
Theses and Dissertations

Fall 2010

Vibration-based damage detection with new operational response and waveform analysis methodology

Kyle D. Hudson
University of Iowa

Follow this and additional works at: <https://ir.uiowa.edu/etd>

 Part of the [Civil and Environmental Engineering Commons](#)


Copyright © 2010 Kyle David Hudson

This thesis is available at Iowa Research Online: <https://ir.uiowa.edu/etd/820>

Recommended Citation

Hudson, Kyle D.. "Vibration-based damage detection with new operational response and waveform analysis methodology." MS (Master of Science) thesis, University of Iowa, 2010.
<https://doi.org/10.17077/etd.fr34svqq>

Follow this and additional works at: <https://ir.uiowa.edu/etd>

 Part of the [Civil and Environmental Engineering Commons](#)

VIBRATION-BASED DAMAGE DETECTION WITH NEW
OPERATIONAL RESPONSE AND WAVEFORM ANALYSIS METHODOLOGY

by

Kyle D. Hudson

A thesis submitted in partial fulfillment
of the requirements for the
Master of Science degree in Civil and Environmental Engineering
in the Graduate College of
The University of Iowa

December 2010

Thesis Supervisor: Assistant Professor Salam Rahmatalla

Copyright by
KYLE D. HUDSON
2010
All Rights Reserved

Graduate College
The University of Iowa
Iowa City, Iowa

CERTIFICATE OF APPROVAL

MASTER'S THESIS

This is to certify that the Master's thesis of

Kyle D. Hudson

has been approved by the Examining Committee for the thesis requirement for the Master of Science degree in Civil and Environmental Engineering at the December 2010 graduation.

Thesis Committee:

Salam Rahmatalla, Thesis Supervisor

M. Asghar Bhatti

Colby Swan

ACKNOWLEDGEMENTS

I would like to acknowledge the efforts of those who worked alongside me to make this work possible. Extensive field and laboratory testing was accomplished with the help of Dr. Hee-Chang Eun, Daniel Ambre, and Ye Liu. All three contributed their time and ideas to make experimental testing a rewarding, valuable part of this work. I would especially like to thank Ye Liu for contributing early on to my development and understanding of the field of damage detection.

I would also like to thank Dr. M. Asghar Bhatti and Dr. Colby Swan for serving on my thesis committee. Both were chosen for this role because I have looked up to them and enjoyed learning from them during my time spent at The University of Iowa.

My advisor, thesis supervisor, and friend, Dr. Salam Rahmatalla deserves significant credit for his commitment to this project. Dr. Rahmatalla has vision beyond the present moment that pushes those around him to think critically and wonder about ideas and paths that at first seem daunting, if not impossible. With his guidance, I was able to expand my horizons and begin to understand the extremely active and progressive field of damage detection at a level I never thought possible. Future students will benefit from his commitment not only to this field but to experimentation, modeling, and practical engineering applications.

Lastly, and most importantly, I owe my deepest gratitude to my family and friends for supporting me during my undergraduate and graduate education. Their encouragement has been unwavering and their dedication to my professional and personal growth has been extremely beneficial during the most rewarding and challenging times of my education.

ABSTRACT

Vibration-based damage identification (VBDI) techniques have been developed in part to address the problems associated with an aging civil infrastructure. To assess the potential of VBDI as it applies to highway bridges in Iowa, three applications of VBDI techniques were considered in this study: numerical simulation, laboratory structures, and field structures. VBDI techniques were found to be highly capable of locating and quantifying damage in numerical simulations. These same techniques were found to be accurate in locating various types of damage in a laboratory setting with actual structures. Although there is the potential for these techniques to quantify damage in a laboratory setting, the ability of the methods to quantify low-level damage in the laboratory is not robust. When applying these techniques to an actual bridge, it was found that some traditional applications of VBDI methods are capable of describing the global behavior of the structure but are most likely not suited for the identification of typical damage scenarios found in civil infrastructure. Measurement noise, boundary conditions, complications due to substructures and multiple material types, and transducer sensitivity make it very difficult for present VBDI techniques to identify, much less quantify, highly localized damage (such as small cracks and minor changes in thickness). However, while investigating VBDI techniques in the field, a novel methodology, operational response and waveform analysis (ORWA), was developed to extend the focus of traditional VBDI techniques by correlating bridge damage to operational structural motion. It was found that if the frequency-domain response of the structure can be generated from operating traffic load, the structural response can be animated and used to develop a holistic view of the bridge's response to various automobile loadings. By animating the response of a field bridge, concrete cracking (in the abutment and deck) was correlated with structural motion and problem frequencies (i.e., those that cause

significant torsion or tension-compression at beam ends) were identified. Furthermore, a frequency-domain study of operational traffic was used to identify both common and extreme frequencies for a given structure and loading. Finally, a finite element analysis of a structure similar to the field bridge was carried out to supplement and partially verify experimental results. Further work should (1) perfect the process of collecting high-quality operational frequency response data; (2) expand and simplify the process of correlating frequency response animations with damage; and (3) develop efficient, economical, pre-emptive solutions to common damage types identified by ORWA.

TABLE OF CONTENTS

LIST OF TABLES	viii
LIST OF FIGURES	ix
CHAPTER	
1. INTRODUCTION	1
1.1 Motivation	1
1.2 Background	2
1.3 Objective	5
2. THEORY	6
2.1 Eigenparameters in VBDI	6
2.2 MS and FRF	7
2.3 MS Curvature Method	8
2.4 FRF Curvature Method	9
2.5 ODSFRF Curvature Method	10
2.6 Curve Fitting Methods	11
2.6.1 Global Curve Fitting	12
2.6.2 Local Curve Fitting	12
2.7 Numerical Simulation with MS Curvature Method	13
2.8 Numerical Simulation with FRF Curvature Method	15
2.9 ORWA	17
3. LABORATORY EXPERIMENTS	20
3.1 Equipment	20
3.2 I-beam	21
3.2.1 Forced Vibration Test with Two Damage Locations	21
3.2.1.1 Identification of two masses	23
3.2.1.2 VBDI with Local Curve Fitting	24
3.2.1.3 VBDI with Local and Global Curve Fitting	27
3.2.1.4 Effect of Nodal Mesh on VBDI with Local Curve Fitting	28
3.2.2 Forced Vibration Test with One Damage Location	31
3.2.2.1 Identification of Clamps on top Flange	31
3.2.2.2 VBDI with Local Curve Fitting	32
3.3 Scale Bridge	34
3.3.1 Forced Vibration Test on Baseline Structure	35
3.3.1.1 Identification of Stiffened Areas	37
3.3.1.2 VBDI with Local Curve Fitting	37
3.3.2 Forced Vibration Test with One Damage Location	38
3.3.2.1 Identification of Mass	39
3.3.2.2 VBDI with Local Curve Fitting	40

3.3.3	Global Operational Vibration Test with One Damage Location	41
3.3.3.1	Analysis of Real Motion of Structure	41
4.	FIELD EXPERIMENTS	44
4.1	Equipment	45
4.2	November 2009 Testing	46
4.2.1	Global Forced Vibration Beam Test	49
4.3	April 2010 Testing	51
4.3.1	Independent Forced Vibration Beam Test	52
4.3.1.1	VBDI with Local Curve Fitting	53
4.3.2	Global Operational Vibration Bridge Test	57
4.3.2.1	Operational VBDI with Global Curve Fitting	60
4.3.2.2	Beams	60
4.3.2.3	Diaphragm Members	62
4.3.3	ORWA	64
4.3.3.1	Frequency-domain analysis of traffic	64
4.3.3.2	Analysis of True Motion of Entire Structure	65
4.3.3.3	Operational Excitation at 13.5 Hz	67
4.3.3.4	Independent Forced Vibration End Beam Test	70
4.3.3.5	Analysis of Relative Motion of Beam End	72
4.3.3.6	Impact Excitation at 13.5 Hz	73
4.3.3.7	Impact Excitation at 16.5 Hz	75
4.3.3.8	Impact Excitation at 35 Hz	75
4.3.3.9	Comparison of Midpoint ODSFRF Magnitudes	76
5.	FINITE ELEMENT MODELING	78
5.1	Model Details	78
5.2	Model Results	80
6.	DISCUSSION AND RECOMMENDATIONS	83
6.1	VBDI	83
6.2	ORWA	87
6.3	Finite Element Modeling	89
7.	CONCLUSION	92
	REFERENCES	93

LIST OF TABLES

Table 4.1: Midpoint ODSFRF Magnitudes at 13.5 Hz

77

LIST OF FIGURES

Figure 2.1:	ANSYS screenshot showing first damage location at element 63 (66.6% cross section reduction)	13
Figure 2.2:	ANSYS screenshots showing second damage location at element 235 (16.6% cross section reduction)	13
Figure 2.3:	ANSYS screenshots showing third damage location at element 315 (50% cross section reduction)	14
Figure 2.4:	First five mode shapes of baseline numerical plate	14
Figure 2.5:	First five mode shapes of damaged numerical plate	14
Figure 2.6:	Summed Damage Index for plate using local curve fitting (66.7% damage at element 63, 16.7% damage at element 235, and 50% damage at element 315)	15
Figure 2.7:	Schematic of the plate used in numerical simulation of FRF Curvature Method	15
Figure 2.8:	Summed Damage Index for plate using local curve fitting (60% damage at element 5 and 5% damage at element 21)	16
Figure 2.9:	Summed Damage Index for plate using global curve fitting (60% damage at element 5 and 5% damage at element 21)	16
Figure 2.10:	Summed Damage Index for plate with 1% noise using local curve fitting (60% damage at element 5 and 5% damage at element 21)	17
Figure 2.11:	Summed Damage Index for plate with 1% noise using global curve fitting (60% damage at element 5 and 5% damage at element 21)	17
Figure 3.1	Typical VBDI forced excitation test setup and hardware including data analyzer, analyst software, impulse hammer, uniaxial accelerometers and structure	20
Figure 3.2:	Cross section of 81” long laboratory I-beam	21
Figure 3.3:	Figure 3.3 Typical laboratory I-beam setup with six fixed accelerometers and two damage zones simulated by fixing masses to the top flange of the structure	22
Figure 3.4:	Roving excitation test setup with two damage zones	22

Figure 3.5:	Overlaid FRFs from a roving excitation test on the undamaged I-beam	23
Figure 3.6:	Overlaid FRFs from a roving excitation test on the I-beam with two masses fixed to the top flange	24
Figure 3.7:	Damage index using difference between FRFs and GSM-fit FRFs	25
Figure 3.8:	Summed damage index using difference between FRFs and GSM fit FRFs for all frequencies	26
Figure 3.9:	Summed damage index using difference between FRF and Global/local-fit FRFs for frequencies from 875-925 Hz	27
Figure 3.10:	Overlaid FRFs from roving excitation test with two masses and 2 inch elements	28
Figure 3.11:	Overlaid FRFs from roving excitation test with two masses and 4 inch elements	29
Figure 3.12:	Overlaid FRFs from roving excitation test with two masses and 6 inch elements	29
Figure 3.13:	Summed damage index for roving excitation test using 2 inch elements	30
Figure 3.14:	Summed damage index for roving excitation test using 4 inch elements	30
Figure 3.15:	Summed damage index for roving excitation test using 6 inch elements	30
Figure 3.16:	Clamps (510 g each) fixed to outer edge of top flange of beam at node 61	31
Figure 3.17:	Overlaid FRFs from roving excitation test on I-beam with two clamps on top flange at node 61	32
Figure 3.18:	Damage index from roving excitation test on I-beam with two clamps at node 61	33
Figure 3.19:	Summed damage index from roving excitation test on I-beam with two clamps at node 61	33
Figure 3.20:	Scale bridge girder and diaphragm member cross sections	34
Figure 3.21:	Scale bridge in the laboratory	35
Figure 3.22:	Rendering of scale bridge with 98 labeled response points	36

Figure 3.23:	Accelerometers fixed with magnets to the first six response points of the scale bridge	36
Figure 3.24:	Overlaid FRFs from forced excitation, roving response test on baseline scale bridge	37
Figure 3.25:	Damage index for right beam of baseline scale bridge	38
Figure 3.26:	Damage index for left beam of baseline scale bridge	38
Figure 3.27:	Mass (1500 g) added to top flange of the right beam, 20 inches from the far end	39
Figure 3.28:	Overlaid FRFs from forced excitation, roving response test on damaged scale bridge	39
Figure 3.29:	Damage index for damaged right beam of scale bridge	40
Figure 3.30:	Damage index for undamaged left beam of baseline scale bridge	41
Figure 3.31:	Overlaid FRFs from operational vibration, roving response test on damaged scale bridge	42
Figure 3.32:	Screenshot of MEscape animation of scale bridge ODSFRFs at 46.9 Hz	43
Figure 3.33:	Screenshot of MEscape animation of scale bridge ODSFRFs at 59.4 Hz	43
Figure 4.1:	Plan view of tested field bridge (FHWA # 31690)	44
Figure 4.2:	Schematic of field bridge girder and diaphragm member cross sections	45
Figure 4.3:	Typical field operational vibration setup	46
Figure 4.4:	Markings at one foot intervals on the web and bottom flange of each beam	47
Figure 4.5:	Single scaffolding tower used to impact beam 1 at node 12	47
Figure 4.6:	Schematic of forced vibration roving accelerometer test setup for bottom flange of beam 1 (one accelerometer per beam and impact point is stationary on beam 1 only)	48
Figure 4.7:	Snooper truck and long poles used to access the bottom flange of each beam	48
Figure 4.8:	Overlaid FRFs from roving response test on all four beams of field bridge	49
Figure 4.9:	Damage Index for beam 1	49

Figure 4.10:	Damage Index for beam 2	50
Figure 4.11:	Damage Index for beam 3	50
Figure 4.12:	Damage Index for beam 4	50
Figure 4.13:	Scaffolding that provided access to the entire superstructure	52
Figure 4.14:	Schematic of forced vibration roving accelerometer test setup for bottom flange of beam 1 (three accelerometers per beam and impact point is on node 16 of each beam)	52
Figure 4.15:	Data acquisition system setup with large impact hammer used to excite each beam	53
Figure 4.16:	Overlaid FRFs for roving response test on beam 1	54
Figure 4.17:	Overlaid FRFs for roving response test on beam 2	54
Figure 4.18:	Overlaid FRFs for roving response test on beam 3	54
Figure 4.19:	Overlaid FRFs for roving response test on beam 4	55
Figure 4.20:	Damage Index for beam 1	56
Figure 4.21:	Damage Index for beam 2	56
Figure 4.22:	Damage Index for beam 3	56
Figure 4.23:	Damage Index for beam 4	57
Figure 4.24:	Rendering of the bridge with the reference response location (A), concentrated beam mesh near boundary conditions (B), normal beam mesh (C), diaphragm member mesh (D), and abutment mesh (E)	58
Figure 4.25:	Operational vibration response measurement of a beam near the boundary condition	58
Figure 4.26:	Operational vibration response measurement of a diaphragm member	59
Figure 4.27:	Operational vibration response measurement of a strip of the vertical face of an abutment	59

Figure 4.28:	Overlaid ODSFRFs from global operational vibration test	60
Figure 4.29:	Summed damage index for beam 1	61
Figure 4.30:	Summed damage index for beam 2	61
Figure 4.31:	Summed damage index for beam 3	61
Figure 4.32:	Summed damage index for beam 4	62
Figure 4.33:	Summed Damage index for diaphragm row 1	63
Figure 4.34:	Summed Damage index for diaphragm row 2	63
Figure 4.35:	Summed Damage index for diaphragm row 3	63
Figure 4.36:	Summed Damage index for diaphragm row 4	63
Figure 4.37:	Overlaid time waveforms from 880 different automobiles	64
Figure 4.38:	Overlaid frequency waveforms from 88 different automobiles	65
Figure 4.39:	Screenshot of MEScope animation of entire bridge ODSFRFs at 13.5 Hz	66
Figure 4.40:	Screenshot of MEScope animation of independent beam FRFs at 13.5 Hz	66
Figure 4.41:	Lateral surface crack in concrete deck near midspan of bridge	67
Figure 4.42:	Screenshot of MEScope NE4 boundary condition animation of ODSFRFs at 13.5 Hz	68
Figure 4.43:	Schematic of torsional and compression-tension action caused by first bending mode of diaphragm members	69
Figure 4.44:	Zoomed-in schematic of torsional and compression-tension action caused by first bending mode of diaphragm members	69
Figure 4.45:	Large diagonal crack in the northeast abutment wall beneath beam 4	70
Figure 4.46:	Rendering of a typical beam end and boundary condition with 42 response points	71
Figure 4.47:	Forced vibration response measurement of northeast end and boundary condition of beam 3	71

Figure 4.48:	Forced vibration response measurement of northeast end and boundary condition of beam 4 with noticeable deterioration of the bottom flange	72
Figure 4.49:	Overlaid FRFs from forced vibration test on northeast boundary condition and end of beam 4	73
Figure 4.50:	Overlaid FRF's from forced vibration test on northeast boundary condition and end of beam 3	73
Figure 4.51:	Screenshot of MEscape NE4 (exterior beam) boundary condition animation of FRF's at 13.5 Hz showing significant torsional motion	74
Figure 4.52:	Screenshot of MEscape NE3 (interior beam) boundary condition animation of FRF's at 13.5 Hz showing very little torsional motion	74
Figure 4.53:	Screenshot of MEscape NE4 (exterior beam) boundary condition animation of ODSFRFs at 16.5 Hz showing the most significant torsional motion of any frequency in the 125 Hz measurement spectrum	75
Figure 4.54:	Screenshot of MEscape NE3 (interior beam) boundary condition animation of ODSFRFs at 35 Hz showing significant compression-tension motion	76
Figure 5.1:	Finite element model mesh of the field bridge	79
Figure 5.2:	First vertical bending mode of the FEM with overlaid contour plot of lateral strain	80
Figure 5.3:	Compressive lateral strain caused by first vertical bending mode of the FEM on the bottom of the concrete deck	81
Figure 5.4:	Compressive horizontal strain caused by first vertical bending mode of the FEM on the corner of an abutment	82
Figure 5.5:	Compressive vertical strain caused by first vertical bending mode of the FEM on the corner of an abutment	82

CHAPTER 1

INTRODUCTION

1.1 Motivation

Maintaining a safe and reliable civil infrastructure is of utmost importance to the national economy and well-being of all citizens. With more than half of the 600,000 bridges in the United States built before 1975, areas of research related to bridge maintenance, inspection, and monitoring have received significant attention in recent years (U.S. Department of Transportation Federal Highway Administration, 2010). In Iowa, especially, where 21% of the almost 25,000 bridges are structurally deficient and over 1,000 bridges are more than 100 years old, the development of technologies related to damage detection and extension of bridge life is crucial to the state's economic growth (U.S. Department of Transportation Federal Highway Administration, 2010). Through the use of health-monitoring systems, a deeper understanding of a given bridge's integrity beyond what visual inspection provides can be achieved. With this knowledge, designers and maintenance professionals can create a relevant and cost-effective strategy for maximizing the life of the bridge. Issues that must be addressed by a health-monitoring system generally fall into two categories: reliability and accuracy of the method and efficiency of the method when applied to an actual structure.

When considering a damage detection tool's reliability and accuracy, four damage issues in bridges have traditionally been considered: (1) detecting damage; (2) locating regions of damage; (3) quantifying the severity of damage; and (4) predicting remaining service life (Rytter, 1993). Unfortunately, due to inevitable noise in field measurements, complicated boundary conditions, difficulty of measuring large structures with multiple materials, and potentially inadequate transducer sensitivity, even the most state-of-the-art damage detection methods

struggle to provide insight into one or more of these issues when applied to civil infrastructure (Adewuyi, Wu, & Serker, 2009; Chang, Flatau, & S.C., 2003). Furthermore, to create a complete engineering solution to damage in aging civil infrastructure, these four issues must be extended to include two more goals: (5) identify the root cause of the damage and (6) provide a solution to the problem.

When considering a health monitoring system's efficiency, ideally it would be low cost, portable, applicable to various bridge sizes and types, and usable at almost any time. Many types of damages in structures, especially at their earlier stages, are highly localized (Guo, Xiaozhai, Dong, & Chang, 2005), and therefore the most accurate and reliable methods for detecting these damages must also be localized, unique, and oftentimes permanent. Localized methods exist but are not feasible for mass deployment on all parts of highway bridges due to high cost and labor intensive installation. Global health monitoring systems are often more portable and less permanent than local methods but sensor placement and spatial resolution is an important factor in their applicability to civil infrastructure (Adewuyi, Wu, & Serker, 2009). Nevertheless, with proper use, global methods such as vibration-based damage identification (VBDDI) have shown promise in their ability to supplement current inspection and design techniques.

1.2 Background

Local damage detection techniques such as acoustic approaches (i.e., ultrasonic, impact-echo, tap test), visual approaches (i.e., X-ray and Gamma ray), and standard strain gauge approaches have been proven to accurately detect damage in the region very close to where the technology is deployed (Guo, Xiaozhai, Dong, & Chang, 2005). However, the logistics and cost associated with using these methods on civil infrastructures can outweigh the benefits even for relatively small structures (Chang, Flatau, & S.C., 2003; Guo, Xiaozhai, Dong, & Chang, 2005).

Global damage detection techniques such as distributed strain measurement, fiber optic measurement and dynamic testing (through VBDI) can deliver a broader view of the structure as a whole (Li & Wu, 2007). Due to the high cost of distributed strain gauges and fiber optics, VBDI has received much attention in recent years. The concept of VBDI methods is that a change in dynamic characteristics (mass, stiffness, or damping) can be detected by observing the associated change in modal parameters such as natural frequency, mode shape (MS), and Frequency Response Function (FRF).

Modal analysis methods have become powerful tools for damage detection in bridges since 1991 when Pandey et al. proposed the idea of using MS curvature as an indicator of the local structural flexibility. In this way, if a crack occurs in a structure, the flexibility of the structure will increase, leading to an increase in the magnitude of the curvature. Most of the methods in this category compare MS curvatures of healthy (undamaged) and damaged structures and therefore require accurate finite element models of the structure. Several researchers (Maia et al., 2003; Farrar & Jauregui, 1994) have based their algorithms on different variations of assessing the curvature of mode shapes. The main disadvantage of this class of approaches is its reliance on highly accurate solving of a modal analysis problem, which is very hard to achieve in practice due to the existence of noise and user interactions.

Alternatively, FRF methods that use only experimental vibration data to detect structural damage have become very popular. These methods can be applied in situations where information on the undamaged structures is available (Ratcliffe, Crane, & Gillespie, 2004; Sampaio & Silva, 1999) or unavailable (Liu, Lieven, & Escamilla-Ambriso, 2009; Maia et al., 2003). The FRF approach does not require the identification of the modal parameters, which is a crucial step, as it is very hard in practice to accurately extract a large number of mode shapes from the measured data;

additionally, the FRF methods can be based on a wide range of frequencies and therefore have a better chance to capture localized damages in real time.

Vibration-based techniques use either controlled vibration or operational vibration to excite the structure. Whereas controlled vibration experiments calculate a MS and FRF from a known excitation (i.e., impact hammer or shaker), operational vibration experiments simply calculate a deflection shape or a response function at a given frequency because excitation magnitudes are unknown (i.e., traffic loading on a bridge). Dynamic testing of field structures has been completed using both forced excitation with an impact hammer (Mertlich et al., 2007; Huber et al., 2000; Miller et al., 1992) and shaker (Kim and Stubbs, 2003; Halling et al., 2001; Farrar and Jauregui, 1994) as well as ambient or operational excitation often using traffic as a source of vibration (Fraser et al., 2010; Whelan et al., 2009). Typically, accelerometers are used to measure the structure's response to a given excitation; however, in recent years more advanced transducers such as Global Positioning Systems (GPS) (Yao et al., 2008) and Micro-electromechanical Systems (MEMS) (Whelan et al., 2009; Uhl et al., 2007) have been applied to field structures independently or integrated with more conventional sensors (Roberts, Meng, & Dodson, 2004). In any case acceleration, velocity, or displacement data in the time domain can be transformed to the frequency domain and used to calculate either a MS, FRF, operating deflection shape (ODS), or operating deflection shape frequency response function (ODSFRF). All four of these parameters can be used to detect damage (by implementing a damage detection code) or to determine the relative motion of one point of the structure to another (McHargue & Richardson, 1993).

Methodologies currently being used in the mechanical systems and machinery field have shown great success in accomplishing all six goals of damage detection and problem solving

discussed earlier. They aim to detect, locate, and quantify damage then correlate that damage with operational loading and provide a solution to the problematic structural motion (Onari and Boyadjis, 2009; Ganeriwala et al., 2008; Bounds and White, 2006; DeMatteo, 2001). However, their potential usage on large civil structures has been given very little attention. This work presents a novel methodology, namely operational response and waveform analysis (ORWA), to extend state-of-the-art operational vibration knowledge from mechanical systems to civil infrastructure, especially bridges nearing the end of their original service life.

1.3 Objective

The objective of this study is to numerically test state-of-the-art damage detection methods, namely VBDI, and apply them to laboratory structures and an Iowa DOT bridge in an attempt to assess the potential of an experimental approach to damage detection methodology as it applies to highway bridges in Iowa. The evaluation uses MS and FRF curvature with various curve fitting models such as the gapped-smooth-method (GSM) to detect damage. The evaluation also considers relative motion due to impact loading and operational loading (in the form of frequency domain animations) to complement and extend damage detection results. This part of the evaluation, combined with a waveform analysis of operational traffic, has been developed into the new operational response and waveform analysis (ORWA) methodology, used to correlate bridge damage with structural motion due to operational vibration. A finite element analysis of the DOT field bridge is completed to supplement and partially verify ORWA findings.

CHAPTER 2

THEORY

2.1 Eigenparameters in VBDI

It is well known that damage in a structure, such as cracking, affects the dynamic characteristics of the structure. More specifically, cracking reduces the stiffness and increases the damping. Therefore, since Adams and Cawley first began measuring changes in natural frequencies due to damage (1979) researchers have been using eigenparameters to detect and locate damage. Two eigenparameters often used in state-of-the-art damage detection algorithms are mode shapes and FRFs. Mode shapes are specific patterns of vibration that a system undergoes in response to specific excitation frequencies. Furthermore, fundamental modes are characterized by the number of half waves in the vibration pattern and correspond to resonant frequencies. Due to the change in stiffness and damping, localized damage causes a localized increase in the magnitude of mode shapes (Pandey et al., 1991). Many researchers first using the change in mode shape to detect damage focused on the first few fundamental modes due to their importance in structural dynamics. Later researchers began looking at higher modes, which allows for a more localized description of the vibration pattern, and recently the FRF has become a popular parameter in VBDI.

The FRF is a complex, frequency domain function that takes the form of a response to forced excitation ratio (or transfer function) at any and all measurement frequencies. The motivation for moving toward the FRF is simple: looking for changes in shapes at modal frequencies is ignoring a significant amount of vibration information present in the structural response (Maia et al., 2003). When experimentally measuring modal parameters, an entire frequency spectrum can be used to detect damage using the FRF as opposed to select

fundamental frequencies with the mode shape. This is crucial for damage located near the node points of a mode shape, which are stationary points in the vibration pattern that will not show any fluctuation in mode shape around that node.

The ODSFRF is a parameter that is used less in damage detection but is equivalent to the FRF in many ways. It is also a complex frequency domain function describing response relative to excitation but the ODSFRF measures input excitation from a fixed response point, as opposed to measuring the excitation directly. It theoretically allows users to achieve the same qualities of the FRF while using ambient vibration as an excitation source.

2.2 MS and FRF

From Newton's second law, the dynamic properties of a multiple-degree-of-freedom system can be derived. As will be shown, the MS and FRF are properties of the structural system only. Although the FRF is dependent on the load amplitude, it is also a ratio, so for a linear system the ratio will remain the same regardless of amplitude (Richardson & Formenti, 1985). The equation of motion for a multiple-degree-of-freedom system is:

$$\mathbf{M}\ddot{\mathbf{x}}(t) + \mathbf{C}\dot{\mathbf{x}}(t) + \mathbf{K}\mathbf{x}(t) = \mathbf{F}(t) \quad (2.1)$$

where \mathbf{M} , \mathbf{C} , and \mathbf{K} are mass, damping, and stiffness matrices, respectively.

$\mathbf{x}(t) = [x_1(t), x_2(t), \dots, x_N(t)]^T$ is the displacement vector with values x_n equal to the displacement at each measured point, and $\mathbf{f}(t) = [f_1(t), f_2(t), \dots, f_N(t)]^T$ is the load or excitation vector with values f_n equal to the excitation at each point. The mode shapes (Φ) for the system can be determined:

$$\Phi = [\Phi_1, \Phi_2, \dots, \Phi_N]^T = \text{Eigenvector}\{\mathbf{K}, \mathbf{M}\} \quad (2.2)$$

Assuming that the forcing function is complex, $\mathbf{f}(t) = \mathbf{f} e^{i\Omega t}$, the solution to Equation 2.1 is

$\mathbf{x}(t) = \mathbf{X} e^{i\Omega t}$. Substituting this solution back into Equation 2.1 gives:

$$-\Omega^2 \mathbf{M} \mathbf{X} e^{i\Omega t} + i\Omega \mathbf{C} \mathbf{X} e^{i\Omega t} + \mathbf{K} \mathbf{X} e^{i\Omega t} = \mathbf{F} e^{i\Omega t} \quad (2.3)$$

Solving for the displacement response and defining a transfer function (\mathbf{H}), Equation 2.3 becomes:

$$\mathbf{X} = \mathbf{X}(\Omega) = [-\Omega^2 \mathbf{M} + i\Omega \mathbf{C} + \mathbf{K}]^{-1} \cdot \mathbf{F} = \mathbf{H} * \mathbf{F} \quad (2.4)$$

For the i^{th} mode coordinate and the p^{th} excitation point, modal superposition can be used to determine a particular modal stiffness, mass, damping, and force:

$$\mathbf{K}_i = \Phi_i^T \mathbf{K} \Phi_i ; \mathbf{M}_i = \Phi_i^T \mathbf{M} \Phi_i ; \mathbf{C}_i = \Phi_i^T \mathbf{C} \Phi_i ; \mathbf{F}_i = \Phi_i^T \mathbf{F}(\Omega) = \Phi_{pr}^T \mathbf{f}_p(\Omega) \quad (2.5)$$

So from Equations 2.4 and 2.5, the modal displacement response for the i^{th} mode coordinate in the r^{th} structural mode shape corresponding to the p^{th} excitation point is:

$$\mathbf{X}_i(\Omega) = \frac{\Phi_{pr} \mathbf{f}_p(\Omega)}{[-\Omega^2 \mathbf{M}_i + i\Omega \mathbf{C}_i + \mathbf{K}_i]} = \mathbf{H}_i * \mathbf{f}_p(\Omega) \quad (2.6)$$

Once again, from modal superposition, the actual displacement response of the measured point l is:

$$x_l(\Omega) = \sum_{i=1}^N \Phi_{lr} \mathbf{X}_i(\Omega) \quad (2.7)$$

So from Equations 2.6 and 2.7, the actual displacement response is:

$$x_l(\Omega) = \sum_{i=1}^N \frac{\Phi_{lr} \Phi_{pr} \mathbf{f}_p(\Omega)}{[-\Omega^2 \mathbf{M}_i + i\Omega \mathbf{C}_i + \mathbf{K}_i]} \quad (2.8)$$

From Equations 2.6 and 2.8, the FRF with respect to displacement between the measured point l and the excitation point p (\mathbf{H}_{lp}) is:

$$\mathbf{H}_{lp} = \frac{x_l(\Omega)}{\mathbf{f}_p(\Omega)} = \sum_{i=1}^N \frac{\Phi_{lr} \Phi_{pr}}{[-\Omega^2 \mathbf{M}_i + i\Omega \mathbf{C}_i + \mathbf{K}_i]} \quad (2.9)$$

Factoring and letting $\frac{\mathbf{M}_i}{\mathbf{K}_i} = \frac{1}{\omega^2}$, and from $\frac{c}{2m\omega} \Rightarrow \frac{\mathbf{C}_i}{\mathbf{K}_i} = \frac{2\zeta}{\omega}$, Equation 2.9 becomes:

$$H_{lp} = \sum_{i=1}^N \frac{\Phi_{lr} \Phi_{pr}}{K_i \left[-\left(\frac{\Omega}{\omega}\right)^2 2i\omega\zeta\left(\frac{\Omega}{\omega}\right) + 1 \right]} \quad (2.10)$$

Finally, the FRF with respect to acceleration is $H_{lp,acc} = -\omega^2 H_{lp,displ}$ so:

$$H_{lp,acc} = \sum_{i=1}^N \frac{-\omega^2 \Phi_{lr} \Phi_{pr}}{K_i \left[-\left(\frac{\Omega}{\omega}\right)^2 2i\omega\zeta\left(\frac{\Omega}{\omega}\right) + 1 \right]} \quad (2.11)$$

Because Equation 2.11 is complex, it can be split into real and imaginary components as follows:

$$H_{lp,acc} = \sum_{i=1}^N \frac{-\omega^2 \Phi_{lr} \Phi_{pr} K_i}{K_i^2 \left\{ \left[\left(\frac{\Omega}{\omega}\right)^2 2\omega\zeta\left(\frac{\Omega}{\omega}\right) \right]^2 + 1 \right\}} + i \sum_{i=1}^N \frac{\omega^2 \Phi_{lr} \Phi_{pr} K_i \left[-\left(\frac{\Omega}{\omega}\right)^2 2\omega\zeta\left(\frac{\Omega}{\omega}\right) \right]}{K_i^2 \left\{ \left[\left(\frac{\Omega}{\omega}\right)^2 2\omega\zeta\left(\frac{\Omega}{\omega}\right) \right]^2 + 1 \right\}} \quad (2.12)$$

Equation 2.12 is the analytical definition of FRF, but for experimental purposes it is easier to view the FRF as a function of the Fourier spectrum of the excitation and response: The FRF is defined as the ratio of the Fourier spectrum of the response to the Fourier spectrum of the force:

$$FRF(\omega) \equiv \alpha = \frac{F_x(\omega)}{F_y(\omega)} \quad (2.13)$$

2.3 MS Curvature Method

The MS curvature method was proposed based on the premise that for a given moment applied to a structure, a reduction in stiffness associated with damage will cause an increase in the curvature of the mode shape (Pandey, Biswas, & Samman, 1991). The MS curvature of the structure is typically computed using numerical differentiation of shapes at evenly spaced intervals:

$$\Phi_i'' = \frac{\Phi_{i+1} - 2\Phi_i + \Phi_{i-1}}{h^2} \quad (2.14)$$

A damage index can be computed by summing the absolute difference or absolute squared difference of the damaged and baseline mode shapes for all impact points:

$$\Delta \Phi_i'' = \sum_j |\Phi_{ij}''^2 - \Phi_{ij}''^{*2}| \quad (2.15)$$

The disadvantage of the MS curvature method is that the mode shapes have to be accurately solved to produce accurate results. For large systems, this task is difficult and can be expensive to implement. Also, relatively small noise levels can significantly distort the modal solution and are only magnified by numerical differentiation (Adewuyi, Wu, & Serker, 2009).

2.4 FRF Curvature Method

This method simply extends the MS curvature method proposed by Pandey et al. to all frequencies in the measurement range:

$$\alpha_{i,j,\omega} = \frac{\alpha_{i+1,j} - 2\alpha_{i,j} + \alpha_{i-1,j}}{h^2} \quad (2.16)$$

Similarly, a damage index can be computed by summing the absolute difference or absolute squared difference of the damaged and baseline FRFs for all impact points:

$$\Delta \alpha_{i,\omega}'' = \sum_j |\alpha_{ij}''^2 - \alpha_{ij}''^{*2}| \quad (2.17)$$

A second damage index can be computed by summing Equation 2.17 for all frequencies in the measurement range:

$$S_i = \sum_{\omega} \Delta \alpha_{ij}''^2 \quad (2.18)$$

Since damage can be detected in mode shapes as an abnormality in the curvature of a given shape (Pandey, Biswas, & Samman, 1991), the damage indices in Equations 2.17 and 2.18 can be calculated using either the real or imaginary part of the FRF because both parts are a function of the frequency dependent r^{th} structural mode shape, as shown in Equation 2.12.

Furthermore, if damage information from both parts is desired, a real damage index can be added to an imaginary damage index if proper normalization is used. Although all three techniques tend to show similar results, it should be noted that all damage index plots to follow are a summation of real and imaginary damage indices.

An advantage of the FRF curvature method over the mode shape curvature method is that it contains an entire spectrum of frequency information as opposed to information at select (natural) frequencies. Also, because the FRF can be readily obtained from most data acquisition systems in the form of Equation 2.13, there is no need to experimentally determine the modal parameters as in MS curvature method. Therefore, significant computational time and effort is avoided with the FRF curvature method.

2.5 ODSFRF Curvature Method

Although the ODSFRF is calculated from data that is dependent only on response, the damage detection algorithm is the exact same as the FRF (Equations 2.16-2.18 apply to the ODSFRF as well). Theoretically, there is no advantage to collecting data via the ODSFRF versus the FRF because it is assumed that there will be less noise introduced in a known excitation than an operating excitation (Schwarz & Richardson, 2004). The advantage of the method is the practicality and relative ease of collecting data on civil infrastructures when no impact hammer or shaker is required.

2.6 Curve Fitting Methods

As shown in Equations 2.15 and 2.17, the MS curvature, FRF, and ODSFRF methods all rely on a baseline modal parameter. Unfortunately, in many circumstances, it is not possible to acquire data for an undamaged structure. Various researchers have shown that when the structure is relatively simple, it may be feasible to create a finite element model to determine the

baseline MS or FRF (Adewuyi, Wu, & Serker, 2009; Sampaio & Silva, 1999; Ratcliffe, 2009; Maia et al., 2003). However, for larger structures such as bridges, it is very difficult to capture all the details that affect dynamic properties in a finite element model. In addition to time-dependent variables such as testing temperature and noise level, boundary conditions in bridges are often in between the theoretical pin, roller, and free conditions commonly used in finite element models (Ratcliffe, 2009). One alternative to FEA and physically testing a baseline structure is curve fitting experimental data from a damaged structure, assuming that the baseline structure would yield smooth experimental data.

2.6.1 Global Curve Fitting

Global curve fitting processes all measurements together to determine the frequency and damping parameters and then uses those known values to calculate complex residues for each measurement (Richardson & Formenti, 1985). Examples of global curve fitting methods include polynomials, exponential functions, the peak (Gaussian) model, and the Fourier/power series, all of which are available in the MATLAB Curve Fitting Toolbox. MEscape software is also capable of globally smoothing FRF data, based on various fitting parameters.

2.6.2 Local Curve Fitting

In local curve fitting, each measurement is individually fit so any given curve's parameters (i.e., frequency, damping, and complex residue) are independent of another. An example of a local curve fitting method is the gapped-smoothing method (GSM), created by Ratcliffe et al. This method fits a gapped cubic polynomial to each measurement when calculating curvature, meaning that for the position x_i along the structure, the corresponding curvature is:

$$p_0 + p_1 x_i + p_2 x_i^2 + p_3 x_i^3 \quad (2.19)$$

The coefficients p_0 , p_1 , p_2 and p_3 are determined using C_{i-2} , C_{i-1} , C_{i+1} and C_{i+2} (curvature element C_i is gapped or left out of the calculation).

2.7 Numerical Simulation with MS Curvature Method

To show the MS curvature method's ability to detect damage, a numerical simulation was completed in ANSYS with a 470 element long plate. The plate was assumed to have free-free boundary conditions at its ends. Three damage locations were simulated at elements 63, 235, and 315 by decreasing the plate's thickness by 66.6%, 16.6%, and 50%, respectively. The ANSYS screenshots in Figures 2.1, 2.2 and 2.3 show the three damage locations.

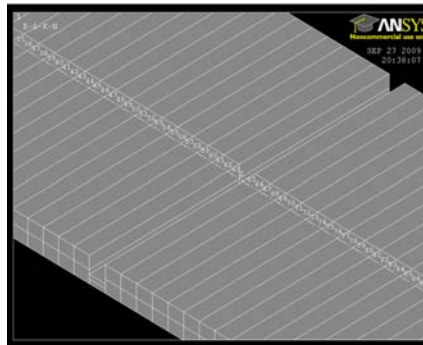


Figure 2.1 ANSYS screenshot showing first damage location at element 63 (66.6% cross section reduction)

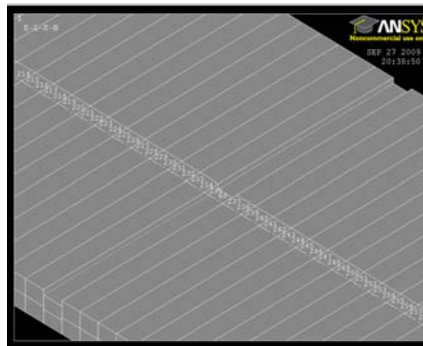


Figure 2.2 ANSYS screenshot showing second damage location at element 235 (16.6% cross section reduction)

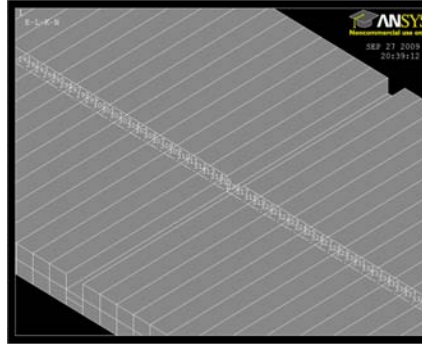


Figure 2.3 ANSYS screenshot showing second damage location at element 315 (50% cross section reduction)

Figures 2.4 and 2.5 show the first five mode shapes of the baseline and damaged plate, respectively. As shown, there is very little difference between the mode shapes of the two plates. However, when using the MS Curvature method with local curve fitting (GSM), each damage location is detected (although the change in curvature at the element with 16.6% reduction in thickness is very small) as shown in Figure 2.6.

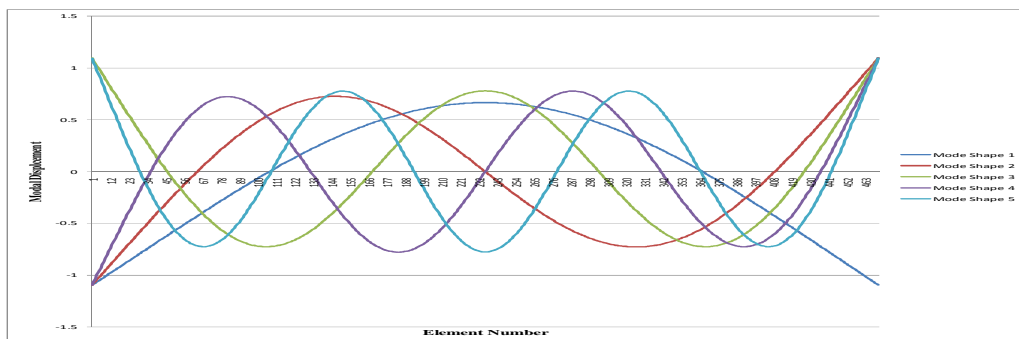


Figure 2.4 First five mode shapes of baseline numerical plate

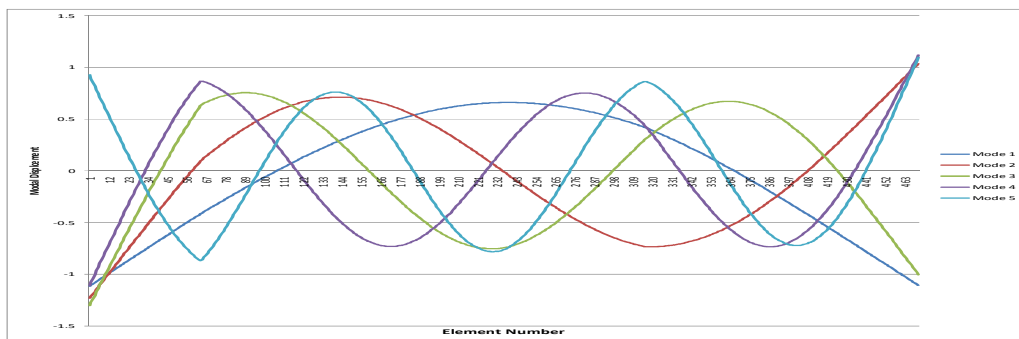


Figure 2.5 First five mode shapes of damaged numerical plate

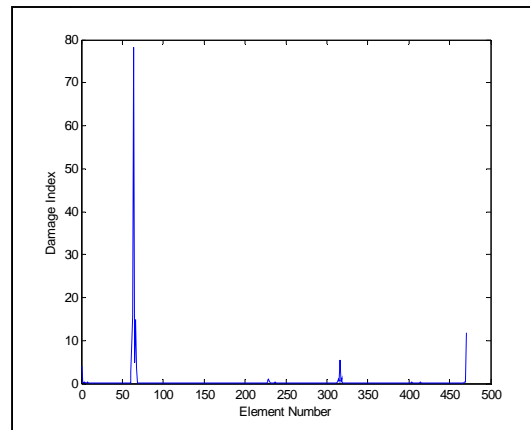


Figure 2.6 Summed Damage Index for plate using local curve fitting (66.7% damage at element 63, 16.7% damage at element 235, and 50% damage at element 315)

2.8 Numerical Simulation with FRF Curvature Method

To show the FRF curvature method's ability to detect damage, a numerical simulation was completed in MATLAB with a 30 element long plate. The plate was assumed to have free-free boundary conditions at its ends. Two damage locations were simulated at elements 5 and 21 by decreasing the plate's thickness by 60% and 5%, respectively. Figure 2.7 shows a schematic of the plate.

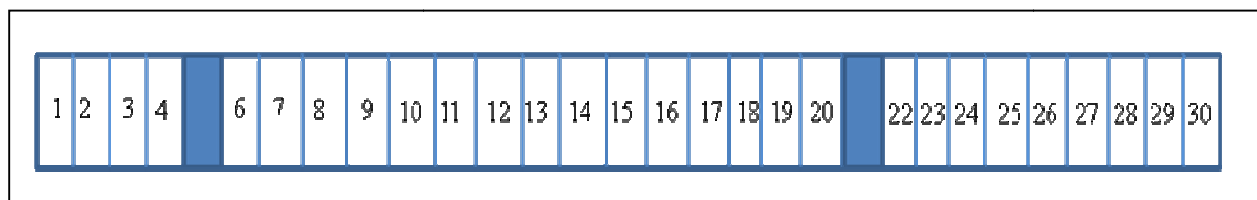


Figure 2.7 Schematic of plate used in numerical simulation of FRF Curvature Method

Figures 2.8 and 2.9 show the summed damage indices for the plate using local and global curve fitting, respectively. Local curve fitting accurately locates the damage and seems to quantify the magnitudes of the damage as well. Global curve fitting also locates the damage, but fails to show a significant difference in the thickness between elements 5 and 21.

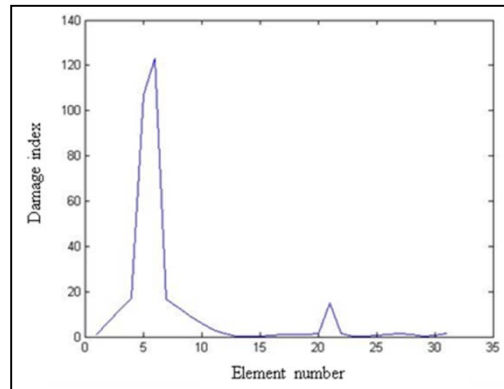


Figure 2.8 Summed Damage Index for plate using local curve fitting (60% damage at element 5 and 5% damage at element 21)

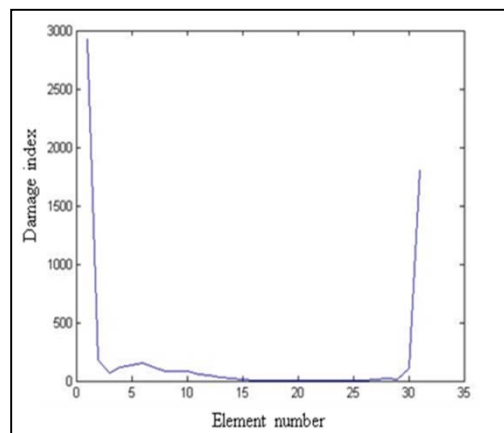


Figure 2.9 Summed Damage Index for plate using global curve fitting (60% damage at element 5 and 5% damage at element 21)

Because there is significant and inevitable noise in experimental measurements, the same numerical simulation was run with the addition of 1% random noise. Figures 2.10 and 2.11 show the summed damage indices for the plate with 1% noise using local and global curve fitting, respectively. Both fitting methods identify a broad damage location between elements 3 and 15 and are unable to identify any curvature change around element 21. Therefore, the addition of noise has significantly impacted the quality of the damage detection results.

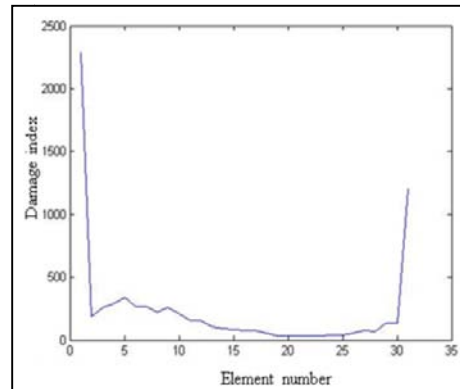


Figure 2.10 Summed Damage Index for plate with 1% noise using local curve fitting (60% damage at element 5 and 5% damage at element 21)

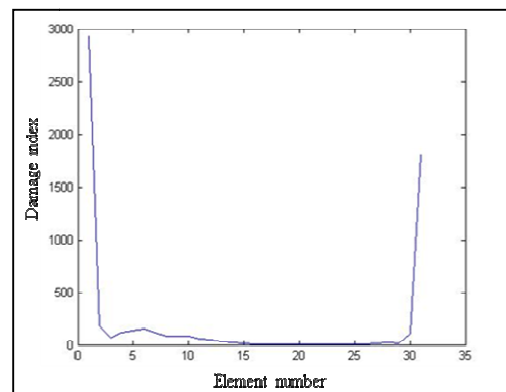


Figure 2.11 Summed Damage Index for plate with 1% noise using global curve fitting (60% damage at element 5 and 5% damage at element 21)

2.9 ORWA

ORWA is a methodology used to extend state-of-the-art vibration-based damage detection algorithms currently being developed to identifying the cause of damage and proving a solution to the problem. The method can be summed up in four steps: (1) experimentally gather operational response data, (2) determine the most significant excitation/response frequencies (3) visualize structural motion at significant frequencies and look for problematic motion, and (4) correlate any structural damage to problematic motion and its corresponding frequency.

In this work, operational response was visualized using acceleration data that was manipulated to give ODSFRF's, which are similar to operating deflection shapes (ODS). ODS are a technique used for visualization of the vibration pattern of a structure under real life operating conditions. Unlike modal analysis, ODS can analyze the response of a structure under forces and complicated boundary conditions. Therefore, ODS contains both forced and resonant vibration components. ODS is one way to obtain correlation between different points on the structure. It can indicate points with the largest motion and specify their directions. ODS also provide very useful information regarding the dynamic characteristics of a structure and its components.

Operating deflection shapes are essentially column vectors of transmissibilities. For experimental purposes it is convenient to view transmissibility as a function of the cross and auto spectra, which can readily be obtained from most multi-channel data acquisition systems. The cross spectrum (G_{xy}) is computed by multiplying the Fourier spectrum of a measured response by the complex conjugate of the Fourier spectrum of a fixed reference response as follows:

$$G_{xy}(\omega) = F_x(\omega) F_y^*(\omega) \quad (2.20)$$

The auto spectrum (G_{yy}) is computed by multiplying the Fourier spectrum of the fixed reference response by the complex conjugate of itself as follows:

$$G_{yy}(\omega) = F_y(\omega) F_y^*(\omega) \quad (2.21)$$

Transmissibility (T_{xy}) is simply the ratio of the cross spectrum to the auto spectrum, which gives the motion of each roving response point normalized by the motion of the reference response point as follows:

$$T_{xy}(\omega) = \frac{G_{xy}(\omega)}{G_{yy}(\omega)} \quad (2.22)$$

An alternative parameter to transmissibility (and ODS) is the ODSFRF which is calculated by replacing the magnitude of the cross spectrum with the square root of the magnitude of the response auto spectrum (Vold, Schwarz and Richardson, 2000) as follows:

$$\text{ODSFRF}(\omega) = \sqrt{G_{xx}} \frac{G_{xy}(\omega)}{|G_{xy}(\omega)|} = \overline{F_x(\omega)} \quad (2.23)$$

One advantage of the ODSFRF is that it measures the true amount of motion at each measured point directly whereas transmissibility must be multiplied by the reference auto spectrum to attain the true motion, which can introduce noise. Also, for viewing purposes the ODSFRF is more convenient because it shows peaks at resonance frequencies, whereas transmissibilities show flat spots (Vold, Schwarz and Richardson, 2000).

CHAPTER 3

LABORATORY EXPERIMENTS

3.1 Equipment

Because VBDI techniques require that the dynamic characteristics of the structure be determined and analyzed, certain equipment is needed to utilize these methods. In the laboratory, a 500 lbF range Dytran impulse hammer was used to excite various structures. Six 100 g range Dytran uniaxial accelerometers were used both in the field and in the laboratory. Typically, accelerometers were fixed to structures with a magnet, but in some cases glue and wax were used. An IOtech ZonicBook/618E Data Analyzer was used to acquire data and construct FRFs. MEscape software was used to calculate mode shapes and ODSFRFs, as well as to animate data. MATLAB was used to implement VBDI algorithms. Figure 3.1 shows a typical laboratory forced vibration test setup.

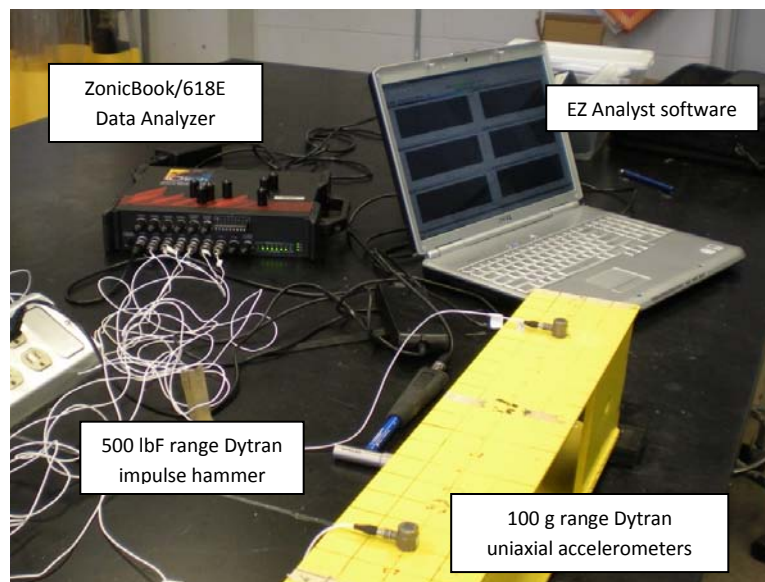


Figure 3.1 Typical VBDI forced excitation test setup and hardware including data analyzer, analyst software, impulse hammer, uniaxial accelerometers and structure

3.2 I-beam

Laboratory testing was completed on a W6x9 beam 81 inches in length and simply supported by hard rubber pads at its ends. Figure 3.2 shows a cross section of the I-beam. Two different methods were used to determine the dynamic response of the I-beam due to forced excitation: roving response and roving excitation. For both methods, frequencies from 0-10000 Hz were analyzed with a spectral density of 1 line/6.25 Hz.

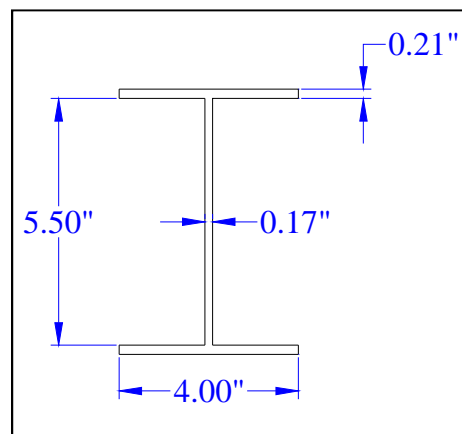


Figure 3.2 Cross section of 81" long laboratory I-beam

3.2.1 Forced Vibration Test with Two Damage Locations

During a roving excitation test, the I-beam was impacted at each node and six accelerometers were fixed to various nodes on the structure. Both baseline and damaged forced excitation tests were run on the I-beam. Damage was simulated by fixing masses of different sizes to the centerline of the top flange of the beam, thereby creating a local change in mass and stiffness in the region surrounding each mass. Figure 3.3 shows a picture of a typical roving excitation setup with two damage locations. As shown in Figure 3.4, accelerometers were fixed on nodes 4, 16, 26, 43, 55, and 74 and masses of 1.7 kg and 0.5 kg were fixed to the top flange between nodes 60 and 62 and nodes 33 and 36, respectively.



Figure 3.3 Typical laboratory I-beam setup with six fixed accelerometers and two damage zones simulated by fixing masses to the top flange of the structure

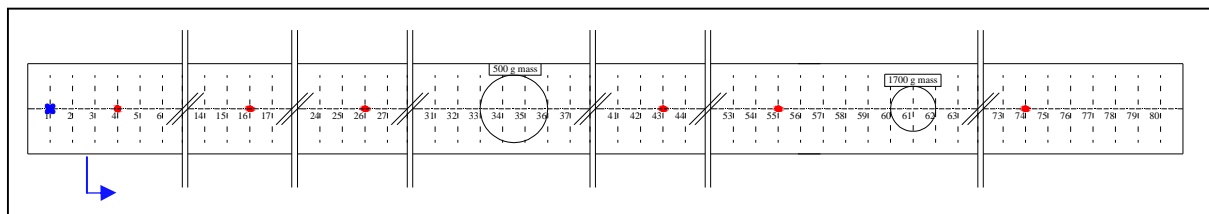


Figure 3.4 Roving excitation test setup with two damage zones

Various excitation meshes were considered during testing to determine the sensitivity of the damage detection algorithms to mesh size. The most common mesh size used was one impact per inch, but one impact per 2 inches, 4 inches, and 6 inches tests were also run. For each excitation point, the beam was impacted five times, creating 30 FRFs (one FRF for each fixed response per excitation). These FRFs were then averaged for each impact point. Therefore, with 80 excitation points and six fixed responses, 480 FRFs were created. Assuming that each

accelerometer is able to capture the dynamic characteristics of the entire structure (i.e., the accelerometer is not located on a stationary modal coordinate and sensitivity is not an issue), these 480 FRFs can be averaged for each accelerometer, creating 80 usable FRFs.

3.2.1.1 Identification of two masses

Figure 3.5 shows all 480 overlaid FRFs from 0-2000 Hz collected from a roving excitation test (see Section 3.2.2) on the undamaged I-beam. Although these undamaged FRFs are not needed in the damage detection algorithms, they can be compared to the FRFs from the same structure with added damage. Figure 3.6 shows the overlaid FRFs from 0-2000 Hz collected from a roving excitation test on the I-beam with two masses fixed to the top flange. The small mass between nodes 33 and 36 and the large mass between nodes 60 and 62 represent 1.8% and 6% of the beam's total mass, respectively. In comparing Figures 3.5 and 3.6, one can notice both a change in shape of the FRFs and a shift in natural frequencies. Although observation of a shift in natural frequencies identifies the presence of damage, other methods must be used to locate and quantify the damage (i.e., VBDI algorithms).

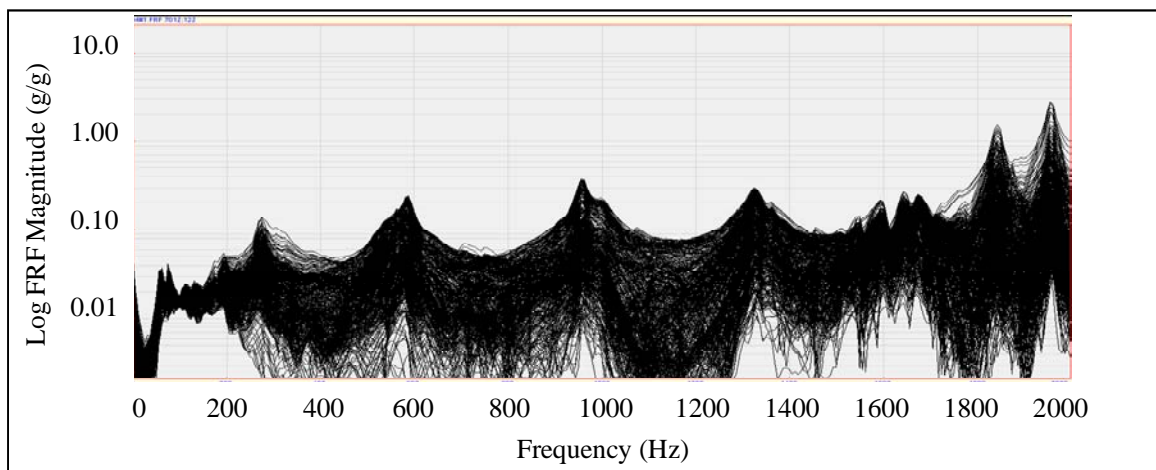


Figure 3.5 Overlaid FRFs from a roving excitation test on the undamaged I-beam

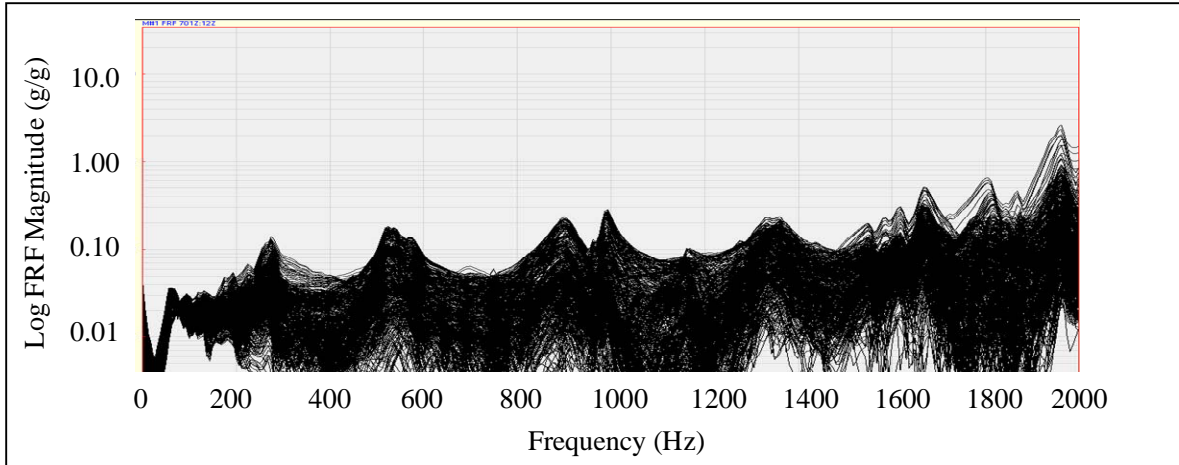


Figure 3.6 Overlaid FRFs from a roving excitation test on the I-beam with two masses fixed to the top flange

3.2.1.2 VBDI with Local Curve Fitting

As stated in Chapter 2, damage can be simulated by the addition of mass to a structure because mass is a dynamic property. Figure 3.7 shows the damage index (calculated using Eq 2.18) from a roving excitation test. The y-axis is position along the beam from 0 to 81 inches, and the x-axis is frequency shown in spectral lines. Warm colors represent the largest change in curvature between actual FRF test results and the curve fit FRF test results (using GSM), and white indicates virtually no change. The frequency range for this particular test was 10000 Hz at 1 line/6.25 Hz. The solid red lines indicate the boundaries of the large mass. Likewise, the dashed red lines indicate the boundaries of the small mass.

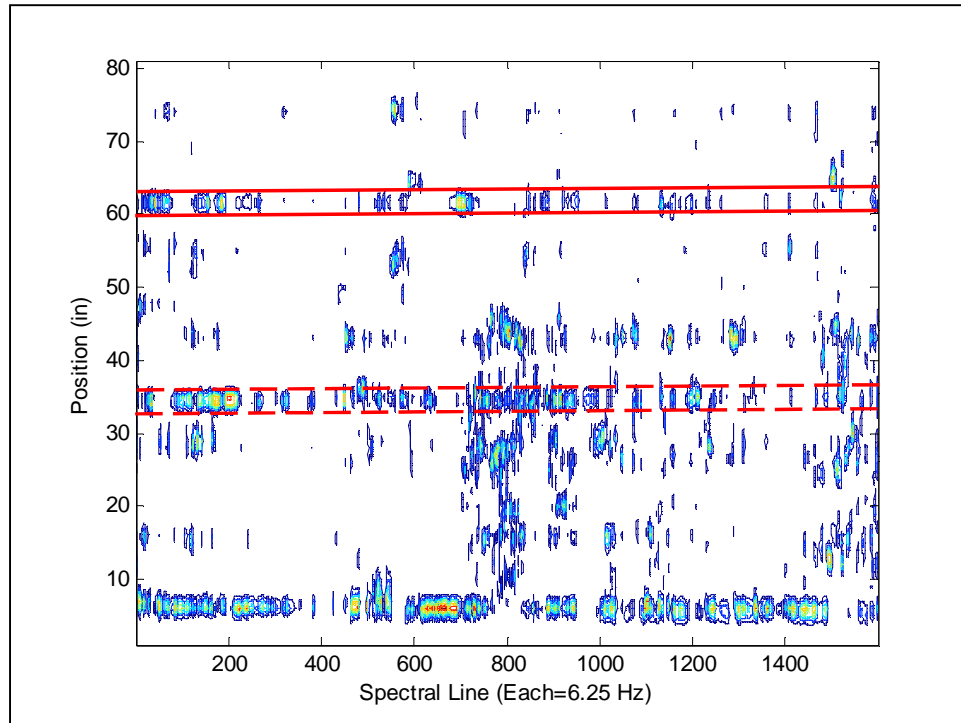


Figure 3.7 Damage index using difference between FRFs and GSM-fit FRFs

Figure 3.7 clearly indicates a large change in FRF curvature within both damage regions but also shows a thick band of color around 5-8 inches. Also present are thinner bands of color at various points along the structure. Figure 3.8 is the summed damage index (calculated using Equation 2.19), which sums the change in curvature along the entire frequency spectrum. Therefore, the x-axis is positioned along the beam and the y-axis is the magnitude of the summed damage index. Once again, the red lines indicate the damage boundaries, and black lines were added to show the location of each accelerometer. Figure 3.8 not only locates the damage properly, but also shows a relationship between small intermediate peaks in summed damage index and accelerometer location: accelerometers at nodes 16, 43, 55, and 74 were located perfectly.

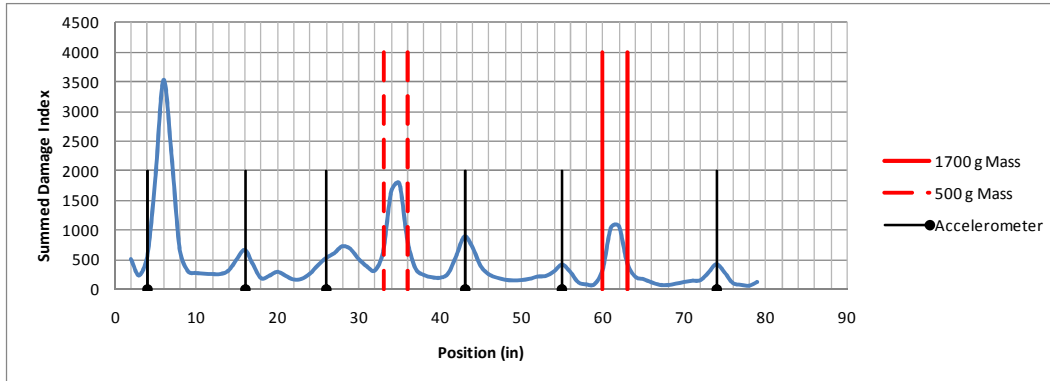


Figure 3.8 Summed damage index using difference between FRFs and GSM fit FRFs for all frequencies

The reason for the difference in FRF curvature at fixed accelerometer locations is not fully understood. The accelerometers have negligible mass compared to the cylinders fixed to the top flange of the beam and have no effect on the beam's damping or stiffness. Because the beam was impacted every inch, the impacts on nodes very close to a given accelerometer could be causing the change in curvature. For this particular structure, the false positive damage indication at each accelerometer can easily be suppressed with numerical techniques because their magnitude is less than that of the actual damage. For other structures, this could hold true, or the accelerometer locations could be subtracted from subsequent tests (i.e., accelerometers are placed in the same reference locations for various tests during a structure's life cycle, and results are subtracted so that accelerometer false positives disappear).

The large change in curvature between 5-8 inches indicated in both Figures 3.7 and 3.8 could be due to the fact that the accelerometer at node 4 is on a highly stiffened portion of the beam. As shown in Figure 3.5, the laboratory I-beam has stiffeners at both ends. The stiffener at the other end of the beam may not have been identified because the closest accelerometer was a few inches away, not directly on the stiffened part of the flange.

Unfortunately, both Figures 3.7 and 3.8 fail to properly quantify the severity of the damage relative to each other. The band of color in the damage index is thicker and darker in the region of the smaller mass, and the peak in the summed damage index is higher for the smaller mass. This is most likely due to the fact that the smaller mass was placed more toward the middle of the beam, where there is maximum deflection.

3.2.1.3 VBDI with Local and Global Curve Fitting

As stated in Chapter 2, GSM is a local curve fitting method, whereas MEscape software is capable of globally smoothing FRF test results. The results presented in this section represent a novel approach to smoothing data in damage detection. First the FRF data is globally smoothed in MEscape only within a region where a mode is well-defined (because global smoothing of the entire frequency spectrum fails to accurately curve fit the data). For this test, the third mode from 875-925 Hz was chosen (see Figure 3.6). Next, the curve fit data and actual data within this 50 Hz region are exported from MEscape and run through the normal FRF Curvature with GSM damage detection algorithm independently of each other. The squared difference of the summed damage index from the curve fit data and actual data is then calculated, as shown in Figure 3.9.

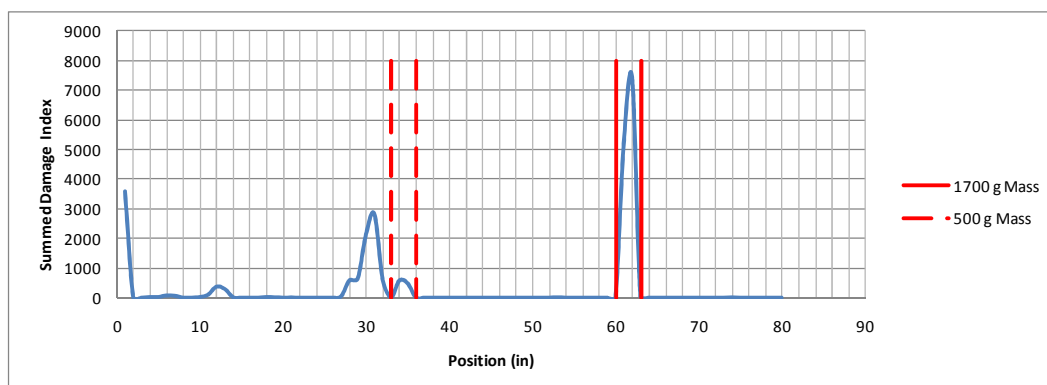


Figure 3.9 Summed damage index using difference between FRF and Global/local-fit FRFs for frequencies from 875-925 Hz

As Figure 3.9 shows, both areas of damage are accurately located, and the large mass between nodes 60-62 shows up with a magnitude significantly higher than that of the smaller mass. Also, the accelerometer locations no longer show up as damage because they have effectively been subtracted out. The small peak around node 12 and the large peak around node 31 are false positives. They exist because in these locations the MEscape global curve fit did not accurately represent the actual data, either because better software parameters could be set or because the frequency range was too limited or extensive.

3.2.1.4 Effect of Nodal Mesh on VBDI with Local Curve Fitting

Three roving excitation tests with varying nodal meshes were completed on the I-beam with the same damage configuration as described in the previous two sections. Figures 3.10-3.12 show the 240, 120, and 84 overlaid FRFs from tests with 2 inch, 4 inch and 6 inch roving excitation point measurements. All three figures have approximately the same shape and natural frequencies, which is to be expected.

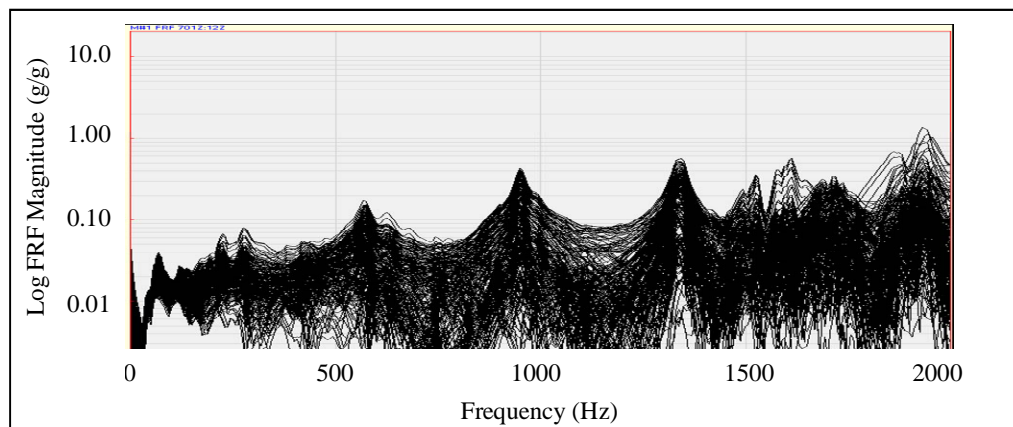


Figure 3.10 Overlaid FRFs from roving excitation test with two masses and 2 inch elements

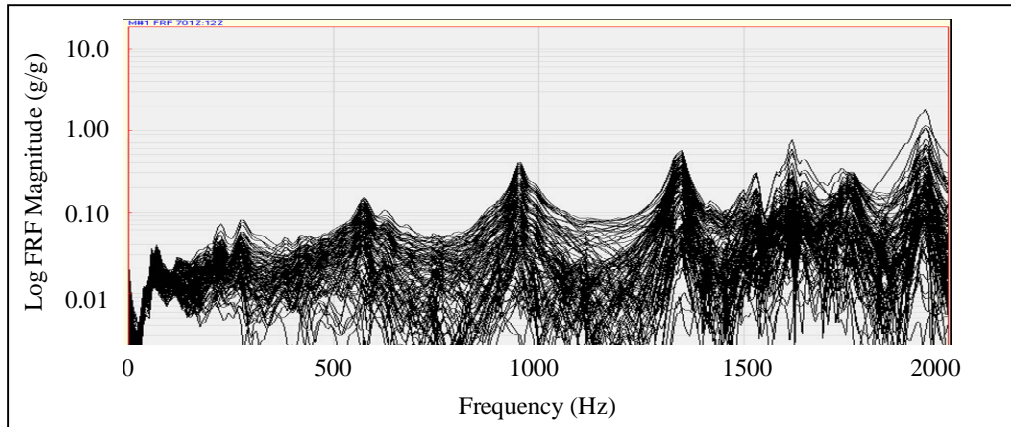


Figure 3.11 Overlaid FRFs from roving excitation test with two masses and 4 inch elements

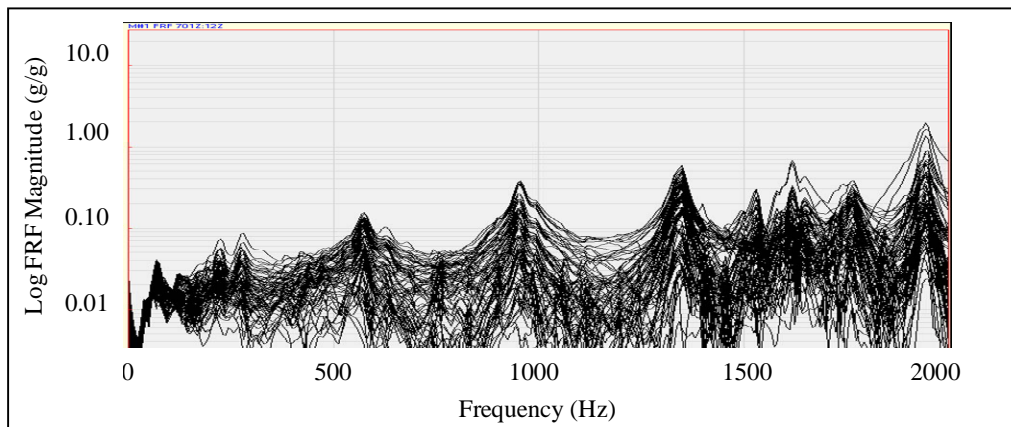


Figure 3.12 Overlaid FRFs from roving excitation test with two masses and 6 inch elements

Figures 3.13-3.15 show the summed damage indices for roving excitation tests with 2 inch, 4 inch, and 6 inch nodal meshes, respectively. Although not as smooth as the summed damage index from a nodal mesh of 1 inch, Figure 3.14 shows that the damage is still noticeable when exciting the beam every 2 inches. However, with this setup, the accelerometer locations are not identified as clearly as the fine mesh, which means it will be harder to account for their presence with numerical techniques. Also, the magnitude of the fourth accelerometer peak is actually greater than both damage locations. Both Figures 3.14 and 3.15 show that nodal meshes of one excitation point per 4 inches and 6 inches is not adequate to detect damage.

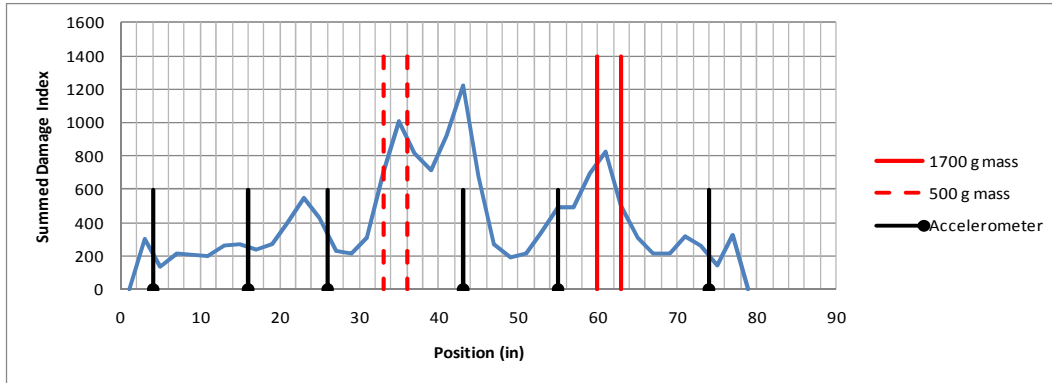


Figure 3.13 Summed damage index for roving excitation test using 2 inch elements

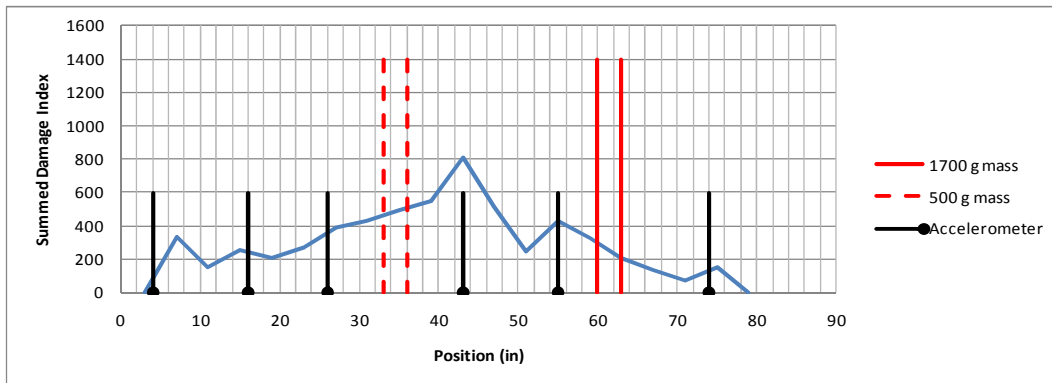


Figure 3.14 Summed damage index for roving excitation test using 4 inch elements

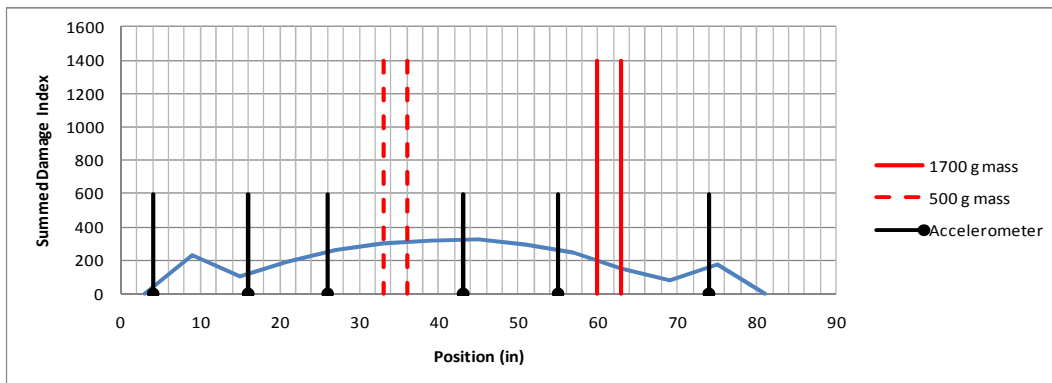


Figure 3.15 Summed damage index for roving excitation test using 6 inch elements

3.2.2 Forced Vibration Test with One Damage Location

Other damage locations and types were considered while testing the I-beam. In order to test the ability of the method to detect damage away from the centerline, 510 g clamps were fixed to the outer edge of the top flange at node 61 as shown in Figure 3.16. A roving excitation test similar to that shown in Figure 3.6 was run with this setup.

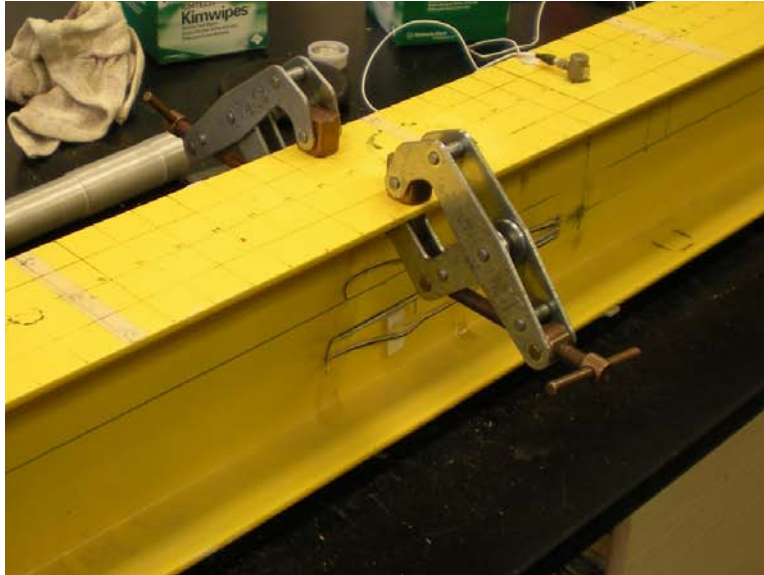


Figure 3.16 Clamps (510 g each) fixed to outer edge of top flange of beam at node 61

3.2.2.1 Identification of Clamps on Top Flange

Figure 3.17 shows the overlaid FRFs from 0-2000 Hz collected from a roving excitation test on the I-beam with clamps fixed to the top flange at node 61. Together, the 510 g clamps represent 3.7% of the beam's total mass.

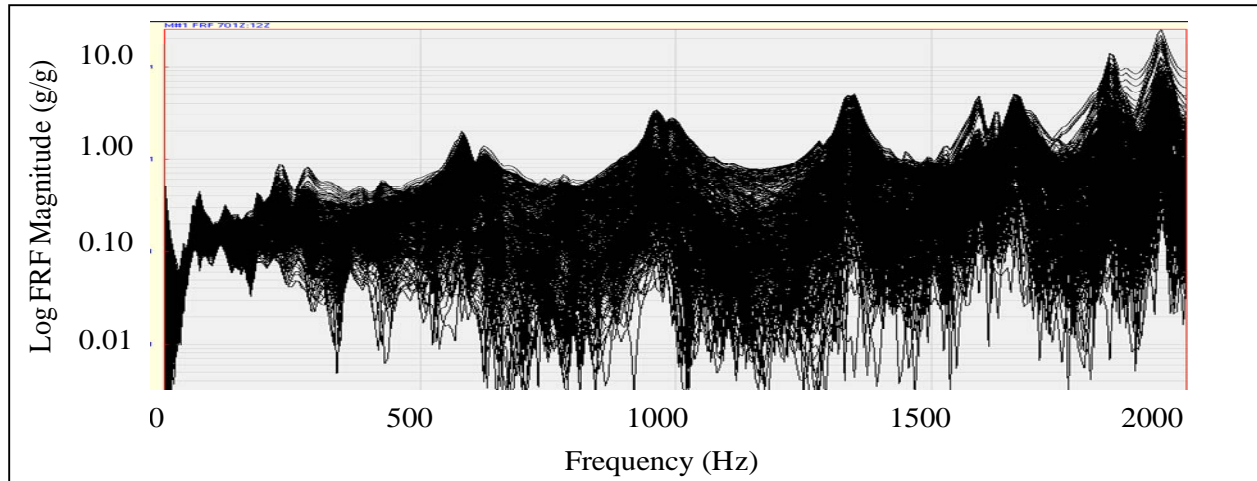


Figure 3.17 Overlaid FRFs from roving excitation test on I-beam with two clamps on top flange at node 61

3.2.2.2 VBDI with Local Curve Fitting

Figure 3.18 shows the damage index of a roving excitation test on the I-beam with two 510 g clamps fixed to the edges of the top flange at node 61. As shown, a thick band of color exists between nodes 60 and 62, indicating large changes in curvature between the experimental FRF and the smoothed FRF. Figure 3.19 shows the summed damage index with red lines for the region where the clamps were fixed and black lines indicating the locations of accelerometers. Once again, the accelerometer locations are clearly located with the roving excitation test method; however, the damage magnitude is 50% greater than the largest accelerometer peak.

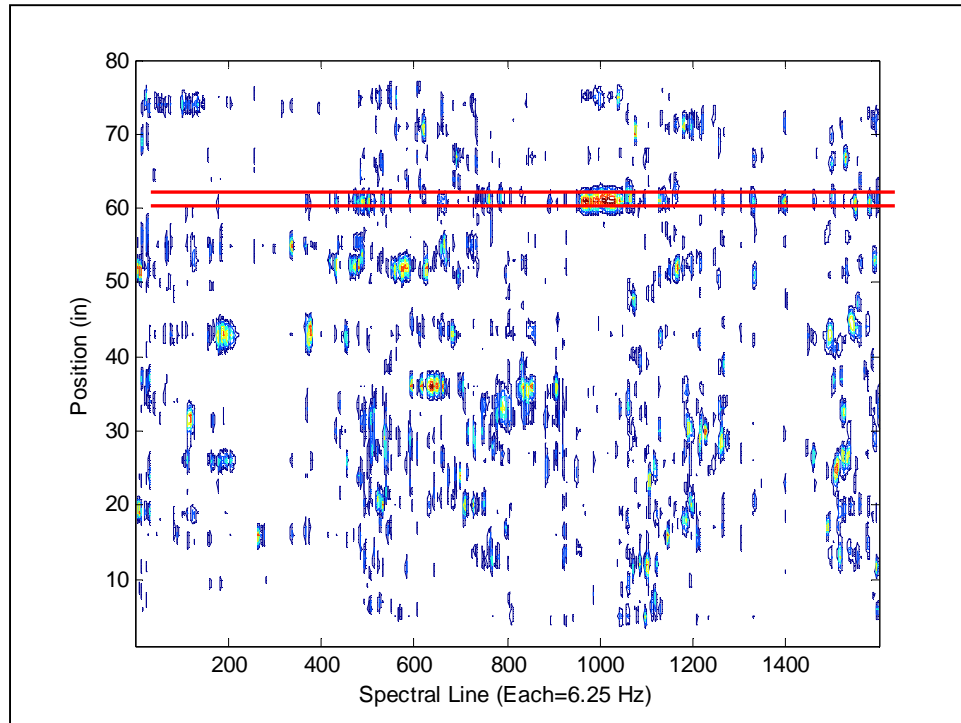


Figure 3.18 Damage index from roving excitation test on I-beam with two clamps at node 61

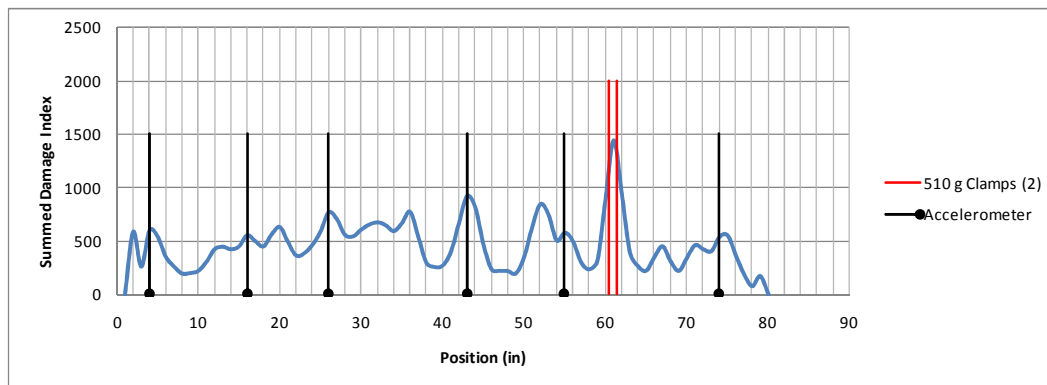


Figure 3.19 Summed damage index from roving excitation test on I-beam with two clamps at node 61

The ability to detect the clamps on the outer edge of the top flange is crucial because it shows that the identification of the two centerline masses was independent of the fact that impacts in the regions surrounding the masses were not actually on the centerline nodes. In the clamps test, added masses did not interfere with the centerline, so all nodes were impacted.

3.3 Scale Bridge

Laboratory testing was completed on a scale model of half of the FHWA # 31690 bridge. The model was constructed at approximately 1/6 scale and was made with two 10 foot long M6x4.4 junior I-beams and four 2 foot 6 inch long C3x3.5 channel sections, as shown in Figure 3.20. The channel sections were fixed to the I-beams with small angles and 1/4 inch bolts. Each bearing pad is made of two steel plates (3/4 inch and 1/2 inch thickness). One side of the model bridge utilizes a pintle in the top bearing plates, as does the actual bridge, to create a simply supported structure. Figure 3.21 shows the scale bridge in the laboratory.

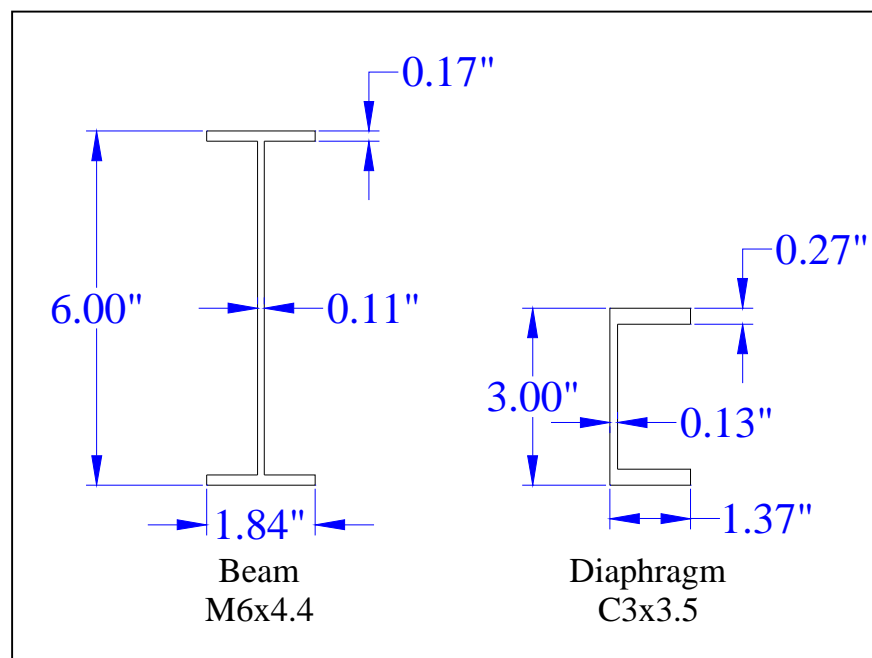


Figure 3.20 Scale bridge girder and diaphragm member cross sections



Figure 3.21 Scale bridge in the laboratory

3.3.1 Forced Vibration Test on Baseline Structure

Six uniaxial accelerometers were roved on the top flanges and bearing plates of each beam. A nodal mesh of one response point per six inches was used on the top flanges of the beams, and each corner of both end plates was measured for all four boundary conditions. The right beam was impacted in the downward vertical direction 20 inches from the end of the beam (node 12). Figure 3.22 shows a 3-D rendering of the structure with 98 labeled points (9 per boundary condition, 19 per beam, and 6 per diaphragm member), and Figure 3.23 shows a close-up of the right beam's first boundary condition with accelerometers on the first six response points. Frequencies from 0-10000 Hz were analyzed with a spectral density of 1 line/6.25 Hz.

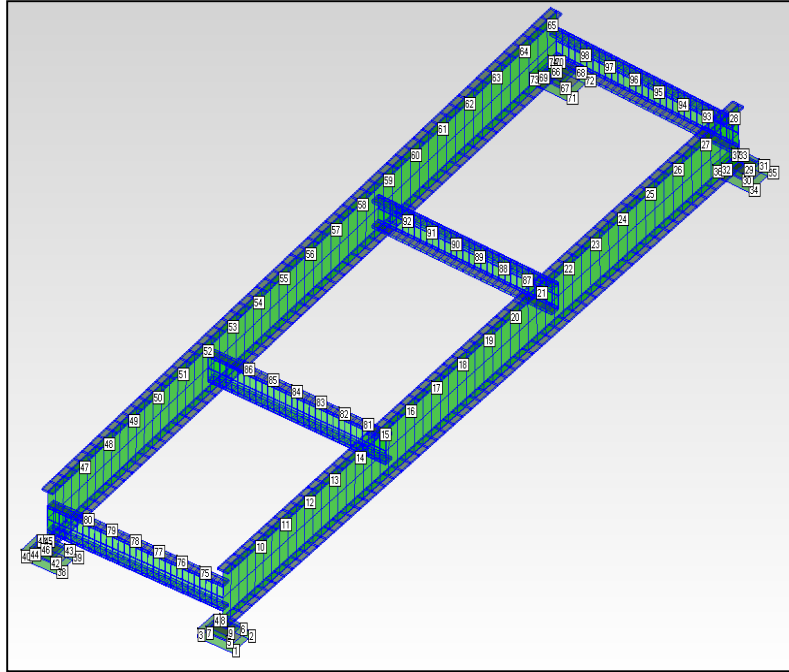


Figure 3.22 Rendering of scale bridge with 98 labeled response points



Figure 3.23 Accelerometers fixed with magnets to the first six response points of the scale bridge

3.3.1.1 Identification of Stiffened Areas

Figure 3.24 shows the overlaid FRFs from 0-2000 Hz collected from a roving response test on the scale bridge with no added damage. Some of the FRFs appear to have little agreement with the others because there were response points on various substructures such as end plates and diaphragm members.

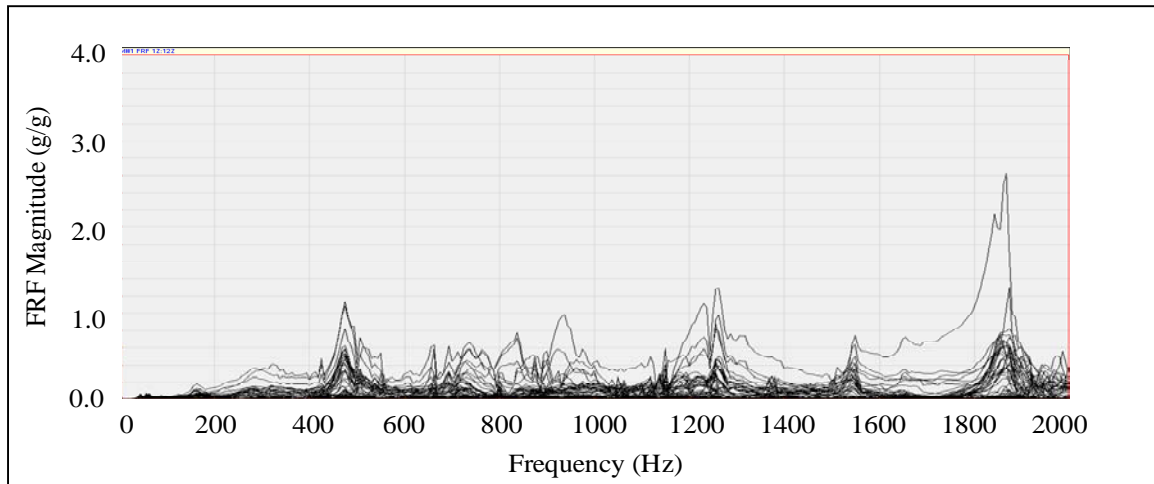


Figure 3.24 Overlaid FRFs from forced excitation, roving response test on baseline scale bridge

3.3.1.2 VBDI with Local Curve Fitting

Figures 3.25 and 3.26 show the damage indices for response points on the right and left beams, respectively. The solid red lines indicate the location of the intermediate diaphragm members at the third points of the 10 foot long beams. With no damage added to the structure, the use of a local curve fitting method should only show areas of the beam that are highly stiffened. The regions of color in Figures 3.25 and 3.26 are mostly within the intermediate diaphragm members, but also extend out past the channel sections for approximately 1 foot on each side. Therefore, for this structure with intermediate diaphragm members at third points, the stiffened region due to those members covers approximately the middle two-thirds of the structure.

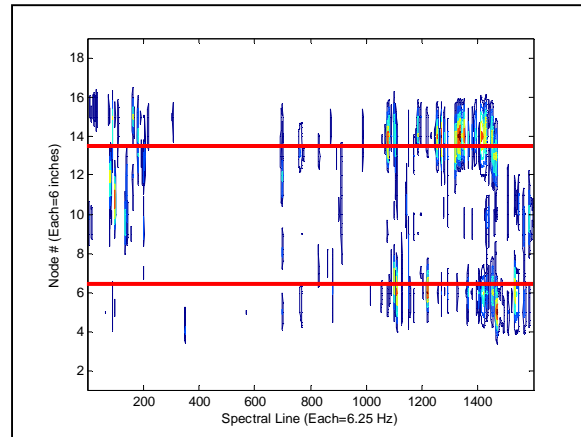


Figure 3.25 Damage index for right beam of baseline scale bridge

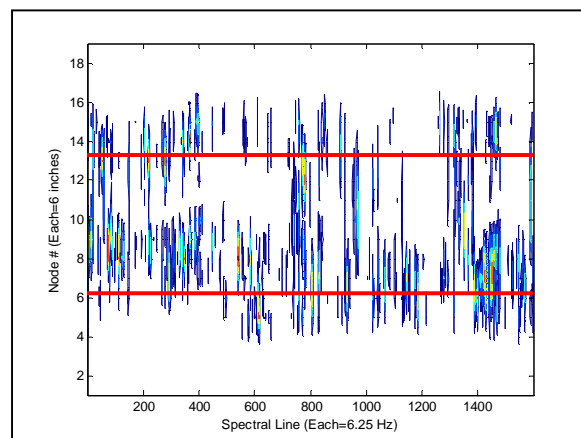


Figure 3.26 Damage index for left beam of baseline scale bridge

3.3.2 Forced Vibration Test with One Damage Location

Damage was added to one of the beams of the scale bridge to determine if the highly stiffened region in the middle of the structure has an effect on damage detection using the FRF curvature method. For this experiment, a 1500 g mass was fixed to the top flange of the right beam 20 inches from the far end (on node 16), as shown in Figure 3.27. This mass represents 3.2% of the total structure's mass (excluding the bearing plates) and 7.5% of the right beam only. Response points for this test were the same 98 points shown in Figure 3.22.



Figure 3.27 Mass (1500 g) added to top flange of the right beam, 20 inches from the far end

3.3.2.1 Identification of Mass

Figure 3.28 shows the overlaid FRFs from 0-2000 Hz collected from a roving response test on the scale bridge with the added damage. Once again, some of the FRFs appear to have little agreement with the others because there were response points on various substructures such as end plates and diaphragm members.

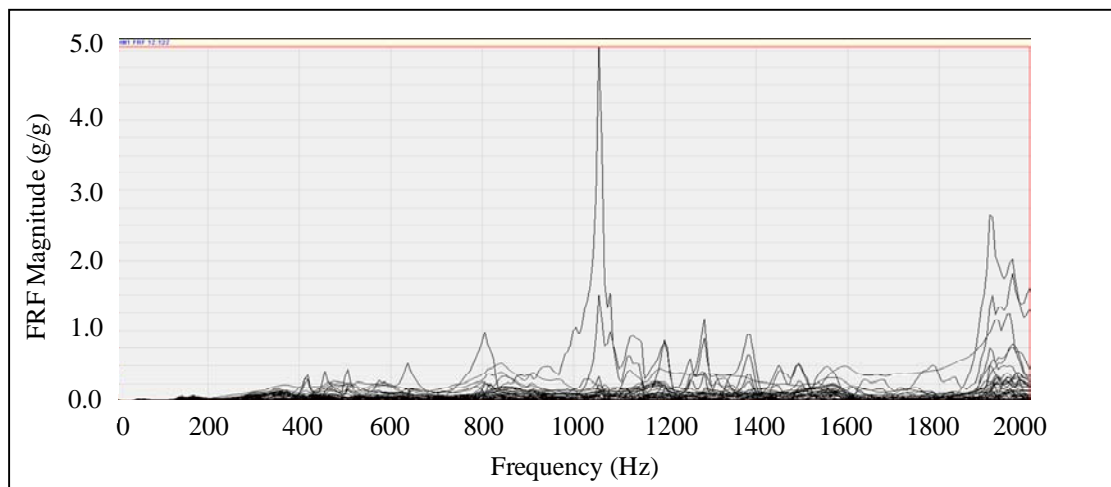


Figure 3.28 Overlaid FRFs from forced excitation, roving response test on damaged scale bridge

3.3.2.2 VBDI with Local Curve Fitting

Figures 3.29 and 3.30 show the damage indices for response points on the right and left beams, respectively. The solid red lines indicate the location of the intermediate diaphragm members at third points of the 10 foot long beams. The dashed black line in Figure 3.29 indicates the location of the mass. With no damage added to the left beam, the use of a local curve fitting method should only show areas of the beam that are highly stiffened. The regions of color in Figure 3.30 are mostly within the intermediate diaphragm members, but also extend out past the channel sections for approximately 1 foot on each side, exactly as with the baseline test. However, Figure 3.29 shows a much more random color distribution with no discernable pattern in curvature change. The stiffened middle area is no longer visible on the damage index for the right beam, and the impact point at node 2 is clearly visible. Unfortunately, although the method clearly indicates a difference in curvature change for the beam as a whole, it was unable to locate the damage at node 16.

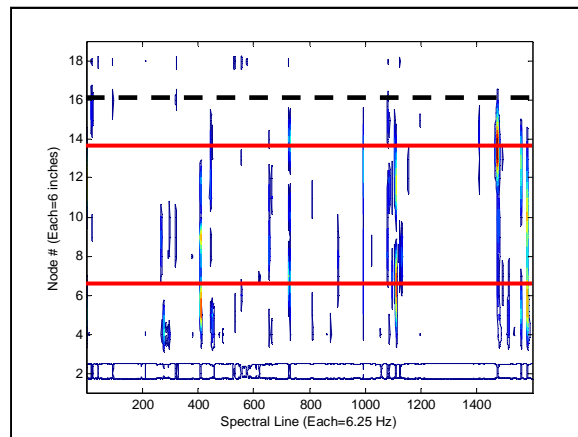


Figure 3.29 Damage index for damaged right beam of scale bridge

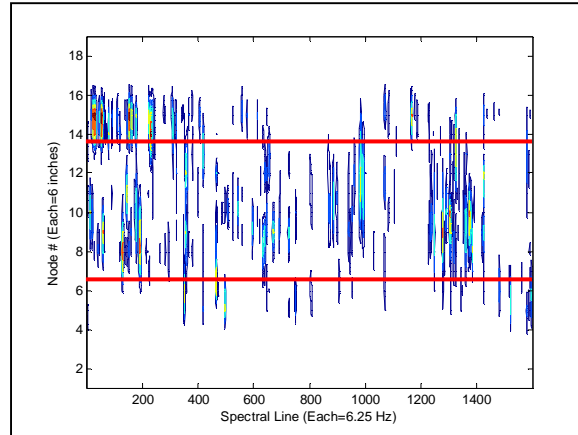


Figure 3.30 Damage index for undamaged left beam of baseline scale bridge

3.3.3 Global Operational Vibration Test with One Damage Location

To simulate operational traffic load on the scale bridge structure, the top flange of each beam was impacted once in the vertical direction at five different locations. Therefore, each data set is composed of 10 averaged impacts. The impact locations were at 20, 40, 60, 80, and 100 inches from the near end of both beams. Although the impact hammer was used to excite the structure, it was not used as a reference because the goal of the experiment was to simulate an operational environment where the excitation is difficult or impossible to measure. Therefore, a reference accelerometer was fixed to the top flange of the right beam at its midpoint. The roving response points were the same for this experiment as shown in Figure 3.23.

3.3.3.1 Analysis of Real Motion of Structure

Figure 3.31 shows 98 overlaid ODSFRFs from 0-500 Hz. By assigning the 98 ODSFRFs in Figure 3.31 to their actual measurement points as shown in Figure 3.23, the actual motion of each point of the structure relative to the reference response at the midpoint of the first beam can be calculated and animated using MEscape software. This allows users to visualize the effect of an average “operational load” traversing the scale bridge.

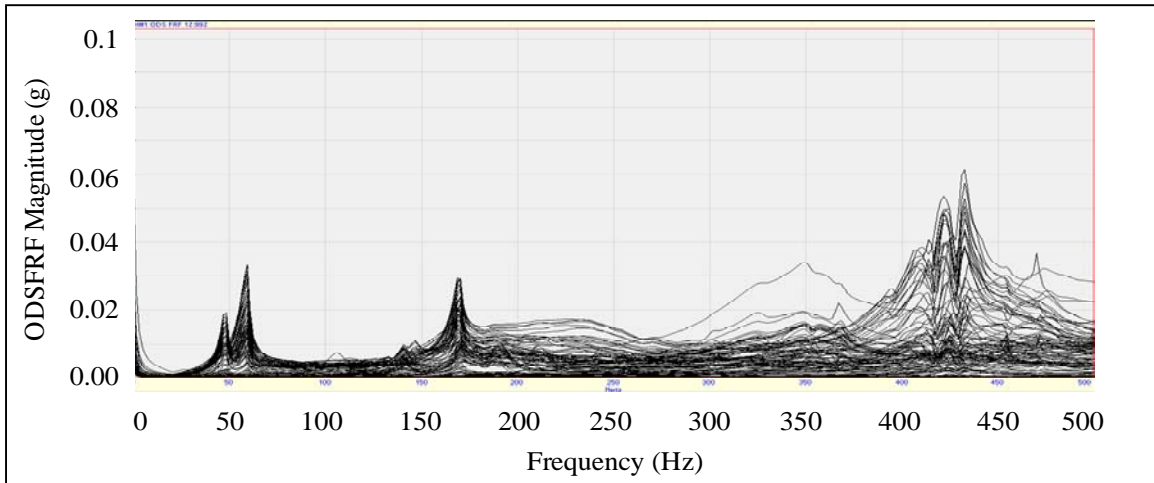


Figure 3.31 Overlaid FRFs from operational vibration, roving response test on damaged scale bridge

Figure 3.32 shows a screenshot of the animation of the ODSFRFs at 46.9 Hz, which causes the beams to experience first mode bending. At frequencies around the first MS, the diaphragm members experience various levels of first mode bending activity, but at the frequency shown they remain straight because both beams are bending with almost identical shapes. Figure 3.33 shows a screenshot of the animation of the ODSFRFs at 59.4 Hz, which causes the beams to experience first mode bending with a phase change (i.e., when right beam midpoint is minimum, left beam midpoint is maximum). Assuming a deck were present on top of the beams, it can be inferred that if the structure was often excited at this frequency, it would cause significant lateral cracking in the deck.

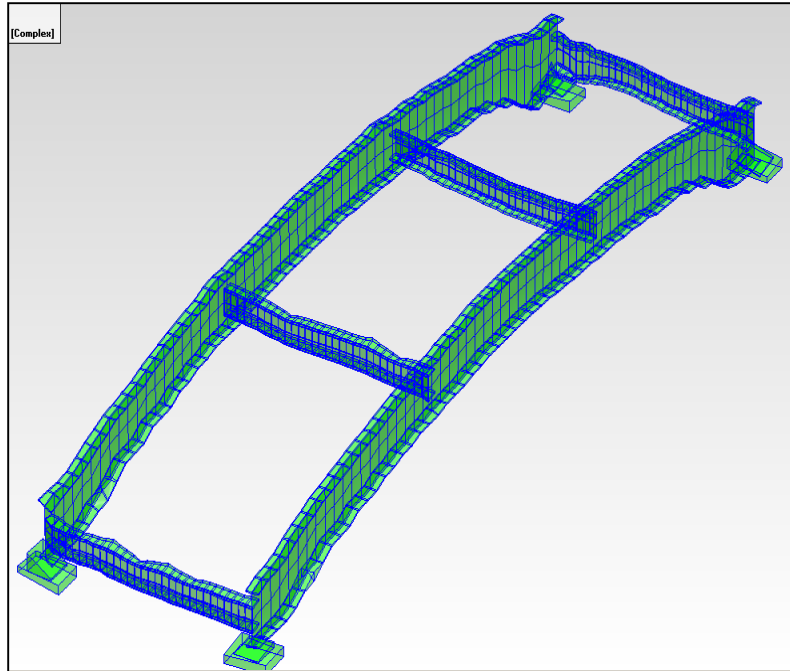


Figure 3.32 Screenshot of MEscape animation of scale bridge ODSFRFs at 46.9 Hz

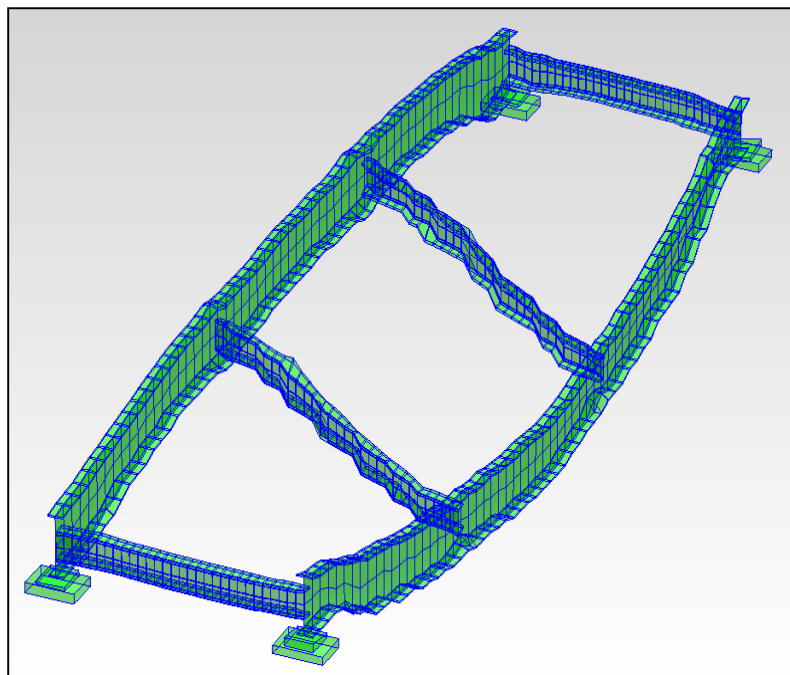


Figure 3.33 Screenshot of MEscape animation of scale bridge ODSFRFs at 59.4 Hz

CHAPTER 4

FIELD EXPERIMENTS

Field testing was completed on FHWA # 31690, a composite steel girder and concrete deck single span bridge. The bridge carries HWY 1 over a small natural creek between Black Diamond Road and Gingerich Road in Johnson County, Iowa. Having been constructed in 1949, the bridge has been rated functionally obsolete by Iowa DOT inspectors but is not structurally deficient and has an overall sufficiency rating of 37 (Iowa Department of Transportation). Spanning approximately 61 feet, the structure is primarily composed of four steel girders, a diaphragm with twelve channel members, and an 8 inch concrete deck. The exterior steel girders are W33x150, the interiors are W36x150, and the channels are C15x33.9 sections. Figure 4.1 shows a plan view of the bridge, and Figure 4.2 shows the member cross sections. Field investigations were carried out during two test dates: November 2009 and April 2010.

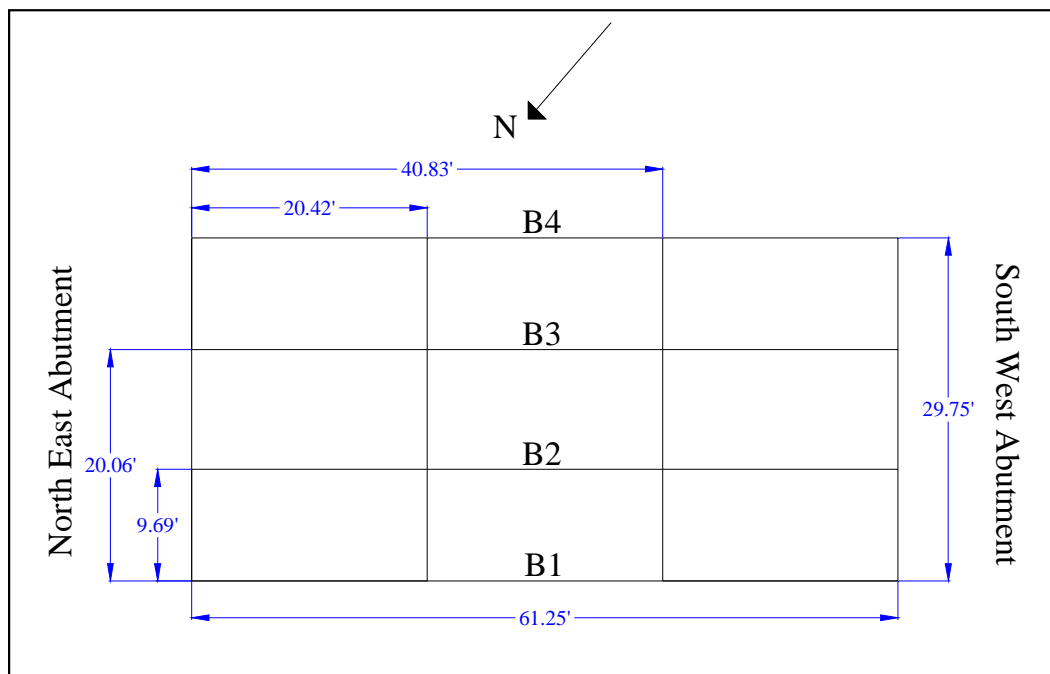


Figure 4.1 Plan view of tested field bridge (FHWA # 31690)

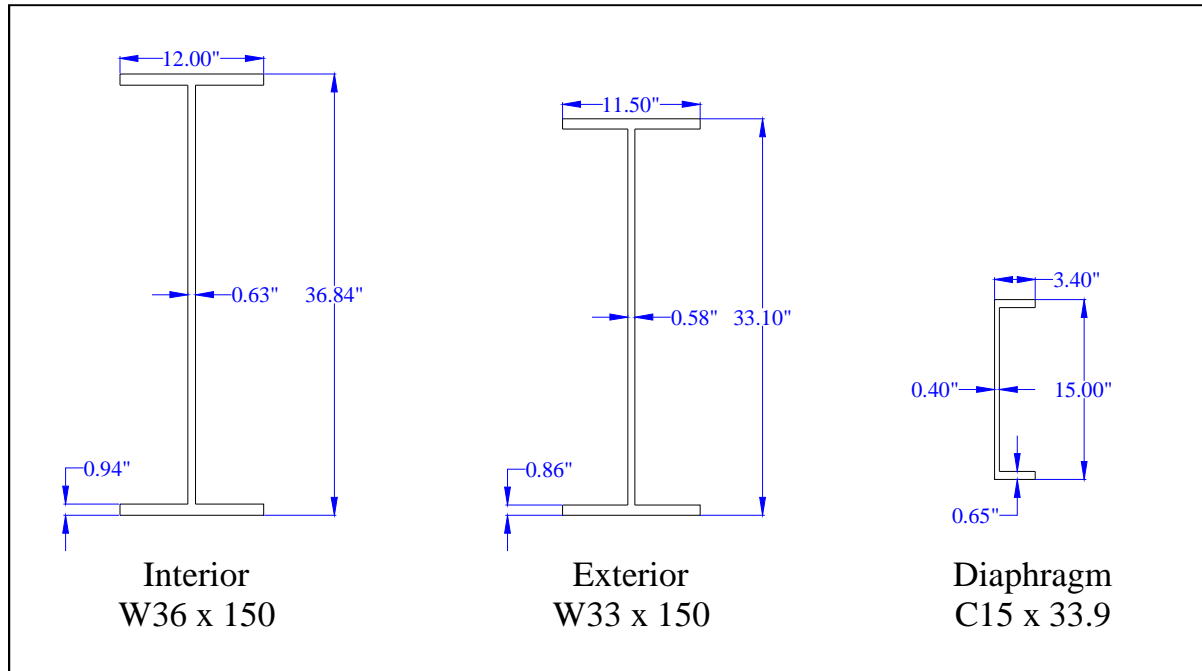


Figure 4.2 Schematic of field bridge girder and diaphragm member cross sections

4.1 Equipment

In the field a 5000 lbF range impulse hammer was used to excite the bridge. Three 5000 g range Dytran triaxial accelerometers and six 100 g range Dytran uniaxial accelerometers were used to determine the dynamic response of various structural elements. Typically, accelerometers were fixed to structures with a magnet, however in some cases wax was used with a magnet. An IOtech ZonicBook/618E Data Analyzer and an IOtech/650U were used to acquire data and construct FRF's. MEscape software was used to calculate mode shapes and ODSFRFs as well as to animate data. MATLAB was used to implement VBDI algorithms. Figure 4.3 shows a typical field operational vibration test setup.



Figure 4.3 Typical field operational vibration test setup

4.2 November 2009 Testing

The focus of this field investigation was to mark the steel girders to create a nodal mesh and acquire preliminary data for the entire bridge that could be used with the FRF Curvature Method. With the help of a DOT Snooper Truck, each steel girder was marked at one foot intervals on the bottom flange and web, as shown in Figure 4.4. One scaffolding tower was constructed under part of beam 1 so that the 12th node on that beam could serve as the fixed excitation point for the entire bridge, as shown in Figure 4.5.



Figure 4.4 Markings at one foot intervals on the web and bottom flange of each beam



Figure 4.5 Single scaffolding tower used to impact beam 1 at node 12

One triaxial accelerometer was roved per beam to each node on the bottom flanges, and the excitation point on beam 1 was impacted both in the lateral (out of plane) and vertical directions. Response data was collected in the lateral and vertical directions. Frequencies from 0-250 Hz were analyzed with a spectral density of 1 line/0.5 Hz. Figure 4.6 shows a schematic of the test setup for beam 1, and Figure 4.7 shows how the accelerometers were roved around the bridge. During this test, the DOT Snooper Truck was present on the bridge deck during the entire testing period in order to provide access to the girders.

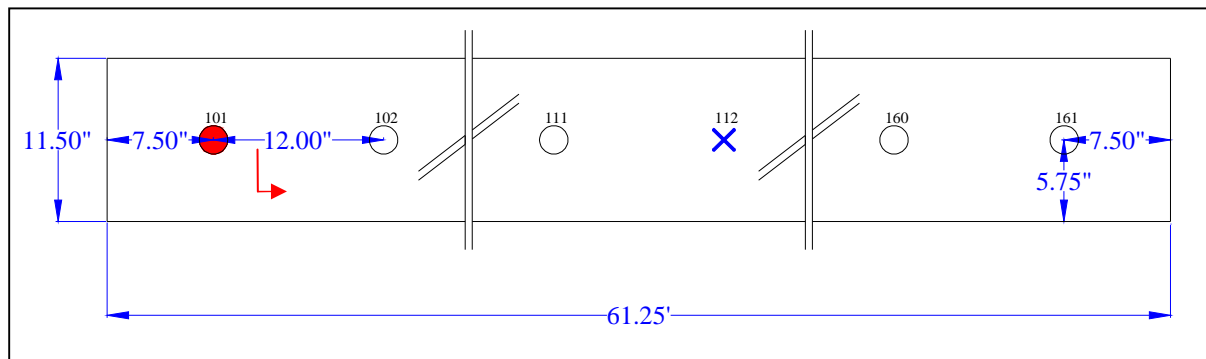


Figure 4.6 Schematic of forced vibration roving accelerometer test setup for bottom flange of beam 1 (one accelerometer per beam and impact point is stationary on beam 1 only)



Figure 4.7 Snooper truck and long poles used to access the bottom flange of each beam

4.2.1 Global Forced Vibration Beam Test

Figure 4.8 shows 228 overlaid vertical direction FRFs from 0-125 Hz (57 FRFs per beam). Although all these FRFs were measured together, having a common excitation point of node 12 on beam 1, for damage detection purposes FRFs for each beam are considered separately. Figures 4.9-4.12 show the damage indices for beams 1-4, respectively, with red lines indicating the location of intermediate diaphragm members. All results shown use the FRF curvature method with GSM only.

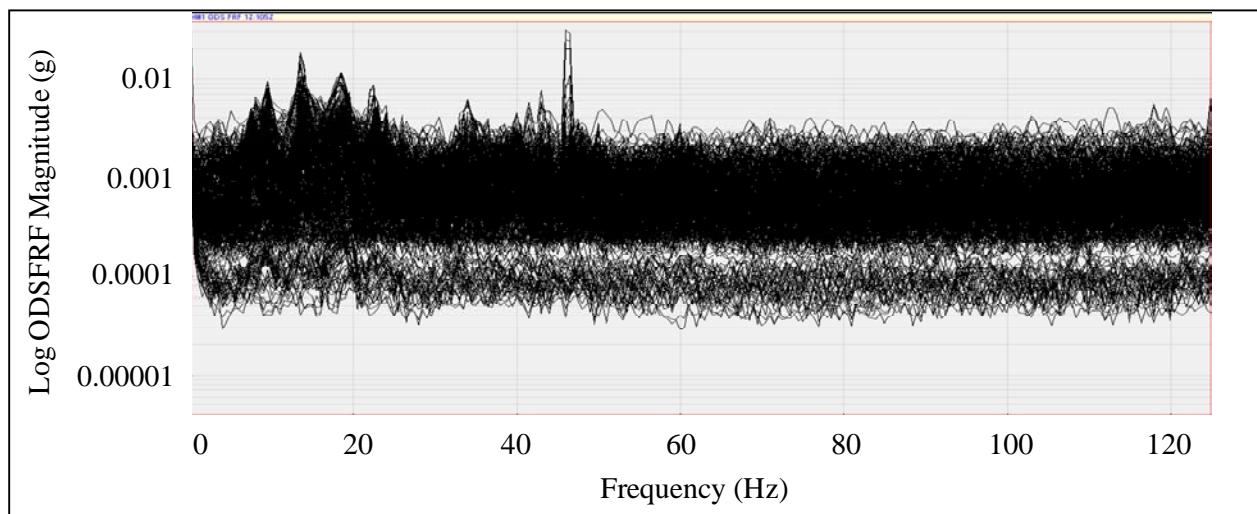


Figure 4.8 Overlaid FRFs from roving response test on all four beams of field bridge

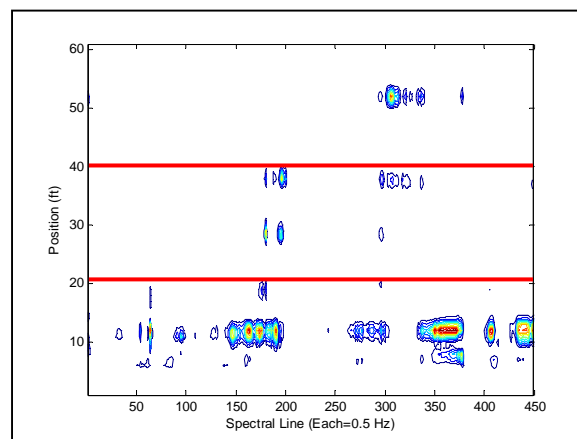


Figure 4.9 Damage Index for beam 1

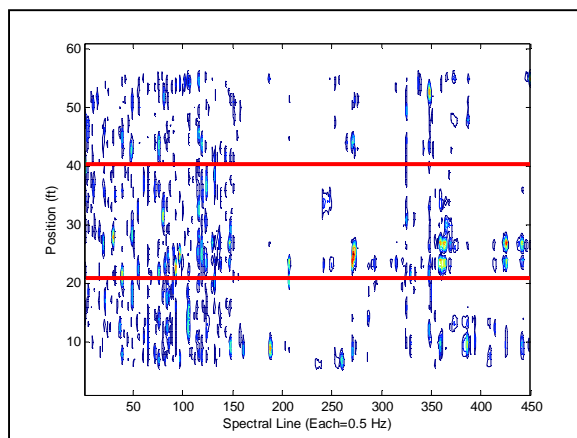


Figure 4.10 Damage Index for beam 2

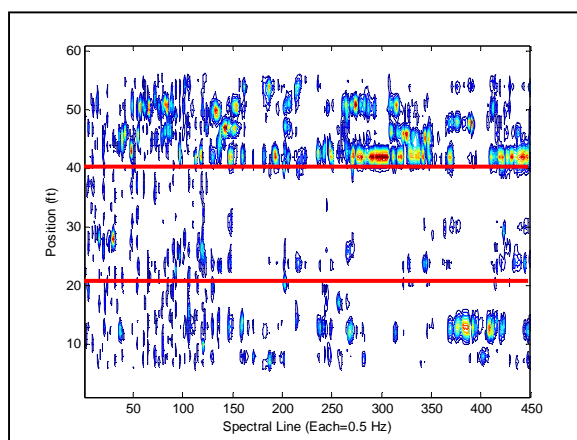


Figure 4.11 Damage index for beam 3

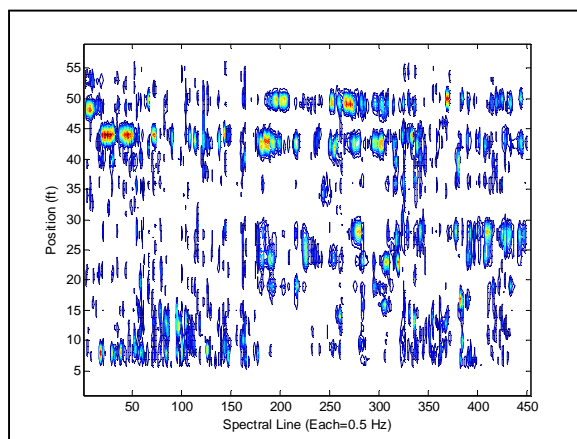


Figure 4.12 Damage Index for beam 4

Figure 4.9 shows the impact location 12 feet from the end of the beam and is much clearer than the rest of the damage indices. The damage index in Figure 4.9 also shows a stiff/damped region close to the first and second intermediate diaphragm members as well as in the middle of the structure and approximately 8 feet from each end. It is difficult to assess the effect of the 28 ton DOT Snooper truck on the damage index for beam 1. The change in FRF curvature at locations 8 feet from the end of the first beam could be due to the truck weight. Because the structure was excited on beam 1, the vibration dissipates significantly before it reaches the rest of the beams due to significant damping in the structure. It can be assumed that the mass of the DOT Snooper truck magnified this damping. Therefore, Figures 4.10-4.12 represent data largely affected by noise, and very little information can be gathered from them.

4.3 April 2010 Testing

The focus of this field investigation was much broader than the November test. The goal was to acquire enough data (both forced vibration and operational vibration data) to fully analyze the girders, diaphragm members, boundary conditions, and abutments. To accomplish these tasks, scaffolding was constructed beneath the entire structure, as shown in Figure 4.13. This eliminated the need for a large Snooper truck to be on the bridge deck during testing.



Figure 4.13 Scaffolding that provided access to the entire superstructure

4.3.1 Independent Forced Vibration Beam Test

The first test that was ran was a forced vibration test where the bottom flange of each beam's measured response was gathered independent of the rest of the structure. Beam 1 was impacted at node 16 and three accelerometers were roved every foot until the end of the beam, as shown in Figure 4.14. Figure 4.15 shows the equipment setup and the excitation of a beam. This process was repeated for each beam, yielding four independent forced vibration tests with 61 measurements each.

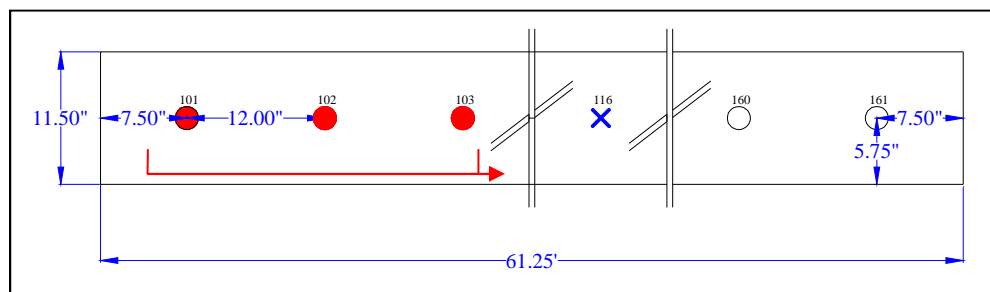


Figure 4.14 Schematic of forced vibration roving accelerometer test setup for bottom flange of beam 1 (three accelerometers per beam and impact point is on node 16 of each beam)



Figure 4.15 Data acquisition system setup with large impact hammer used to excite each beam

4.3.1.1 VBDI with Local Curve Fitting

FRFs from 0-125 Hz gathered from four independent forced vibration beam tests are shown in Figures 4.16-4.19. Because each of these FRFs was taken with its own excitation point (16 feet from end of beam for each), the FRFs shown are much clearer than the FRF in Figure 4.8, especially in the first 60 Hz. All four FRFs show many closely spaced, low-frequency modes. The shape of the FRFs for the exterior beams (4.16 and 4.19) are very similar to each other and indicate very clear modes until approximately 85 Hz. Likewise, the shape of the FRFs for the interior beams (4.17 and 4.18) are similar to each other but seem to indicate less natural frequencies.

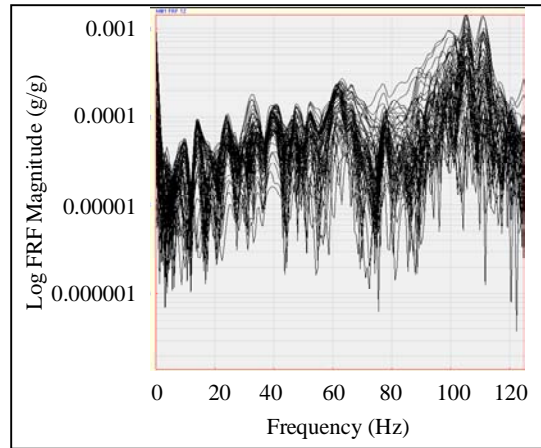


Figure 4.16 Overlaid FRFs for roving response test on beam 1

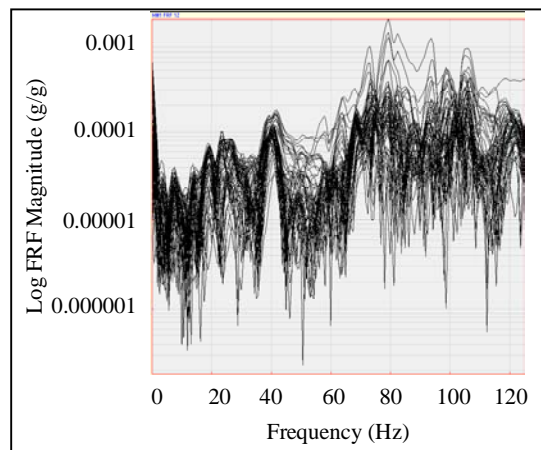


Figure 4.17 Overlaid FRFs for roving response test on beam 2

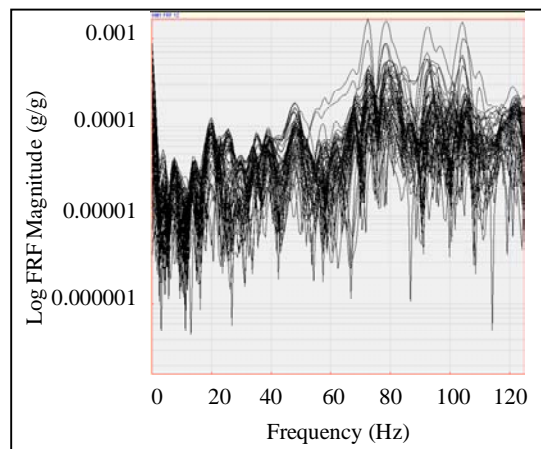


Figure 4.18 Overlaid FRFs for roving response test on beam 3

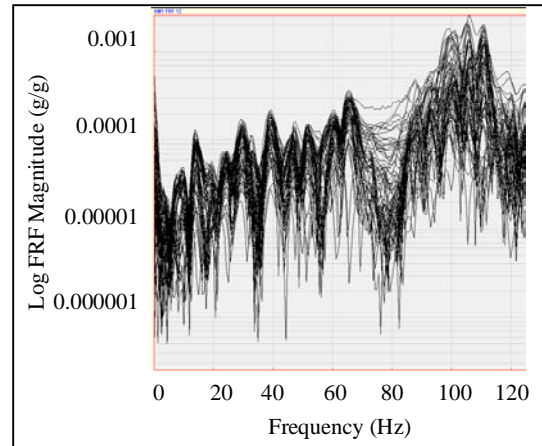


Figure 4.19 Overlaid FRFs for roving response test on beam 4

Figures 4.20-4.23 show the damage indices for beams 1-4, respectively, with red lines indicating the location of intermediate diaphragm members. All results shown use the FRF curvature method with GSM only. All four damage indices in Figures 4.20-4.23 show the presence of the impact location near node 16 very clearly. Damage indices for the exterior beams (1 and 4) seem to show a line of curvature change near the intermediate diaphragm members. Unfortunately, besides the impact location, there is very little difference in FRF curvature at all other points in the interior beams, including regions close to the intermediate diaphragm members. Although the method of impacting each beam independently has produced very high-quality FRFs, it does not seem robust in its ability to detect areas of high stiffness and may not be capable of detecting damage on large structures.

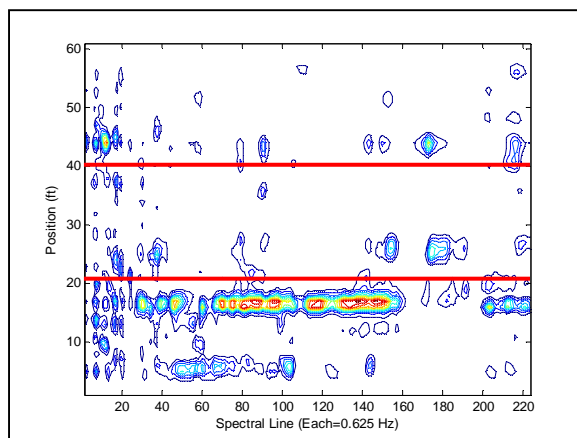


Figure 4.20 Damage index for beam 1

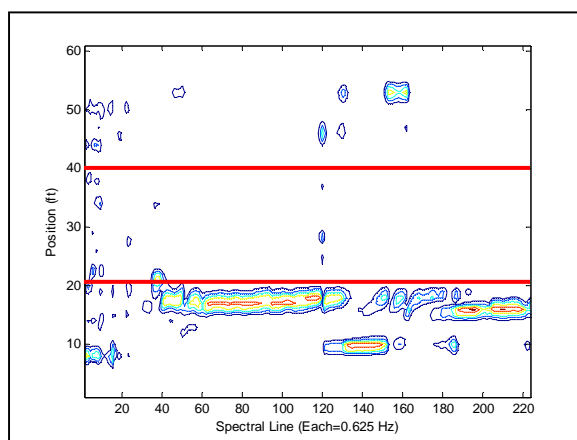


Figure 4.21 Damage index for beam 2

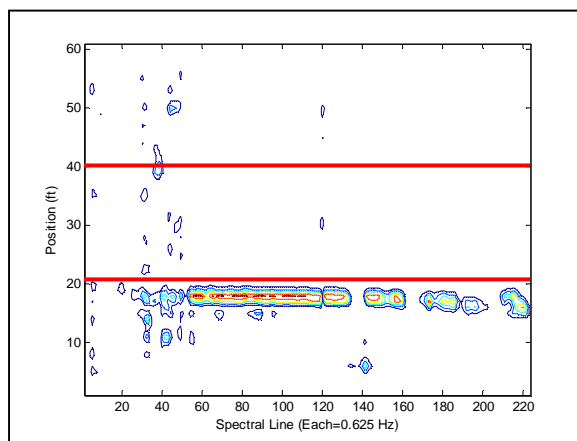


Figure 4.22 Damage Index for beam 3

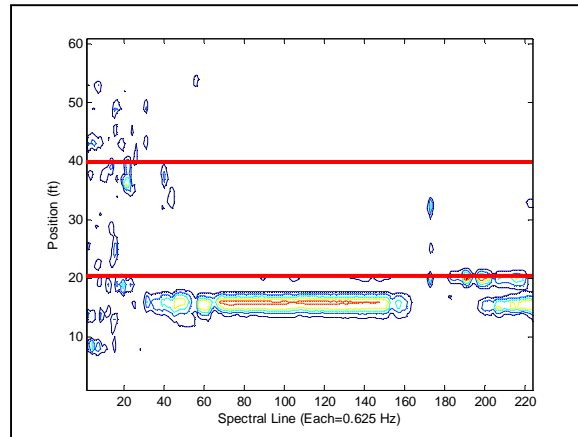


Figure 4.23 Damage Index for beam 4

4.3.2 Global Operational Vibration Bridge Test

The second test that was run in April 2010 was an operational vibration test where the majority of the structure was measured together. Figure 4.24 shows a 3-D rendering of the bridge with 440 labeled points (70 per beam, 10 per diaphragm, and 20 per abutment). Traffic loading was used as the operational vibration, and measurement was triggered by a reference accelerometer that was fixed to the bottom flange of the third beam at midspan (see 4.24A). A ten car average was used, meaning that after ten automobiles triggered the reference accelerometer, the response accelerometers were moved to the next measurement location. Five uniaxial accelerometers were used as response accelerometers and roved around the structure, including each girder, each diaphragm member, and the abutment wall. The nodal mesh on the beams was one measurement point per four inches for the two feet extending out from each end (see 4.24B) and one measurement point per foot for the remaining length of the beam (see 4.24C). The nodal mesh for each diaphragm member was one measurement per foot (see 4.24D). The nodal mesh for the abutment was one measurement per four inches directly below each beam for 20 inches (see 4.24E). This setup yielded one operational vibration test with 440

measurements. Figures 4.25 through 4.27 show the operational vibration response measurement of a beam, diaphragm member, and strip of abutment, respectively.

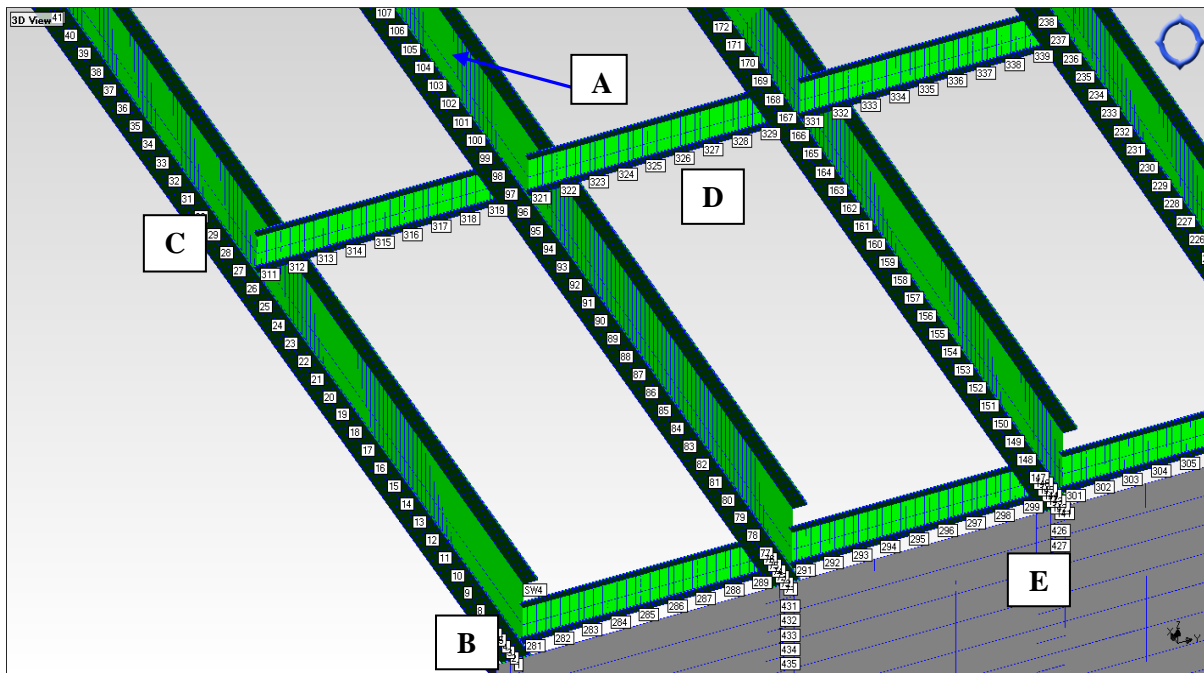


Figure 4.24 Rendering of the bridge with the reference response location (A), concentrated beam mesh near boundary conditions (B), normal beam mesh (C), diaphragm member mesh (D), and abutment mesh (E)



Figure 4.25 Operational vibration response measurement of a beam near the boundary condition



Figure 4.26 Operational vibration response measurement of a diaphragm member



Figure 4.27 Operational vibration response measurement of a strip of the vertical face of an abutment

4.3.2.1 Operational VBDI with Local Curve Fitting

Figure 4.28 shows 440 overlaid ODSFRFs from 0-125 Hz (70 per beam, 10 per diaphragm, and 20 per abutment). The ODSFRFs with magnitudes much lower than the others are from response points on the abutments, which were excited less by the traffic load. Because the abutment data sets consisted of eight placements of five response points each, not enough data was obtained in each placement to calculate meaningful damage indices. Damage detection algorithms were used on beam and diaphragm ODSFRFs extracted from the data shown in Figure 4.28.

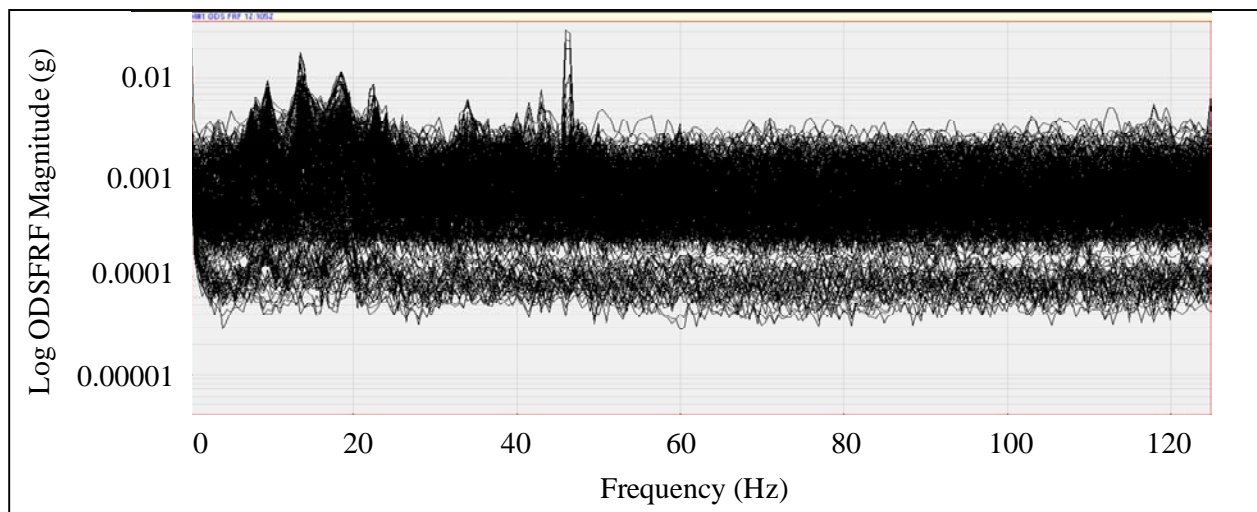


Figure 4.28 Overlaid ODSFRFs from global operational vibration test

4.3.2.2 Beams

Figures 4.29-4.32 show summed damage indices for beams 1-4, respectively. The summed damage indices of the exterior beams in Figures 4.29 and 4.32 show a distinct increase in ODSFRF curvature around and in between the intermediate diaphragm members, shown with solid red lines. This is to be expected, due to the significant addition of stiffness to the region around each diaphragm member. However, the interior beams show a much more spread out

region of changed ODSFRF curvature. This could be due to a larger area of high stiffness caused by diaphragm members on either side of an interior beam's web.

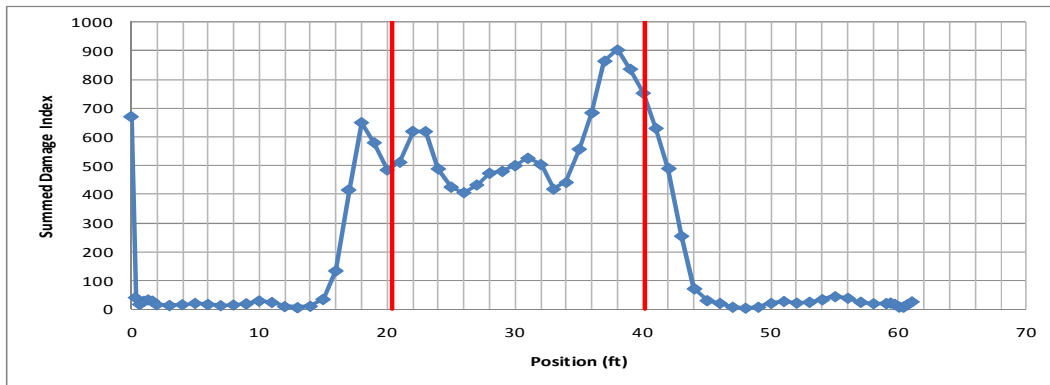


Figure 4.29 Summed damage index for beam 1

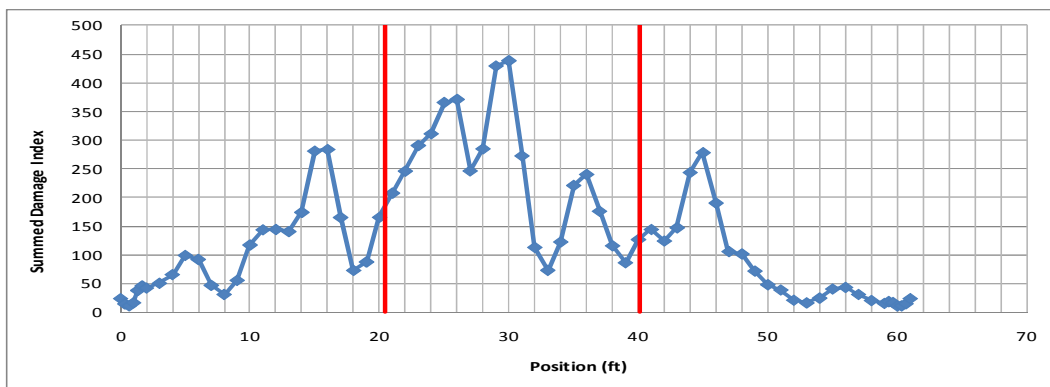


Figure 4.30 Summed damage index for beam 2

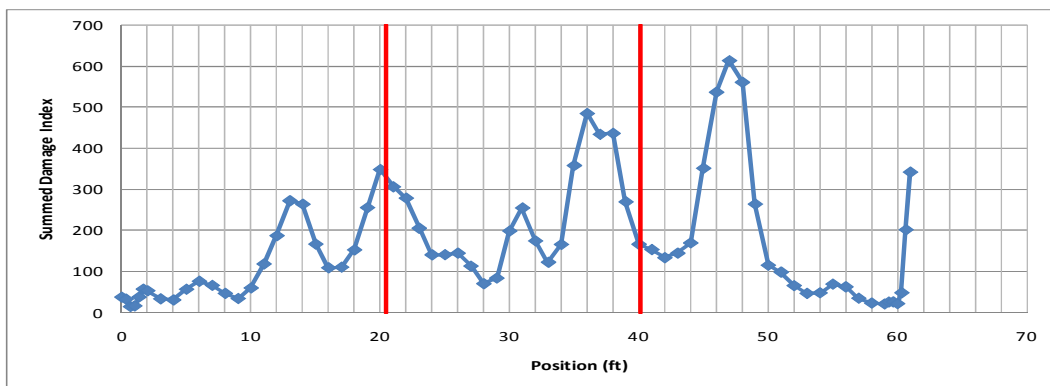


Figure 4.31 Summed Damage index for beam 3

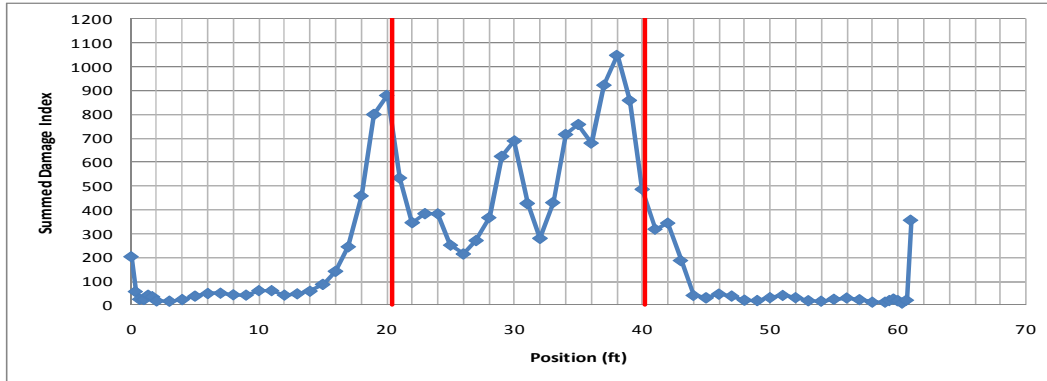


Figure 4.32 Summed damage index for beam 4

The summed damage indices presented above seem to accurately indicate the behavior of the beams in a very global sense (i.e., the presence of a highly stiffened middle region was detected). If extreme damage was present on the beams, it may be evident from these plots; however, it is unlikely that small to moderate levels of damage can be detected using operational data with the curvature method and GSM.

4.3.2.3 Diaphragm Members

Figures 4.33-4.36 show summed damage indices for diaphragm rows 1-4, respectively. The dashed black lines indicate the location of interior beams. Therefore, each plot actually shows the summed damage index of three independent channel sections. The summed damage indices do not seem to indicate any discernable regions of changed dynamic characteristics for the four diaphragm rows. Because the diaphragm members are often much larger sections than necessary (C15x33.9 is the DOT minimum required section), it is unlikely that damage would be present in these members. If damage were present in the diaphragm members, it is not evident whether or not the ODSFRF curvature method would be capable of detecting and locating it.

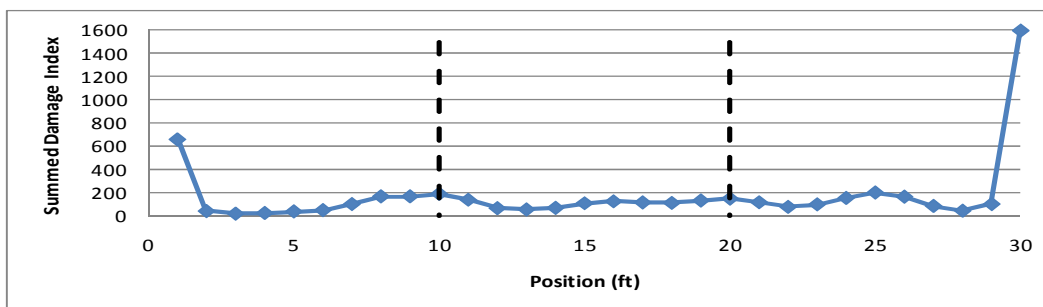


Figure 4.33 Summed Damage index for diaphragm row 1

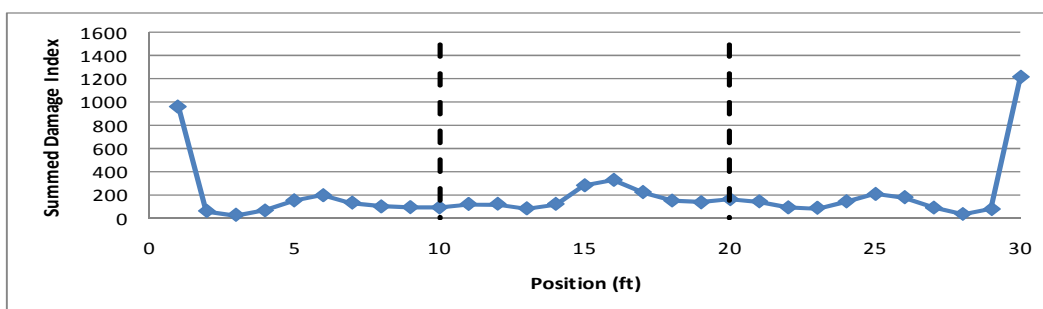


Figure 4.34 Summed damage index for diaphragm row 2

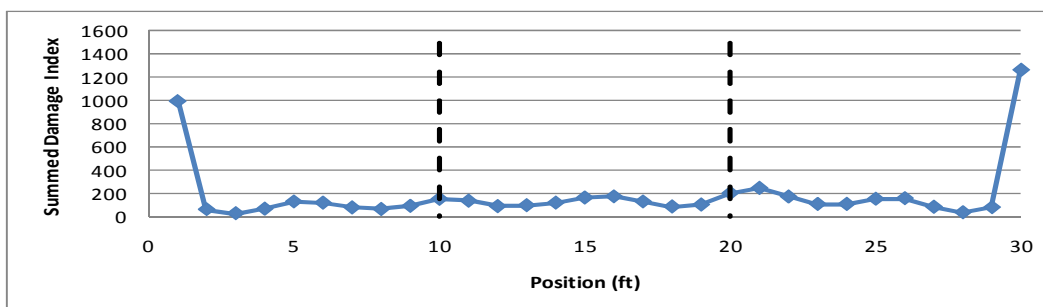


Figure 4.35 Summed damage index for diaphragm row 3

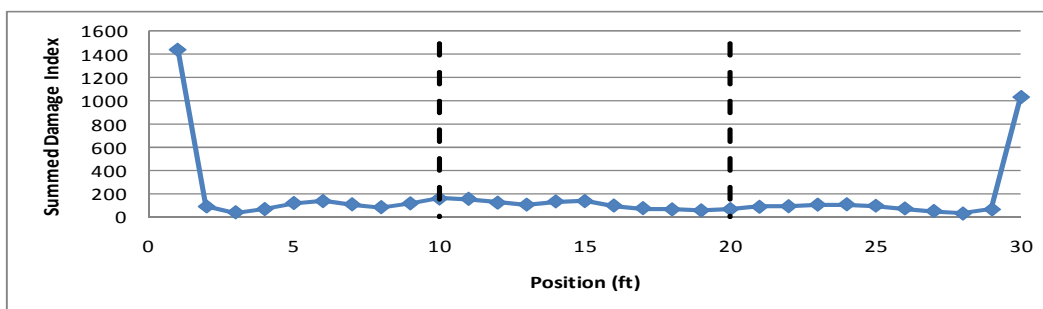


Figure 4.36 Summed damage index for diaphragm row 4

4.3.3 ORWA

After April 2010 field testing, a methodology was developed to utilize the operational response and forced excitation response data in a different way. Instead of focusing on detecting damage, the same data used in VBDI was instead animated using MEscape software. Also, the time waveforms of traffic passing over the bridge were analyzed. This new way of looking at the same vibration data focuses on correlating existing bridge damage with structural motion due to operational traffic loading.

4.3.3.1 Frequency-domain Analysis of Traffic

To determine the effect of everyday traffic passing over the bridge, the response of the reference accelerometer from every recorded operational vibration data set was analyzed. Figure 4.37 shows overlaid time waveforms from 880 different automobiles. As shown, most time waveforms had vibration typically lasting for less than 1.5 seconds

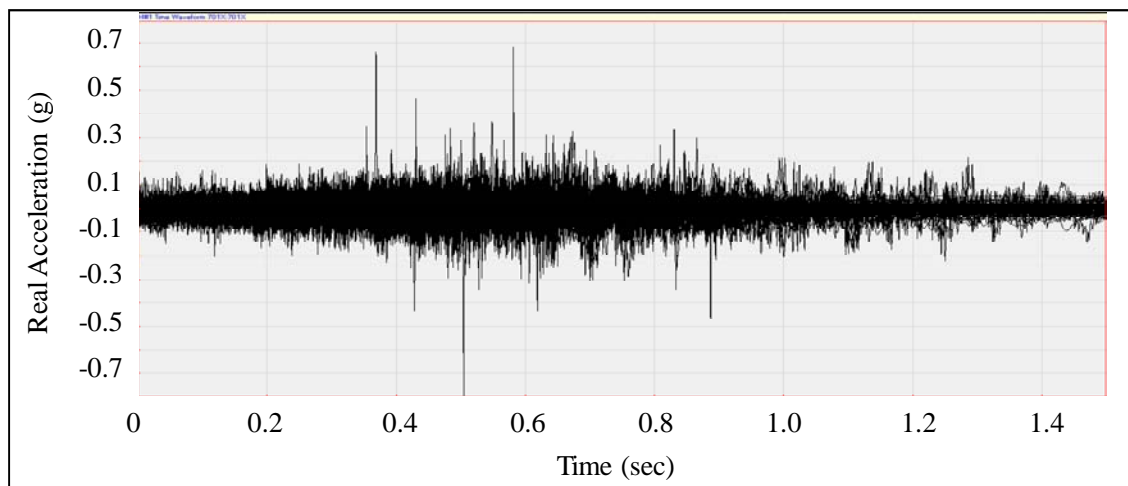


Figure 4.37 Overlaid time waveforms from 880 different automobiles

To analyze the frequency components of the average automobile, the Fourier transform of the 880 time waveforms was calculated, resulting in overlaid frequency waveforms shown in Figure 4.38. As shown, there is significant frequency contribution of most, if not all, data

samples at approximately 13.5 Hz and all acceleration magnitudes are below 0.03 g. The highest amplitude of the frequency waveform is also at 13.5 Hz. Other significant frequencies are 7.5 Hz, 15.5-16.5 Hz, 19.5-24 Hz, and 35 Hz.

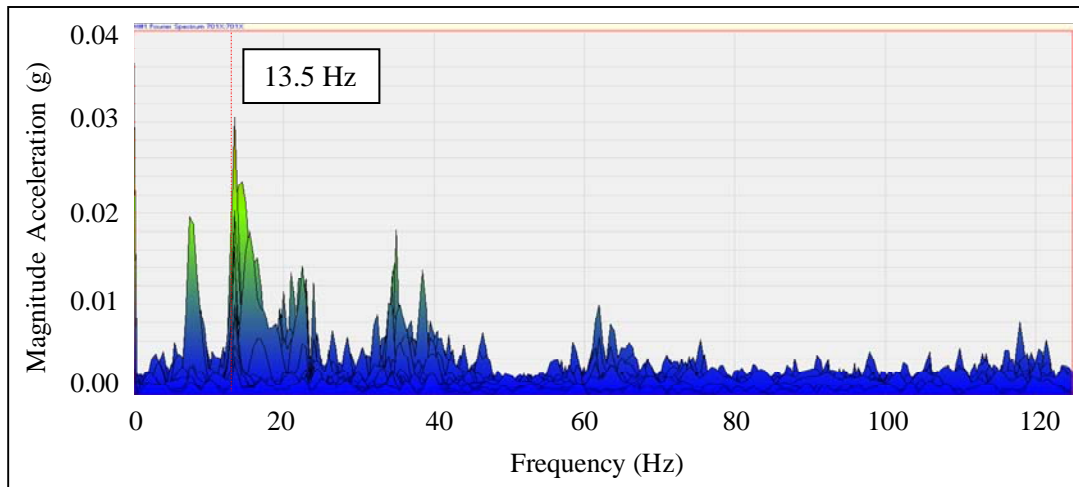


Figure 4.38 Overlaid frequency waveforms from 880 different automobiles

4.3.3.2 Analysis of True Motion of Entire Structure

By assigning the 440 ODSFRFs in Figure 4.28 to their actual measurement points as shown in Figure 4.24, the actual motion of each point of the structure relative to the reference response at the midpoint of the third beam can be calculated and animated using MScope software. This allows users to visualize the effect of an average automobile traversing the bridge. Figure 4.39 shows a screenshot of the animation of the ODSFRFs at 13.5 Hz, which causes the intermediate diaphragm members to have first mode bending. Although the animation of the girders seems to be too noisy to indicate a clear bending pattern, the motion of the diaphragm members dictates that the beams must be experiencing bending similar to the first MS. To verify this hypothesis, the FRF results from independent beam tests (Section 4.3.1) were animated at a frequency of 13.5 Hz. As shown in the screenshot in Figure 4.40, the beams experience first mode bending at 13.5 Hz when measured independently.

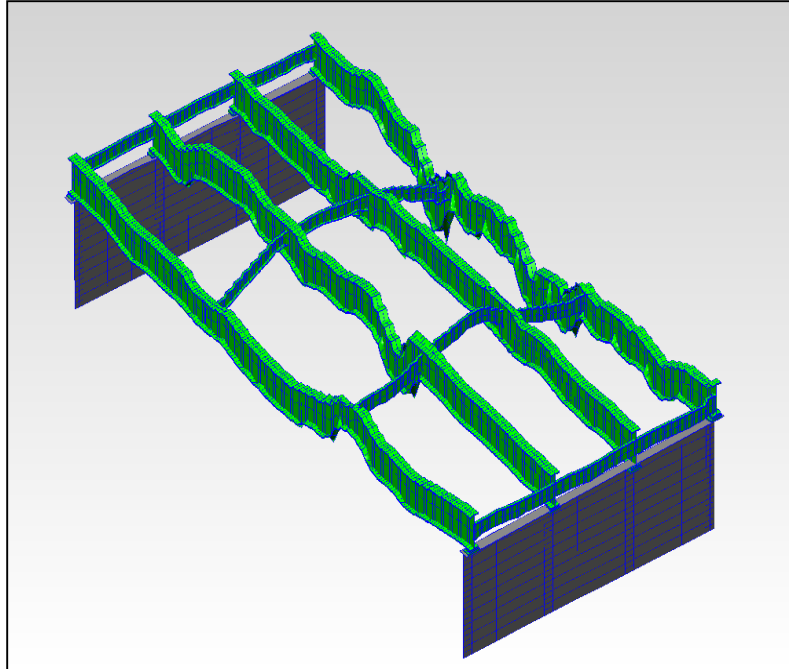


Figure 4.39 Screenshot of MEscope animation of entire bridge ODSFRFs at 13.5 Hz

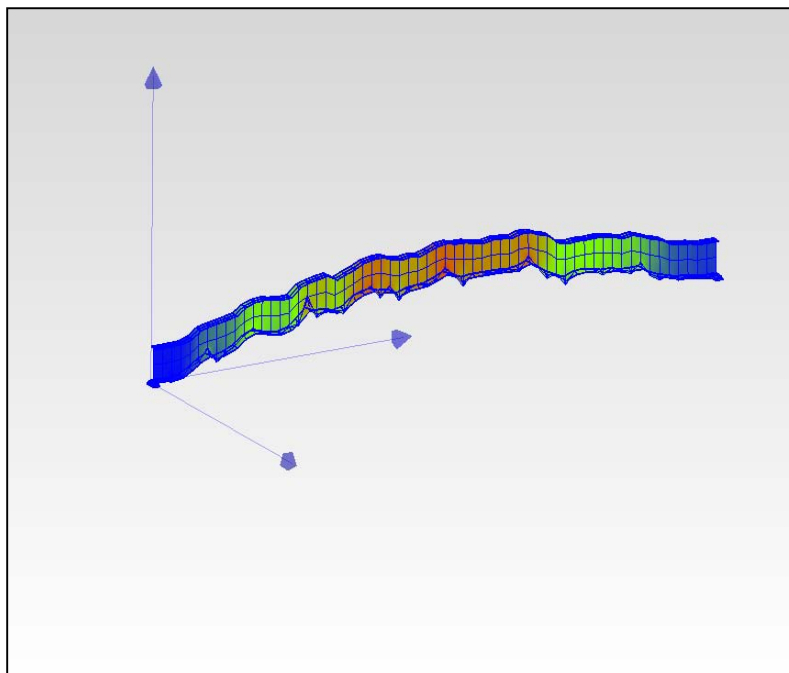


Figure 4.40 Screenshot of MEscope animation of independent beam FRFs at 13.5 Hz

4.3.3.3 Operational Excitation at 13.5 Hz

The first vertical bending mode causes the two interior girders to experience upwards displacement while at the same time that the exterior girders experience downward displacement. Because FHWA #31690 uses composite action between the concrete deck and I-girders, it can be assumed that the motion of the deck resembles that of the girders. Therefore, lateral cracking in the bottom of the concrete deck should be expected near the diaphragm members since the waveform analysis showed that applied excitation causes the structure to experience first vertical mode bending often. As expected there was significant lateral cracking noticed in the concrete deck above the southwestern intermediate diaphragm row, as shown in Figure 4.41.



Figure 4.41 Lateral surface crack in concrete deck near midspan of bridge

Furthermore, the first bending mode of the diaphragm members must cause torsion in the exterior beams, assuming the bolt connections are rigid. To understand the effects of the first vertical bending mode of the structure on the abutment, the animation of response points was

focused on the northeast abutment of beam #4, as shown in Figure 4.42. As shown, the top three response points on the face of the abutment are moving up and down and are not in phase with each other. This relative motion between response points is in essence tension-compression action in the concrete. Although the screenshot in Fig. 9 is focused on an exterior beam, the interior beams also showed similar tension-compression action. This is to be expected because each beam is experiencing first mode bending at 13.5 Hz.

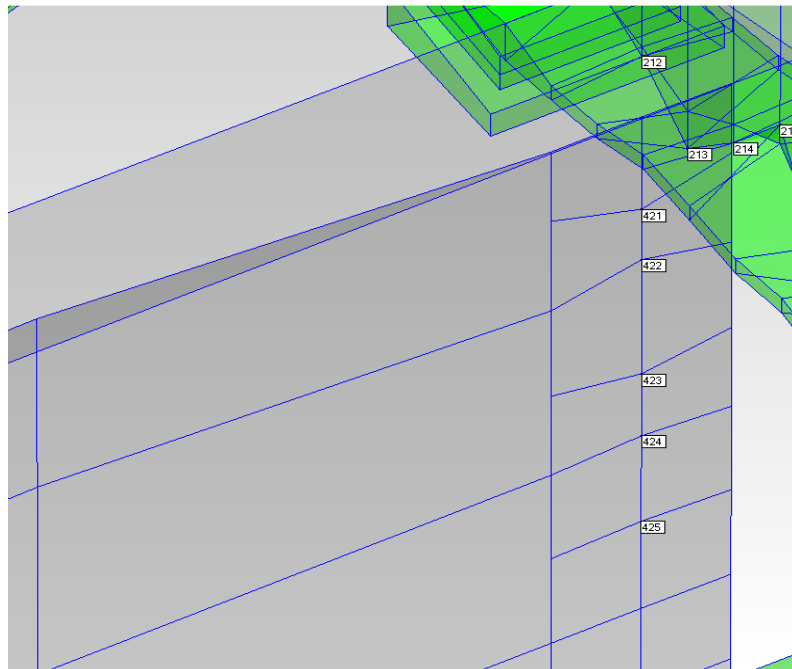


Figure 4.42 Screenshot of MEscape NE4 boundary condition animation of ODSFRFs at 13.5 Hz

The first vertical bending mode of the diaphragm members must cause torsion in the exterior beams, assuming the bolt connections are rigid. This is because the maximum upward displacement of the interior beams occurs while the exterior beams experience maximum downward displacement. Therefore, the abutment seat is being subjected to back-and-forth torsional motion beneath the exterior beams as shown in Figure 4.43. Figure 4.44 shows a schematic of the motion zoomed in at a single exterior beam. Somewhat diagonal cracking in

the abutment face should be expected beneath the exterior beams due to a combination of torsional and tension-compression action since the waveform analysis showed that applied excitation causes the structure to experience first vertical mode bending often. There was significant diagonal cracking propagating from the bearing plates noticed in the northeast abutment below beam #4, as shown in Figure 4.45. Also, moderate corner cracking was observed in the southwest abutment below beam #4. However, only minor cracking existed in both abutments below beam #1.

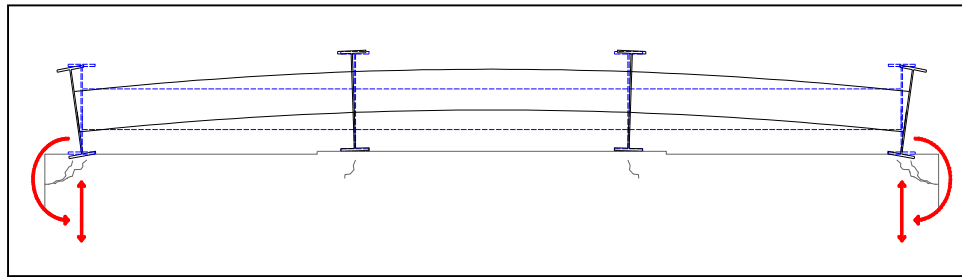


Figure 4.43 Schematic of torsional and compression-tension action caused by first bending mode of diaphragm members

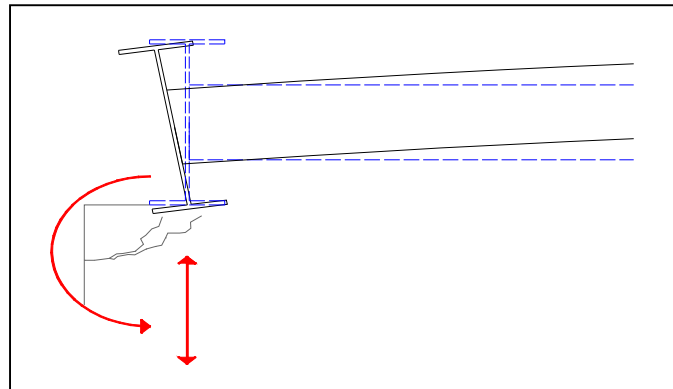


Figure 4.44 Zoomed-in schematic of torsional and compression-tension action caused by first bending mode of diaphragm members



Figure 4.45 Large diagonal crack in the northeast abutment wall beneath beam 4

4.3.3.4 Independent Forced Vibration End Beam Test

The third test that was run during the April 2010 testing was a forced vibration test that focused on the boundary conditions of the beams. Two end plate assemblies were chosen for analysis: northeast support of beam 3 and northeast support of beam 4. A fine mesh of response points was used that included accelerometers on the bottom flange on either side of the web and the bearing plates supporting the beam. Also, the concrete seat in front of the boundary condition of beam 3 was measured. A point ten feet from the end of each beam was chosen as the excitation point and was impacted in the vertical direction. Figure 4.46 shows a 3-D rendering of a typical beam end with 42 labeled points (30 on the beam flange, 6 on the lowest bearing pad, and 6 on the concrete seat). Beam 4 had noticeable deterioration of the bottom flange near the boundary condition, and the same area on beam 3 was relatively clean, as shown in Figures 4.47 and 4.48.

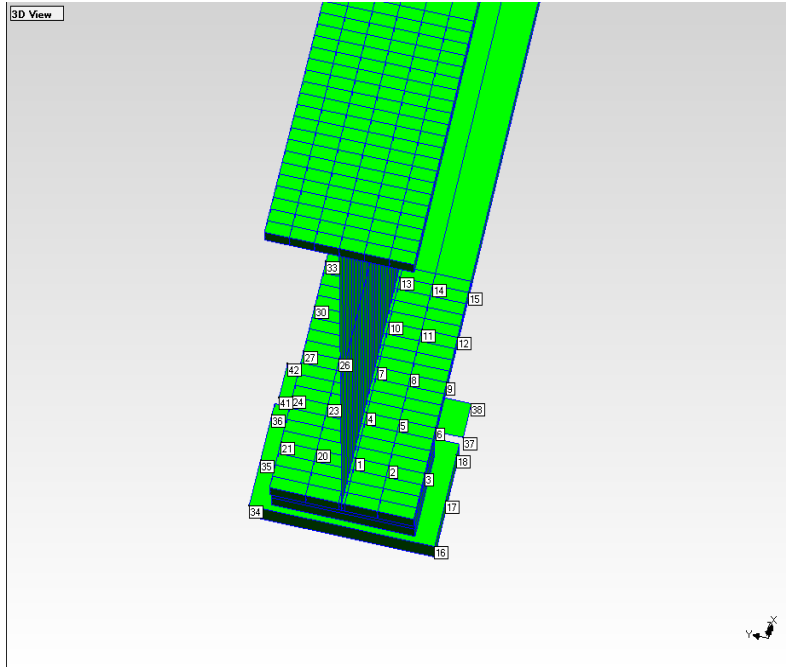


Figure 4.46 Rendering of a typical beam end and boundary condition with 42 response points



Figure 4.47 Forced vibration response measurement of northeast end and boundary condition of beam 3



Figure 4.48 Forced vibration response measurement of northeast end and boundary condition of beam 4 with noticeable deterioration of the bottom flange

4.3.3.5 Analysis of Relative Motion of Beam End

Figures 4.49 and 4.50 show overlaid FRFs from 0-125 Hz. They were calculated from data gathered in two independent forced vibration tests on the northeast boundary condition/end of beam 4 and the northeast boundary condition/end of beam 3, respectively. The FRFs look fairly noisy because response points were distributed across various substructures of the end beam assembly (as shown in Figure 4.46). Because the response points crossed structural boundaries, these results were not used in damage detection algorithms, but instead were used to understand the relative motion between points caused by a forced excitation.

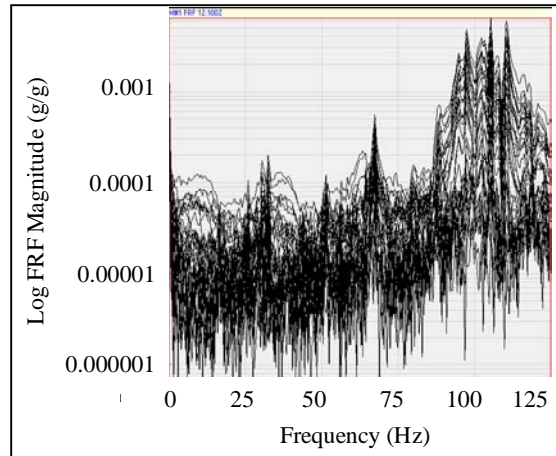


Figure 4.49 Overlaid FRFs from forced vibration test on northeast boundary condition and end of beam 4

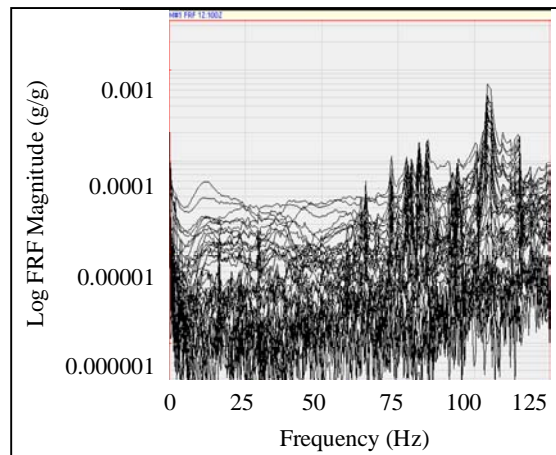


Figure 4.50 Overlaid FRF's from forced vibration test on northeast boundary condition and end of beam 3

4.3.3.6 Impact Excitation at 13.5 Hz

The relative motion of the northeast boundary conditions of beam #3 and #4 were animated at various frequencies to see if there was a significant difference between the motion of an interior and exterior beam end. Because 13.5 Hz was shown to cause problematic motion during the full structure operational vibration test, it was chosen as a possible problem frequency in this analysis as well. Screenshots of the relative response of an exterior beam end (NE4) and

interior beam end (NE3) are shown in Figures 4.51 and 4.52, respectively. Both figures show the beams vibrating at 13.5 Hz, which is the first MS of the structure. As shown in Figure 4.51, the exterior beam end including the bearing plates twist significantly due to a vertical impact whereas Figure 4.52 shows almost no off-center motion in the interior beam end.

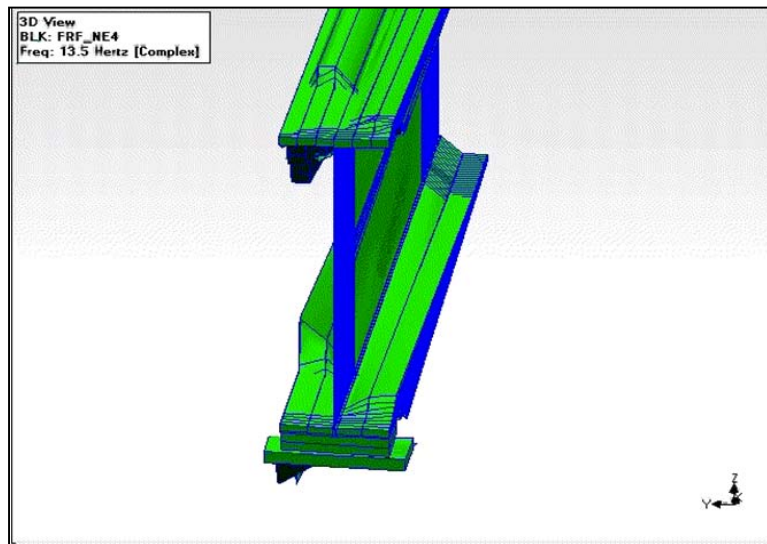


Figure 4.51 Screenshot of MEscape NE4 (exterior beam) boundary condition animation of FRF's at 13.5 Hz showing significant torsional motion

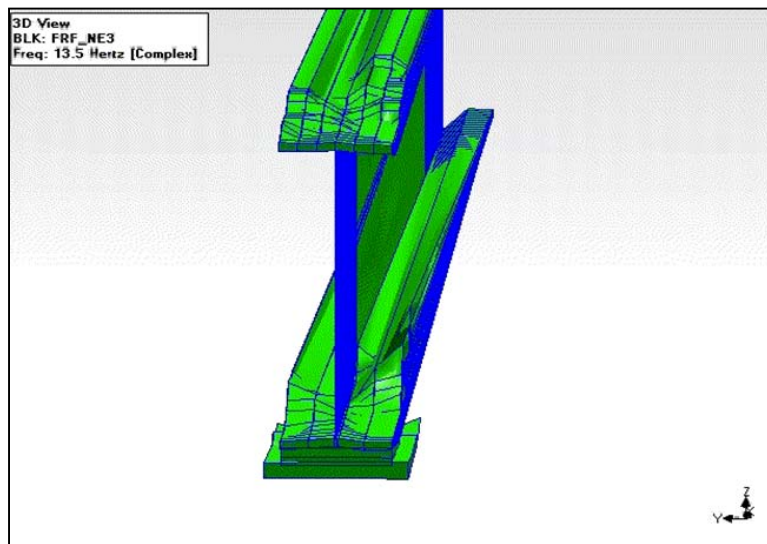


Figure 4.52 Screenshot of MEscape NE3 (interior beam) boundary condition animation of FRF's at 13.5 Hz showing very little torsional motion

4.3.3.7 Impact excitation at 16.5 Hz

Although waveform analysis showed that 13.5 Hz was the most significant frequency excited under operational traffic load, 16.5 Hz was also identified as a significant frequency. As shown in Fig. 4.53, the fine mesh of response points at the northeast boundary condition of beam #4 was animated at this frequency and showed the most significant torsional motion of any of the frequencies in the 125 Hz measurement spectrum. Therefore, this frequency can also be considered problematic in that its motion was correlated with the same cracking that the first vertical bending mode caused (as shown in Figure 4.42). When the entire structure was animated at 16.5 Hz, no discernable vertical MS was recognized, meaning that this excitation frequency causes a mixed-mode response.

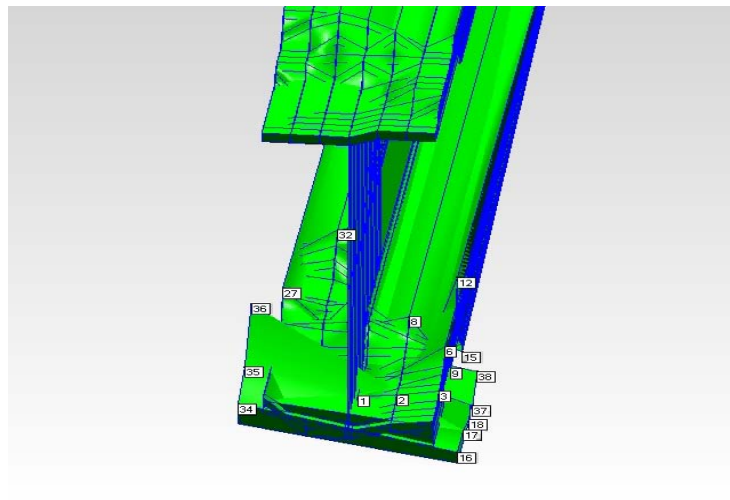


Figure 4.53 Screenshot of MEscape NE4 (exterior beam) boundary condition animation of ODSFRFs at 16.5 Hz showing the most significant torsional motion of any frequency in the 125 Hz measurement spectrum

4.3.3.8 Impact Excitation at 35 Hz

Another frequency identified as being significant during the waveform analysis was 35 Hz. As shown in Figure 4.54, the fine mesh of response points at the northeast boundary condition of beam #3 was animated at this frequency and showed very significant tension-

compression action, but still no torsional motion. If tension-compression motion were a concern beneath the interior beams, 35 Hz could also be considered a problematic frequency, even though it causes mixed-mode response.

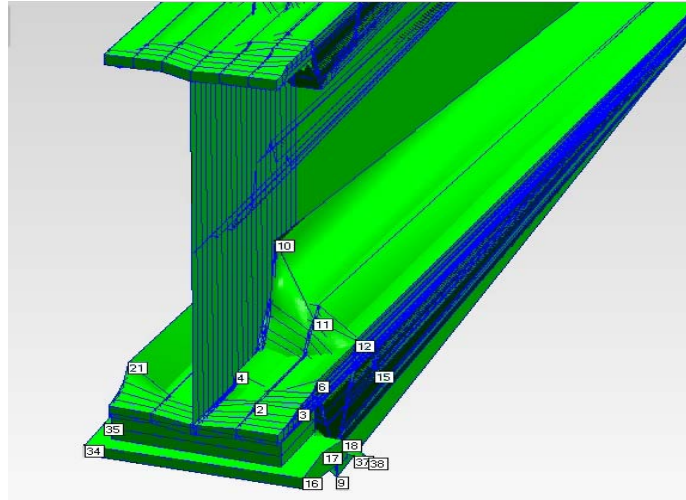


Figure 4.54 Screenshot of MEscope NE3 (interior beam) boundary condition animation of ODSFRFs at 35 Hz showing significant compression-tension motion

4.3.3.9 Comparison of Midpoint ODSFRF Magnitudes

In an attempt to understand why moderate and heavy cracking was only recognized in the abutment below one of the exterior beams, the ODSFRF magnitudes (relative to the reference accelerometer on beam #3) were analyzed at the midpoint of each beam. 13.5 Hz was chosen as the excitation frequency during the comparison because it caused each beam to experience first mode bending with maximum deflection at the midpoint. Table 1 shows the resulting ODSFRF magnitudes at midspan for each beam. The relative ODSFRF magnitude of beam #4 is approximately 51% greater than the next highest beam. Although the cause of this significantly larger midspan deflection during first vertical mode bending is unknown, possible reasons could include the following: uneven load distribution due to settlement; a loss of cross section due to

corrosion that was observed in the beam's lower flange 0.3 m (1 ft) from the northeast abutment; or uneven traffic distribution.

Table 4.1 Midpoint ODSFRF Magnitudes at 13.5 Hz

Beam 1	Beam 2	Beam 3	Beam 4
4.60E-03	5.80E-03	6.54E-03	9.89E-03

CHAPTER 5

FINITE ELEMENT MODELING

Numerical modal analysis of a healthy bridge using the finite element method can assist in identifying local areas of high stress or strain at the natural frequencies. However, with aging, new damage areas may develop, limiting the benefits of the numerical model. Nevertheless, a healthy bridge model can still give useful information about some high stress areas caused by excitation of the modes. While the healthy model of an older field bridge under investigation may not accurately reflect the dynamic properties of the bridge, the information gained from this model can be used to partially verify the findings of the proposed ORWA methodology. For example, both FEA and ORWA can be used to visualize a certain vertical bending mode of the structure. Damage areas correlated with motion caused by traffic loading on the actual bridge can be viewed on the finite element model. If the model shows an area of high strain or stress in the same areas identified as being critical during ORWA, the experimental methodology can be verified and trusted at all excitation frequencies.

5.1 Model Details

Using data from the as-built plans of FHWA #31690 provided by the Iowa Department of Transportation, a numerical model of a bridge similar to the field tested structure was created using ANSYS. The solid model was created with a mesh size of 12 in. on the majority of the structure as shown in Figure 5.1. However, the face of the abutment uses a mesh size of 4 in and the rest of the abutment uses much larger elements, automatically sized using ANSYS. This meshing resulted in approximately 62000 tetrahedral solid elements. A specified elastic modulus of 29000 ksi was used for the steel beams, diaphragm members and bearing plates. A specified elastic modulus of 3528 ksi was used for the concrete abutments and deck.

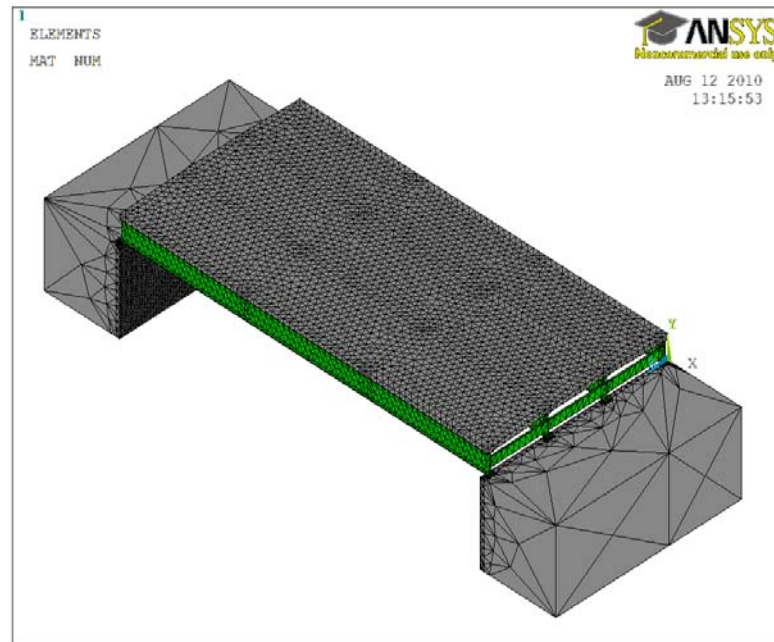


Figure 5.1 Finite element model mesh of the field bridge

Due to the age of the structure, issues such as settlement, cracking and significant corrosion make it very impractical to attain the actual dynamic properties of the tested field structure. Instead, the main focus was to view the effect of the first MS of a highway bridge similar to FHWA #31690 on the abutment and deck, in order to supplement ORWA findings. Although the beam, diaphragm, deck and bearing plate sizes and locations are all accurate the structure was simplified because users were not interested in matching the exact dynamic characteristics (i.e. natural frequencies) of the field bridge. For example, although each abutment is properly located relative to the rest of the structure, they were modeled by a 12 ft x 12 ft concrete cube in order to conserve computational time and effort. Furthermore, the concrete parapet on the deck was ignored along with all soil considerations. Instead of using springs with a specified stiffness on the bottom of each abutment, the concrete was simply fixed with applied boundary conditions. Previous work has created a more detailed and accurate FEM

of a single-span composite steel I-girder and concrete deck bridge, but the modeled field structure was less than 5 years old in this case (Whelan et al., 2009).

5.2 Model Results

A modal analysis was carried out on the solid model and strain results were overlaid on various displaced structures (dependent on applied MS). Because ORWA of the field tested bridge showed that the most dominant MS was the first vertical bending mode and problematic motion was recognized while animating this shape, the first vertical bending MS was analyzed using the FEM as shown in Figure 5.2. Areas of concern identified in ORWA were viewed in ANSYS with overlaying contour plots of lateral strain.

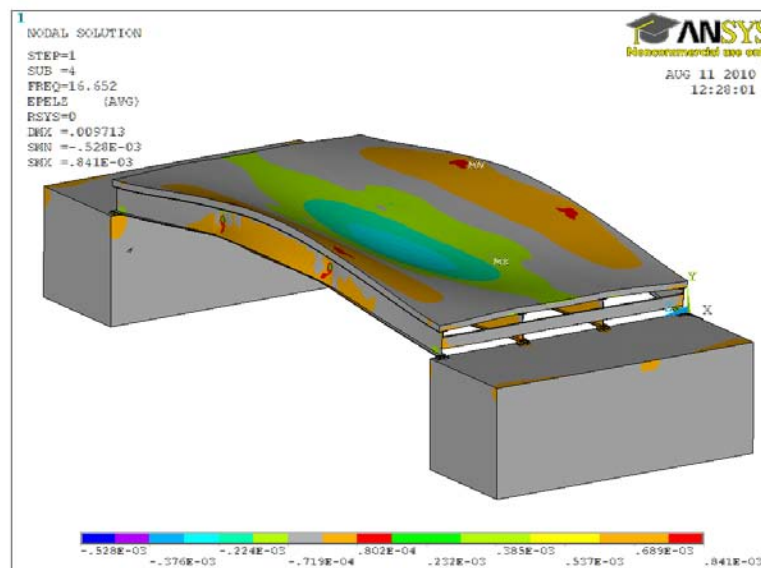


Figure 5.2 First vertical bending mode of the FEM with overlaid contour plot of lateral strain

The first area of concern was the bottom of the concrete deck where lateral cracking was recognized in the field around one of the intermediate diaphragm rows due to first vertical mode bending motion. A large area of compressive lateral strain is noticeable in the bottom of the concrete deck during first mode bending of the finite element structure as shown in Figure 5.3.

Compressive strain will cause cracking in concrete in a direction parallel to the strain, due to

Poisson's effect. Because the first MS was shown to cause damaging motion during ORWA and the FEM shows significant compressive lateral strain on the bottom of the concrete deck during first vertical mode bending, it can be inferred that this motion could be responsible for the observed lateral cracking in the bottom of the field bridge's concrete deck, as shown in Figure 4.39.

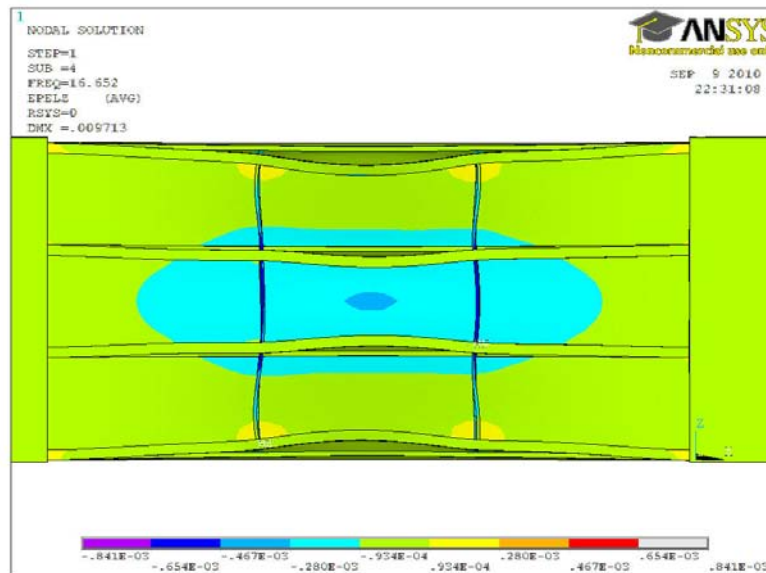


Figure 5.3 Compressive lateral strain caused by first vertical bending mode of the FEM on the bottom of the concrete deck

The second area of concern was the upper corners of the abutments where significant diagonal cracking was recognized in the field due to compression-tension and torsional action. There is increased compressive horizontal strain in the upper corners of each abutment in the finite element structure, as shown in Figure 5.4, almost exactly in the area where a large crack was found propagating from the bearing pads on the field structure. There is also increased compressive vertical strain in the finite element structure in the same area, as shown in Figure 5.5. As mentioned before, compressive strain will cause cracking in concrete in a direction parallel to the strain, due to Poisson's effect. When the same area of concrete is subjected to

horizontal and vertical compressive strain, diagonal cracking is likely to develop. Therefore, it can be inferred that first mode bending may be responsible for the observed diagonal cracking in the northeast abutment below beam #4, as shown in Figure 4.43.

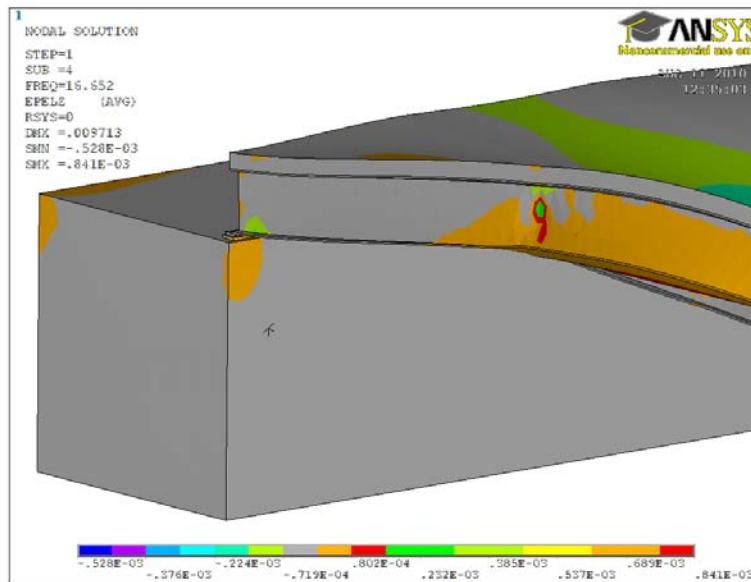


Figure 5.4 Compressive horizontal strain caused by first vertical bending mode of the FEM on the corner of an abutment

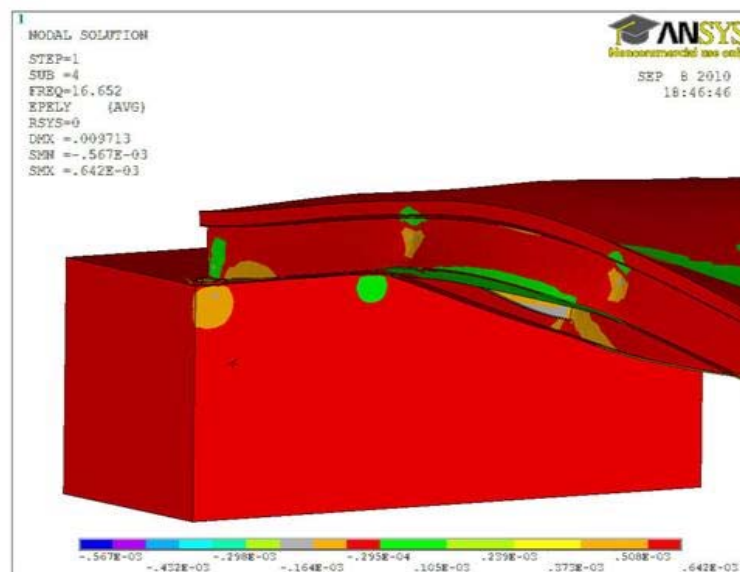


Figure 5.5 Compressive vertical strain caused by first vertical bending mode of the FEM on the corner of an abutment

CHAPTER 6

DISCUSSION AND RECOMMENDATIONS

6.1 VBDI

Vibration-based damage identification (VBDI) techniques were studied to assess their applicability to DOT highway bridges. These techniques, namely the FRF curvature method with various fitting parameters, were used in numerical simulations, laboratory experiments, and field experiments.

Numerical simulations on a plate with two damage locations of varying severity showed that the FRF curvature method is theoretically capable of locating and quantifying damage with great accuracy using either local or global curve fitting. When noise was introduced, the accuracy and precision of damage identification was dependent on damage severity. A large change in cross section (60%) was identified with 1% added random noise, but a small change in cross section (5%) was not detected. Numerical simulations are useful in that they show the significant impact of noise on various damage detection algorithms. Because all vibration-based experiments introduce noise from various sources (transducers, environment, etc.), it is important not only to limit this noise but to understand its inevitable effect on damage detection.

Laboratory experiments were first completed on an I-beam. This structure was relatively simple; its cross section was highly uniform and its boundary conditions were simplistic. To simulate damage in the laboratory, masses were fixed to the top flange of the structure. In the first experiment, a small mass (1.8% of total beam mass) and a large mass (6% of total beam mass) were accurately located with high precision using the FRF curvature method with local curve fitting. However, this method was unable to quantify the damage correctly, showing a greater change in curvature around the small mass than large mass. This is most likely due to the

location of the small mass, which was toward the middle of the beam, where there is maximum deflection. Further investigations could focus on the effect of location on damage quantification, with equivalent single-mass tests at various locations across the structure. A segmented approach could be developed to analyze portions of a structure separately from each other.

A new approach to curve fitting was considered using the same data from the two-mass test. This approach first used global curve fitting and then locally curve fit the data to create a synthetic baseline structure. Both mass locations were accurately identified and quantified (the large mass showed a much larger change in curvature than the small mass). Although this double-fitting method shows promise, it is highly dependent on the parameters chosen during global fitting, and more experiments need to be run to test its applicability to real structures. Using the same two-mass setup, a nodal mesh study was conducted to determine the effect of excitation distance on damage detection results from a roving excitation test. Three experiments were run using excitation spacing of 2 inches (2.5% of total beam length), 4 inches (5% of total beam length), and 6 inches (7.5% of total beam length). Only the test using excitation spacing of 2 inches (in addition to the standard 1 inch spacing test) was able to accurately locate the damage locations. This study provided the necessary knowledge to determine nodal spacing for the scale bridge and field experiments.

The final test run on the I-beam was a single damage location test with clamps fixed to the outer edge of the top flange. These clamps represented 3.7% of the beam's total mass. Similar to the two-mass test, the FRF curvature method with local curve fitting was able to correctly locate the presence of the clamps. This study showed that a roving excitation test on the centerline of the I-beam was independent of whether or not the damage was also located on the centerline.

Laboratory testing was also completed on a 1/6 scale model of a single span, steel girder highway bridge. A forced excitation, roving response test was run on the baseline structure to see if the diaphragm members could be located as highly stiffened regions. The FRF curvature method with local curve fitting was able to clearly locate a stiffened region in the middle two-thirds of the bridge. Therefore, the effect of the diaphragm members in this sort of a structure is more spread out than the assumed local region surrounding each diaphragm member. This same test was then run with a mass (3.2% of total structure mass) fixed to the top flange of one of the beams. The FRF curvature method with local curve fitting showed that the beam without the mass had virtually the same behavior as the baseline test. The beam with the mass had a much different damage index that no longer showed the highly stiffened region between the intermediate diaphragm members. However, the damage detection algorithm was unable to locate the mass. Further testing could increase the size of the mass until it was located using this method and also increase the density of the response mesh on the beams.

An operational vibration test was simulated on the scale bridge by impacting multiple points on the top flanges of each beam and averaging all responses. The actual motion of each response point was then animated. Various operating shapes were identified, and the bending characteristics of the diaphragm members in relation to the girders were recognized. Hypotheses were made regarding frequencies that would cause significant damage if a deck and abutment were present. Further work could focus on expanding this structure to resemble a bridge more closely, with a wood or concrete deck and some sort of external abutment. The same operational response testing could then be completed and analyzed to correlate actual motion with damage in the laboratory.

Early field experiments were completed on a single-span composite steel girder, concrete deck bridge. The first test run attempted to acquire data for all four girders during a roving response test with a single fixed excitation point on an exterior beam. Accelerometers were roved with the help of a DOT Snooper truck that was parked on the bridge during the excitation. The FRF curvature method with local curve fitting was used to create damage indices for each beam; however, only the beam with the impact yielded usable data. The damage index for this beam (beam 4) clearly showed the impact location and small areas of stiffness around each intermediate diaphragm member. The other three damage indices were too noisy to make any conclusions because the impact excitation was so heavily damped by the time it reached other members.

Later field experiments were completed on the same DOT bridge but without the Snooper truck. Instead, scaffolding was used to reach the entire superstructure. Because earlier testing showed that excitation on a single beam was not adequate for detecting damage on the entire structure, the first test that was run was an independent roving response test for each beam. This test yielded the highest quality FRFs for any test run on the field bridge. Using the FRF curvature method with local curve fitting, four separate damage indices were created. All four showed the impact point, but the stiffened regions around the diaphragm members were only located on the exterior beams. Other changes in FRF curvature were too random and spread out to signify the presence of a change in dynamic properties due to damage.

The most extensive test run on the DOT bridge was a global operational vibration test with response points on the beams, diaphragm members, and abutment wall. This test used vibration caused by traffic as an unknown excitation and a reference accelerometer as the input; likewise, roving accelerometers were the output. The ODSFRF curvature method was used to

create damage indices for the four beams and four rows of diaphragm members. The damage indices for the exterior beam very clearly showed a highly stiffened region between the intermediate diaphragm members. The damage indices for the interior beams indicated the same stiffened region between the diaphragm members but also extended out well past these locations. This larger stiffened region, covering approximately two-thirds of each interior beam, is very similar to the characteristics seen in the laboratory scale bridge. Damage indices for the diaphragm members showed no discernable changes in FRF curvature, meaning that all locations measured had very similar levels of stiffness and damping.

6.2 ORWA

The most influential use of data collected on the field bridge was through an analysis of operational motion and time waveforms during the new ORWA methodology. To understand the frequency components of the traffic load relative to the reference accelerometer during the operational vibration test, the time waveforms of all 880 automobiles used in the test were converted to the frequency domain using a FFT. By overlaying all frequency waveforms, it was found that the traffic load contributes most to a frequency of 13.5 Hz, which is to be expected (13.5 Hz is the first fundamental frequency of the bridge). However, other significant frequencies are 7.5 Hz, 15.5-16.5 Hz, 19.5-24 Hz, and 35 Hz. All 440 response points measured during the global operational vibration test were animated using an average automobile frequency response function (by overlaying 880 ODSFRFs).

The motion of the bridge as a whole was animated at 13.5 Hz and correlated with noticeable lateral cracking in the concrete deck near the intermediate diaphragm rows. Also, frequencies causing torsional and compression-tension action experienced by the abutment directly beneath the exterior beams were correlated with both significant and minor cracking in

those regions of the abutment. The frequencies that caused the most significant torsional and compression-tension action in the exterior beams were 13.5 Hz and 16.5 Hz. Although very little cracking was noticed beneath the interior beams of the field bridge, significant compression-tension action was observed when the structure was excited at 13.5 Hz and 35 Hz. These observations are important because the problematic frequencies can be compared to the common frequencies noticed from analysis of the time waveforms. Since at least some of the 880 automobiles traversing the structure excited 13.5 Hz, 16.5 Hz, and 35 Hz it can be inferred that the operational traffic of this particular bridge causes problematic, crack-causing motion in certain parts of the structure.

Even though serious cracking was only visually evident in the NE4 abutment corner, moderate diagonal cracking was observed in the SW4 abutment corner and minor cracking and spalling was observed in the corners below beam #1. The cause of the uneven cracking in the abutment corners could be due to uneven load distribution due to settlement, a loss of cross section due to corrosion that was observed in the beam's lower flange 0.3 m (1 ft) from the northeast abutment, or uneven traffic distribution. Furthermore, a visual inspection of the face of the abutment wall or deck bottom may not be adequate in detecting damage in that part of the structure. A key feature of ORWA is that it can be used independently or along with any damage detection technique (ranging from visual inspection to state-of-the art vibration-based or imaging-based methodologies) to correlate damage with structural motion and predict future damage locations due to operational vibration.

Understanding the causes of damage areas will help bridge engineers in their decision making regarding maintenance and management. When used with other damage detection techniques, ORWA can allow engineers to obtain a more holistic understanding of a bridge's

condition. ORWA will help determine optimal placement of structural health monitoring sensors used in localized damage detection studies. For example, a fine mesh of permanent strain gauges could be permanently fixed to the part of a structure where ORWA has shown that damage not only exists but has been correlated with operational vibration in a way that may cause damage growth. In this way, the long term effects of the traffic loading on the damage area could be studied without equipping the entire structure with labor-intensive transducers.

When used in combination with FEM updating, ORWA can help select the critical prone-to-damage areas on the bridge for detailed localized stress analysis. If ORWA shows that there is a specific area of interest on a structure, further impact or operational excitation tests could be run to determine the modal characteristics of that part of the structure. That substructure could then be finite element modeled and updated with experimental results so that an accurate stress analysis could be completed. Modeling and testing only the parts of the structure that are of interest would save on computational time and make modal updating more feasible.

Alternatively, ORWA may be used independently without the help of further testing or FEA to aid bridge engineers in operational vibration mitigation. The same bridge could be tested and excited by a different traffic loading (i.e. slower or lighter vehicles) to determine the effect of possible regulatory changes to various structures. Future work should extend ORWA to other bridge types and lengths and optimize experimental techniques to attain the most efficient response meshes for various parts of a highway bridge.

6.3 Finite Element Modeling

ORWA is inherently an experimental methodology, especially when applied to aging infrastructure. The deterioration present on virtually all bridges more than 20 years old is extremely difficult to model and quantify. Corrosion, cracking and delamination are three of the

most common damage issues that are very difficult to model. Aside from the computational efforts associated with creating an accurate finite element model, there are analysis constraints as well. A modal analysis is only capable of calculating modal stress/strain results at various natural frequencies. It is not capable of predicting the magnitude or effect of intermediate frequencies which have been shown to cause problematic motion in certain parts of the field bridge tested. Still without any structural updating, local areas with high strain were identified by the FEM model (Figures 18 and 19) and the results were consistent with the findings of the proposed ORWA methodology (Figure 11). This means that the FEM of a healthy structure can provide useful information by partially verifying experimental ORWA results. However, without a spectral analysis, FEM lacks the capability of investigating a structure's response at critical mixed modes and without updating, FEM cannot continue to represent a bridge as it ages. ORWA is capable of accomplishing both of these tasks and therefore, the proposed methodology can circumvent the need for FEM and can be used independently or alongside other nondestructive damage detection techniques on new and old bridges to give useful information about potential damage areas and their causes.

A spectral analysis could be completed on an FEM model of a field bridge (which would allow for a full frequency spectrum analysis) but there are issues associated with this analysis type as well due to the uncertainty in the structural dynamic properties of old structures. Traffic loading and its dynamic effect on a structure are unique to each bridge. Therefore, the vehicle waveforms used to excite a numerical model must be measured experimentally so field testing is still necessary. During field testing for ORWA, time waveforms and all other dynamic parameters needed for analysis are measured together, making it an efficient experimental process. The process can be made even more efficient with the use of low cost MEMS sensors

(Whelan et al., 2009) and other wireless transducer systems currently available. Even if the waveforms are gathered experimentally with the sole purpose for use in a numerical model, engineers would still face the modeling issues associated with aging infrastructure, which do not impact ORWA. However, future work could compare the computational time and benefits of a spectral analysis versus experimental ORWA. Future work could also take the same operational vibration field results from ORWA but complete an operational modal analysis (OMA). The experimental modal characteristics could then be used to update a finite element structure and a comparison could be made between the computational time and benefits of updating a finite element structure versus ORWA.

CHAPTER 7

CONCLUSION

Although the VBDI methods tested accurately detected damage in numerical simulations and laboratory experiments, field testing with both forced and operational excitation was not able to identify any localized information about the structure. Global characteristics such as stiffened regions due to the presence of lateral diaphragm members were located in some cases, but this does little in the way of improving the life of structure. Furthermore, if and when VBDI becomes a powerful tool in detecting damage in real civil infrastructure, it has no way of correlating this damage with a cause or providing a solution to the problem. Analysis of the operational response of the structure using the new ORWA methodology provides an effective way of recognizing global trends in bridge response, correlating motion with damage, and comparing excitation frequencies with problem frequencies. Current damage detection methods (i.e., visual inspection, tap test, etc.) can be used right now with ORWA to begin recognizing the root causes of various damage types. Also, finite element modal analysis can be used to partially verify ORWA results. In the future, advanced damage detection techniques (VBDI, imaging, etc.) can be used to supplement ORWA and provide an even broader base for correlating damage with causes. In this way, the best qualities of VBDI, ORWA and FEM can be utilized to detect, locate and quantify damage, predict service life, identify a cause, and provide a solution to bridge damage caused by traffic loading. Future work should continue to improve VBDI algorithms and vibration-based experimental techniques as well as test ORWA on various structures. Also, efficient, economical, pre-emptive solutions to harmful vibration caused by traffic loading should be investigated and developed in the laboratory and field.

REFERENCES

- Adams, R. D., & Cawley, P. (1979). Defect Location in Structures by a Vibration Technique. *Solid State Technology* .
- Adewuyi, A. P., Wu, Z., & Serker, N. K. (2009). Assessment of Vibration-based Damage Identification Methods Using Displacement and Distributed Strain Measurement. *Structural Health Monitoring* , 8, 443.
- Bounds, M., & White, G. (2006). Investigating rigidity of military vehicle body using Operating Deflection Shape (ODS) analysis. *Journal of the IEST* , 49 (2), 16-24.
- Chang, P. C., Flatau, A., & S.C., L. (2003). Review Paper: Health Monitoring of Civil Infrastructure. *Structural Health Monitoring* , 2, 257.
- DeMatteo, T. (2001). *Operational Deflection Shapes and Modal Analysis Testing to Solve Resonance Problems*. Computational Systems Inc.
- Farrar, C., & Jauregui, D. (1994). *Damage Detection Algorithms Applied to Experimental and Numerical Modal Data from the I-40 Bridge*. Technical Report, Los Alamos National Laboratory, N.M.
- Fraser, M., Elgamal, A., He, X., & Conte, J. P. (2010). Sensor Network for Structural Health Monitoring of a Highway Bridge. *Journal of Computing in Civil Engineering* , 11-24.
- Ganeriwala, S. N., Schwarz, B., & Richardson, R. H. (2009). Operating Deflection Shapes Detect Unbalance in Rotating Equipment. *Sound and Vibration* , 11-13.
- Guo, G. Q., Xiaozhai, Q., Dong, W., & Chang, P. (2005). Local Measurement for Structural Health Monitoring. *Earthquake Engineering and Engineering Vibration* , 4 (1), 165-172.
- Halling, M. W., Muhammad, I., & Womack, K. C. (2001). Dynamic Field Testing for Condition Assessment of Bridge Bents. *Journal of Structural Engineering* , 127 (2), 161-167.
- Huber, M. S., Bay, J. A., & Womack, K. C. (2000). Comparison of an Impact Source and a Monochromatic Source for Modal Testing of Bridges. *Proceedings of Society of Photo-Optical Engineers 5th Annual International Symposium on Nondestructive Evaluation and Health Monitoring of Aging Infrastructure* .
- Iowa Department of Transportation. (n.d.). *Primary Structures*. Retrieved April 2010, from Bridges in Iowa: http://www.iowadot.gov/pdf_files/Primary_Structures.pdf
- Kim, J. T., & Stubbs, N. (2003). Nondestructive Crack Detection Algorithm for Full-scale Bridges. *Journal of Structural Engineering* , 129 (10), 1358-1366.

- Li, S., & Wu, Z. (2007). A Non-baseline Algorithm for Damage Locating in Flexural Structures Using Dynamic Distributed Macro-strain Responses. *36*, 1109-1125.
- Liu, X., Lieven, N., & Escamilla-Ambriso, P. (2009). Frequency Response Function Shape-based Methods for Structural Damage Localization. *Mechanical Systems and Signal Processing* , *23*, 1243-1259.
- Maia, N., Sampaio, R., Silva, J., & Almas, E. (2003). Damage Detection in Structures: from Mode Shape to Frequency Response Function Methods. *Mechanical Ssystem Signal Processing* , *17* (3), 489-498.
- McHargue, P., & Richardson, M. (1993). Operating Deflection Shapes From Time Versus Frequency Domain Measurements. *11th IMAC Conference*. Kissimmee.
- Mertlich, T. B., Halling, M. W., & Barr, P. J. (2007). Dynamic and Static Behavior of a curved-girder Bridge with Varying Boundary Conditions. *Journal of Performance of Constructed Facilities* , *21* (3), 185-192.
- Miller, R. A., Aktan, A. E., & Shahrooz, B. M. (1992). Nondestructive Testing of Concrete Elements and Structures. *Proceedings of Nondestructive Testing of Concrete Elements and Structures* , 150-161.
- Onari, M. M., & Boyadjis, P. A. (2009). Solving Structural Vibration Problems Using Operating Deflection Shape and Finite Element Analysis. *Proceedings of the Twenty-fifth International Pump Users Symposium*, (pp. 85-102).
- Pandey, A., Biswas, M., & Samman, M. (1991). Damage Detection from Changes in Curvature Mode Shapes. *Journal of Sounds and Vibration* , *145* (2), 321-332.
- Ratcliffe, C. P. (2009). Local Damage Detection with the Global Fitting Method Using Mode Shape Data in Notched Beams. *Journal of Nondestructive Evaluation* , *28*, 63-74.
- Ratcliffe, C., Crane, R., & Gillespie, J. (2004). Damage Detection in Large Composite Structures using Broadband Vibration Method. *Journal of the British Institute of Non-destructive Testing* , *46* (1), 10-16.
- Richardson, M., & Formenti, D. (1985). Global Curve Fitting of Frequency Response Measurements using Rational Fraction Polynomial Method. *3rd IMAC Conference*. Orlando.
- Roberts, G. W., Meng, X., & Dodson, A. H. (2004, May). Integrating a Global Positioning System and Accelerometers to Monitor Deflection of Bridges. *Journal of Surveying Engineering* , 65-72.
- Rytter, A. (1993). *Vibration-based Inspection of Civil Engineering Structures*. PhD Thesis, Alborg University, Dept of Building Technology and Structural Engineering.

- Sampaio, R. M., & Silva, J. (1999). Damage Detection Using the Frequency-Response-Function Curvature Method. *Journal of Sound and Vibration* , 226 (5), 1029-1042.
- Schwarz, B., & Richardson, M. (2004). Measurements Required for Displaying Operating Deflection Shapes. *22nd IMAC Conference*. Dearborn.
- U.S. Department of Transportation Federal Highway Administration. (2010, February 5). *FHWA Bridge Programs Structure Type by Year Built*. Retrieved April 2010, from Structures: <http://www.fhwa.dot.gov/bridge/nbi/yrblt09.cfm>
- Uhl, T., Hanc, A., Tworowski, K., & Sekiewicz, L. (2007). Wireless Sensor Network Based Bridge Monitoring System. *Key Engineering Materials* , 499-504.
- Vold, H., Schwarz, B., & Richardson, M. (2000). Displaying Operating Deflection Shapes from Nonstationary Data. *Journal of Sound and Vibration* , 34 (6), 14-18.
- Whelan, M., Gangone, M., Jenoyan, K., & Jha, R. (2009). Real-time Wireless Vibration Monitoring for Operational Modal Analysis of an Integral Abutment Highway Bridge. *Engineering Structures* , 31, 2224-2235.
- Yao, L., Yao, P., & Meng, X. (2008). GPS-based Dynamic Monitoring and Analysis of Nanpu Bridge Deformation. 36 (12), 1633-1636.
- Zhao-Dont, X., & Zhisen, W. (2007). Engery Damage Detection Strategy Based on Accerleration Responses for Long-span Bridge Structures. *Engineering Structures* , 29, 609-617.